Science and Technology of Nuclear Installations

Advanced Technologies in Nuclear Waste Management Process Design and Materials

Lead Guest Editor: Dimitrios Tsaoulidis
Guest Editors: Samuel T. Murphy and Rema Abdulaziz

Advanced Technologies in Nuclear Waste Management Process Design and Materials

Science and Technology of Nuclear Installations

Advanced Technologies in Nuclear Waste Management Process Design and Materials

Lead Guest Editor: Dimitrios Tsaoulidis
Guest Editors: Samuel T. Murphy and Rema Abdulaziz

Contents

Hindawi
Science and Technology of Nuclear Installations
Volume 2020, Article ID 8094205, 7 pages
https://doi.org/10.1155/2020/8094205

Research Article

Solidification and Stabilization of Spent TBP/OK Organic Liquids in a Phosphate Acid-Based Geopolymer

Teng Dong,[1,2] Shuibo Xie ,[1,2] Jingsong Wang,[1] Guodong Zhao,[2] and Qingchun Song[1]

[1]*Pollution Control and Resource Recovery Technologies Key Laboratories of Universities in Hunan Province, University of South China, Hengyang 421001, Hunan Province, China*
[2]*School of Resources Environment and Safety Engineering, University of South China, Hengyang 421001, Hunan Province, China*

Correspondence should be addressed to Shuibo Xie; sbxusc@163.com

Received 3 April 2019; Revised 28 August 2019; Accepted 14 September 2019; Published 20 January 2020

Guest Editor: Dimitrios Tsaoulidis

A method for solidifying spent tributyl phosphate and kerosene (TBP/OK) organic liquids in a phosphate acid-based geopolymer (PAG) was investigated. The TBP/OK emulsion containing tween 80 (T80), TBP/OK organic liquids, and H_3PO_4 was prepared. The TBP/OK emulsion was mixed with metakaolin to obtain solidified TBP/OK forms (SPT). The compressive strength of the SPT was up to 59.19 MPa when the content of TBP/OK was 18%. The loss of compressive strength of SPT was less than 10% after immersion and less than 25% after freeze-thaw treatment. The final setting time was 40.0 h, and the shrinkage of SPT was nearly 3%. The leaching test indicated that the release of TBP/OK from hardened SPT was limited. Characterization of SPT suggested that solidification of TBP/OK using PAG occurred by physical encapsulation.

1. Introduction

Radioactive tributyl phosphate (TBP) is a kind of waste organic solvent containing a variety of radionuclides (such as U and Pu) produced during the plutonium uranium recovery by extraction (PUREX) process for spent fuel reprocessing. The main components of this liquid are TBP, which can be used as an extractant, and kerosene (OK), which can be used as a thinner, and these components are affected by chemical and radioactive factors. Treating and disposing of the combustible organic solvent has become an urgent problem.

Large-volume Portland cements [1] were prepared to solidify TBP/OK organic liquids, and the emulsification-solidification and adsorption-emulsification-solidification methods were compared. The TBP/OK contents in the solidified materials prepared by the two methods were 15% and 18%, and the compressive strengths of the solidified forms were 11.4 MPa and 9.3 MPa, respectively. The results of the adsorption-solidification method [2] showed that the encapsulation capacity of slag cement mixed with an activated carbon adsorbent was better than that of Portland cement. The proportion of TBP/OK liquids encapsulated by slag cement was 14%, and the mechanical properties and the soak resistance of the samples solidified by slag cement conformed to the requirements of GB14569.1-2011 [3]. Zhang et al. [4] studied the solidification of TBP/OK organic liquid by sulfur aluminate cement. Zeolite, calcium hydroxide, and MR-1 type emulsifier were mixed into the cement blends to improve the performance of the solidified waste. When the specification requirements were met, the compressive strength of the solidified samples reached 14.23 MPa, and the other material properties conformed to GB14569.1-2011. The TBP/OK organic solution was hydrolyzed and then solidified by alkali slag cementitious materials [5]. The compressive strength of the solidified forms was 18.9 MPa, and the TBP/OK content was 14.49%. The nuclide leaching rate and immersion resistance conformed to the Chinese specifications. This method requires the addition of NaOH to the TBP/OK organic solution, followed by heating. A high degree of corrosivity is required for the equipment, and it is thus not easy to apply this method on a large scale.

Recently, many countries have been developing new materials to solidify the radioactive waste. The Russian

State Atomic Energy Corporation (ROSATOM) [6] developed a new polymer material that can be used to solidify TBP and mixed (water-organic biphase) sludge. A solidification experiment was conducted on a simulated radioactive organic liquid containing alkali-activated metakaolin base polymers [7], and the amount of organic liquid solidified reached 20%.

It can be noticed that the strength of TBP/OK solidified forms by cement was not more than 20 MPa. The productions of Portland cement, slag cement, and sulfur aluminate cement are characterized by high energy consumption and serious pollution, while geopolymers are environmentally friendly and green materials [8]. Sodium silicate-metakaolin geopolymers have been applied to solidify heavy metals, nuclear waste, and oil [9, 10]. PAG is synthesized in an acidic environment and has higher strength, durability, and thermal stability than sodium silicate-metakaolin geopolymers [11]. Research on the technology and mechanism of solidification of radioactive TBP/OK organic liquids by PAG is of interest.

In this paper, phosphoric acid and metakaolin are used to prepare PAG, and T80 is employed as an emulsifier. The paste fluidity, setting time, mechanical properties, leaching rate of TBP/OK, and pore structure of SPT are studied, and the mechanism of solidification of TBP/OK is discussed.

2. Materials and Experimental Methods

The kaolin used in this work mainly consisted of SiO_2 (45.35 wt.%), Al_2O_3 (39.22 wt.%), and Fe_2O_3 (0.31 wt.%). Kaolin was treated at the selected temperature of 800°C for 4 h in a muffle furnace. The obtained specimen (metakaolin) was cooled in air to ambient temperature and then stored in a dry environment.

The preparation of the solidified SPT samples is shown in Figure 1. The molar concentration of H_3PO_4 was 11 mol/L. The proportion of TBP/OK was defined as the weight of TBP/OK relative to the weight of all reactants. SPT containing 6% TBP/OK (CST), SPT containing 12% TBP/OK (DST), and SPT containing 18% TBP/OK (EST) were prepared. The dose of the emulsifier T80 was 4 vol% relative to the TBP/OK organic liquid content. The TBP/OK organic liquid was prepared by mixing OK and TBP at a volume ratio of 7 : 3. T80 was added to the TBP/OK organic liquid, and then phosphoric acid solution was added. The liquid mixture was treated with an ultrasonic disperser to prepare the emulsion (Figure 2). The emulsion and metakaolin were added to a stirring pot and stirred for 15 minutes to obtain fresh SPT (the mixing pot and mixing blade were made of 304 stainless steel). A Vicat apparatus was used to measure the initial and final setting times. The curing temperature was 70°C, and the humidity was more than 98%; while the room temperature was 36.4°C, and the humidity was 65%. Each setting time test was repeated 4 times, and the arithmetic mean was selected. Fresh SPT was poured into polypropylene (PP) plastic molds, and the samples were vibrated on a vibrating table for 3 minutes and then cured at 70°C and greater than 98% humidity for 7 days. The samples were removed from the molds after 7 days and were then cured at 40°C in an oven for 28 days. Shrinkage of the 25 mm × 25 mm × 250 mm hardened PAG and SPT was measured with a shrinkage-compensating concrete expansion rate tester, and Ø50 mm × 50 mm samples were used to measure the strength (Figure 3).

After 28 days, the CST, DST, and EST samples were dipped in deionized water at 25 ± 1°C for 42 days (Figure 4), and the strength was tested again. Hardened PAG, CST, DST, and EST samples sealed in packets were put in a freezer at a temperature of −20°C for 3 h. The samples were removed from the freezer and immediately thawed in a water tank at 18°C. The thawing time was 4 h. The samples were subjected to five freeze-thaw cycles, and then their appearance was observed, and their compressive strength was tested. The amount of leached TBP/OK in the soaking solution was measured by gas chromatography.

Fragments of the PAG, CST, DST, and EST samples were collected and dipped in ethyl alcohol. The fragments were dried in an oven at 105°C for 12 h before testing. The porosity was tested by Mercury intrusion porosimetry (MIP) experiments. An MIP instrument (Autopore IV 9500, Micromeritics) was used to measure the pore size distributions. Other dried fragments of samples were milled into powders and used for XRD measurements, FTIR, and MAS NMR experiments. XRD was conducted by using a Bruker D8 ADVANCE instrument under the following conditions: 40 kV, 40 mA, and CuKα radiation. The range of the 2θ scanning angle was between 5° and 80°. FTIR experiments were performed by using a VECTOR33 FTIR spectrometer. The samples were mixed with KBr, and the wavelength was varied from 400 cm^{-1} to 4000 cm^{-1}.

3. Results and Discussion

3.1. Workability of Fresh SPT. Fresh PAG has a fluidity of 9.8 cm, as shown in Figure 5. The fluidity of fresh CST, DST, and EST is proportional to the TBP/OK content, and the fluidity increased from 13.0 cm to 15.5 cm (Figure 5). Metakaolin has a layered structure, and water and H_3PO_4 fulfill the voids, reducing the lubricity of the slurry. Furthermore, H_3PO_4 has a certain viscosity that decreases the fluidity of fresh PAG. T80 was added as a surfactant, which reducing the interfacial tension between the TBP/OK and the aqueous phase. When TBP/OK was added to the phosphoric acid solution, TBP/OK droplets were formed after ultrasonic dispersion.

Figure 6 shows the distribution of droplets in the CST, SDT, and EST samples. When the solidified samples were broken, the droplets were removed, and spherical holes were left. More holes appeared in the solidified samples as the TBP/OK content increased. After emulsion, the organic droplets were surrounded by an outer hydrophilic layer to form spherical droplets. Spherical droplets distributed in phosphoric acid solution play a dominant role in lubrication. Therefore, the fluidity of the solidified forms increased with increasing encapsulation capacity. When metakaolin and the emulsion were mixed, the greater number of droplets reduced the surface tension of the liquid and resulted in better fluidity. This increase in droplets also caused more air to be

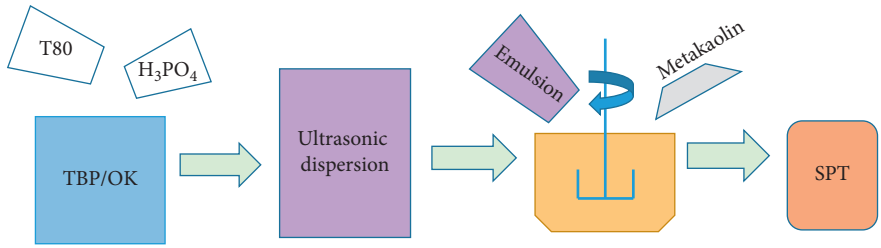

Figure 1: Preparation of the solidified SPT.

Figure 2: TBP/OK and H_3PO_4 emulsion.

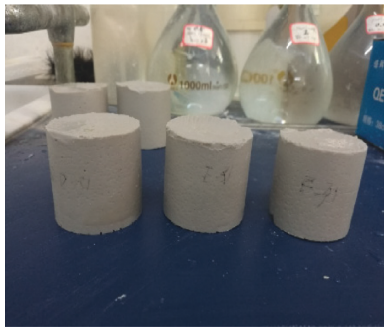

Figure 3: Hardened solidified SPT samples.

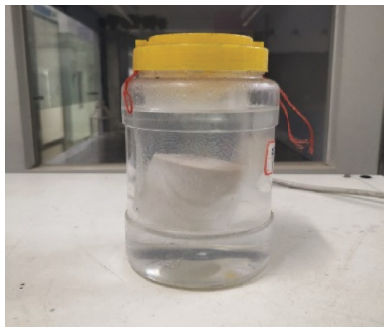

Figure 4: Leaching test of TBP/OK.

present in the solidified paste, and the porosity increased with the increase in the TBP/OK content.

When TBP/OK emulsions were mixed with metakaolin, the contact between the metakaolin powder particles and phosphoric acid decreased. Water molecules in the outer layer of droplets vaporized slowly, and dihydroxylation of the geopolymer slowed. These processes extended the setting

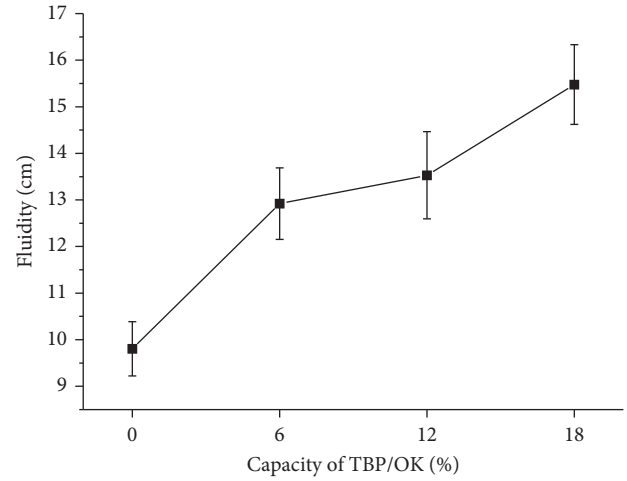

Figure 5: Fluidity of the solidified SPT samples with different TBP/OK contents.

time of the CST, DST, and EST samples. As shown in Figure 7, the initial setting time increased from 29.4 h to 30.6 h, and the final setting time increased from 35.7 h to 40.0 h. These long setting times limit the application of PAG in solidification.

3.2. Mechanical Properties of Hardened SPT. There was an obvious linear shrinkage of the PAG samples (3.2%), and the shrinkage of CST, DST, and EST was nearly 2.9% (Figure 8). As expected, the compressive strength decreased when the TBP/OK content increased. PAG has a high compressive strength of 79.07 MPa, and the strength of SPT is up to 59.19 MPa. The compressive strength did not decrease drastically with increasing TBP/OK content (Figure 9). When the composite contained 18% TBP/OK, the decrease in the compressive strength was 25%. These results indicate that the PAG is a rigid material with good mechanical properties. After the immersion test and freeze-thaw test, there were no obvious cracks on the surfaces of the PAG, CST, DST, and EST samples. The loss of compressive strength after immersion was less than 10%, and the loss of compressive strength after freeze-thaw treatment was less than 25% (Figure 10). These results indicated that the mechanical properties of SPT meet the requirements of the Chinese regulations "Performance Requirements for Low and Medium-Level Radioactive Waste Solidified Forms—Cement Solidified Forms."

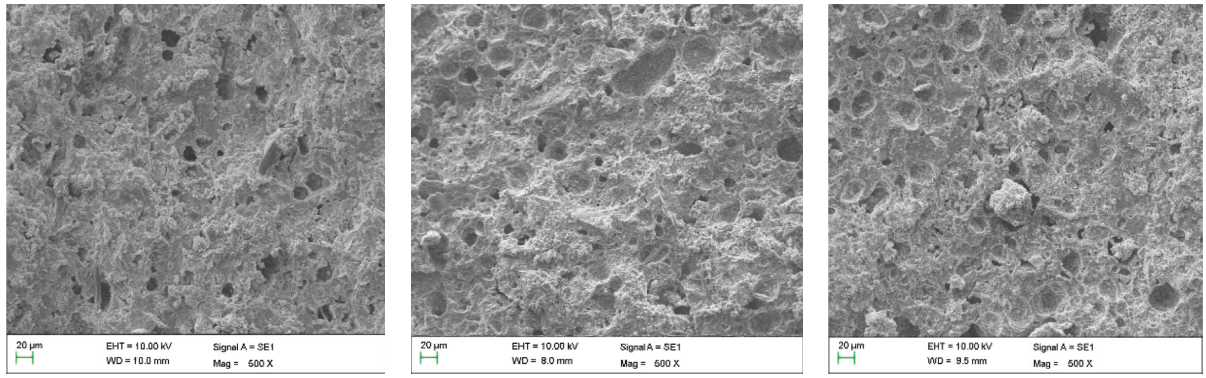

(a) (b) (c)

Figure 6: Distribution of droplets in the CST (a), SDT (b) and EST (c) samples.

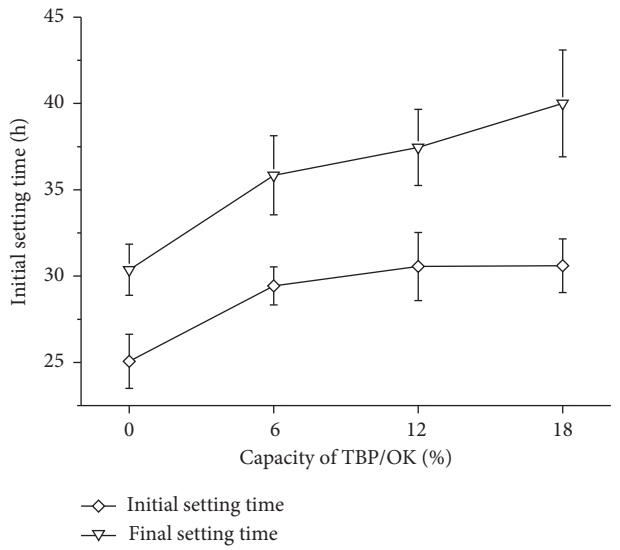

Figure 7: Setting time of the solidified SPT samples with different TBP/OK contents.

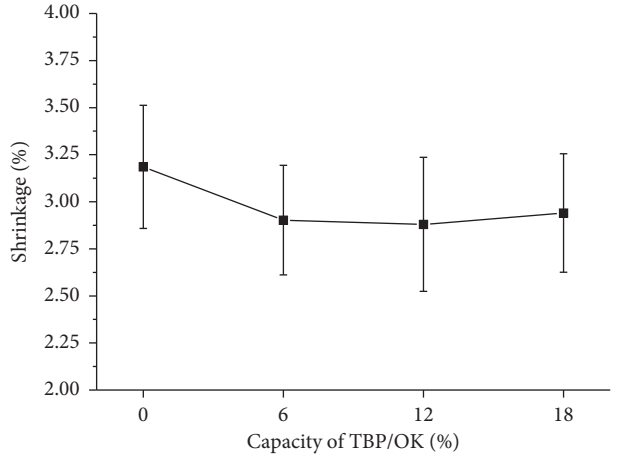

Figure 8: Shrinkage of the solidified SPT samples with different TBP/OK contents.

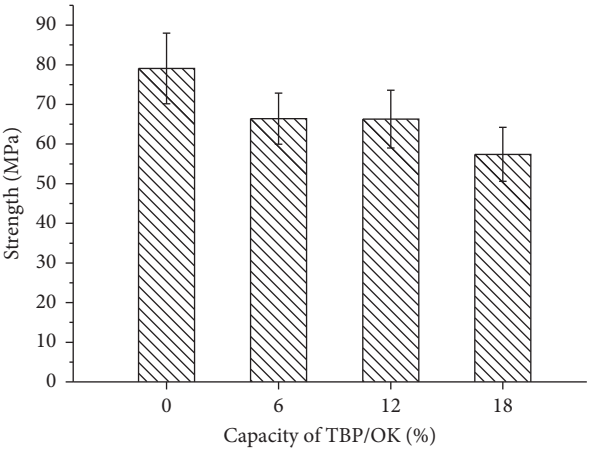

Figure 9: Compressive strength of the solidified SPT samples with different TBP/OK contents.

3.3. Compositions of Hardened SPT. A comparison between the X-ray diffraction patterns of the studied kaolin (KA) and calcined kaolin (MK) shows that all diffraction peaks corresponding to kaolin disappeared after heat treatment. Diffraction peaks corresponding to quartz were observed in the calcined kaolin diffraction patterns, while peaks corresponding to quartz and $AlPO_4$ crystal were observed in the PAG and SPT diffraction patterns (Figures 11 and 12). $AlPO_4$ was formed from the Al^{3+} in metakaolin and PO_4^{3-} from the H_3PO_4 solution. This indicates that the quartz remained unaffected during the geopolymerization process. The X-ray diffraction patterns of PAG and SPT exhibit an amorphous characteristic in the 2θ range of 15–20°. This indicates that the structures of PAG and SPT are typically glass-like.

In agreement with the X-ray diffraction results, FTIR spectra show the disappearance of metakaolin bands and the appearance of new bands that are related to new species (Figures 13 and 14). For calcined kaolin, the bands at 907 cm^{-1} ascribed to Al(VI)-OH disappeared as -OH desorbed during the heating process. Bands at 805 cm^{-1}, 688 cm^{-1}, and 568 cm^{-1} ascribed to -Si-O-Al(IV), -Si-O-

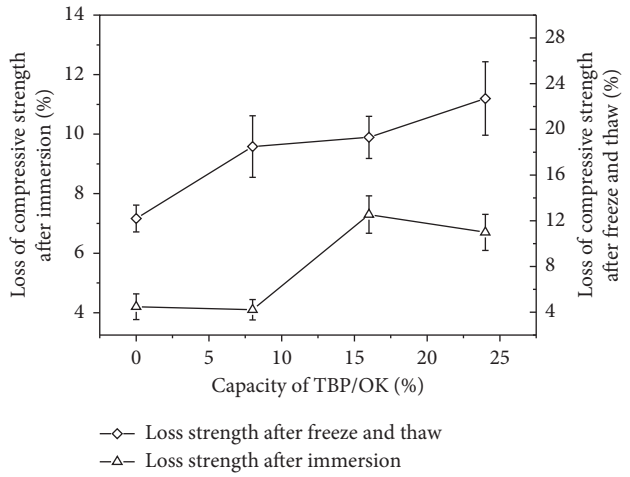

Figure 10: Loss of compressive strength of the solidified SPT samples with different TBP/OK contents.

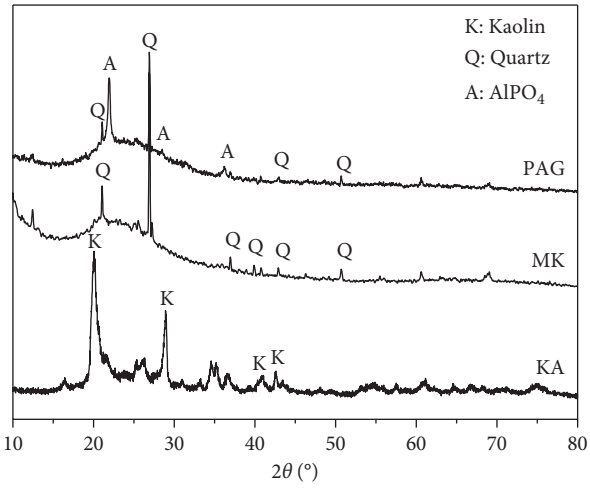

Figure 11: X-ray diffraction patterns of kaolin (KA) [12], calcined kaolin (MK) [12], and phosphate acid-based geopolymer (PAG).

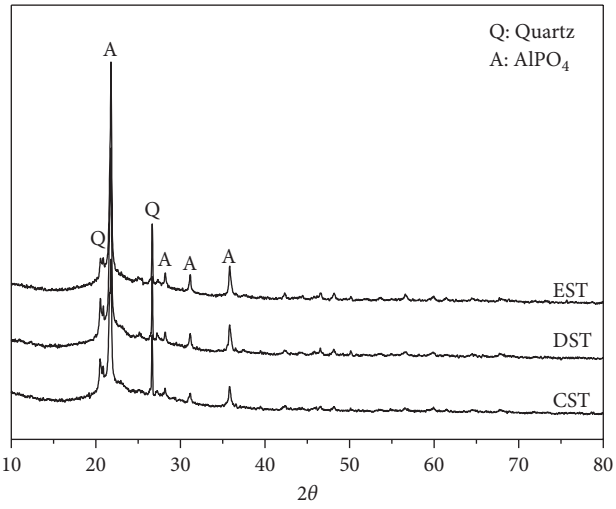

Figure 12: X-ray diffraction patterns of the PAG-solidified CST, DST, and EST samples.

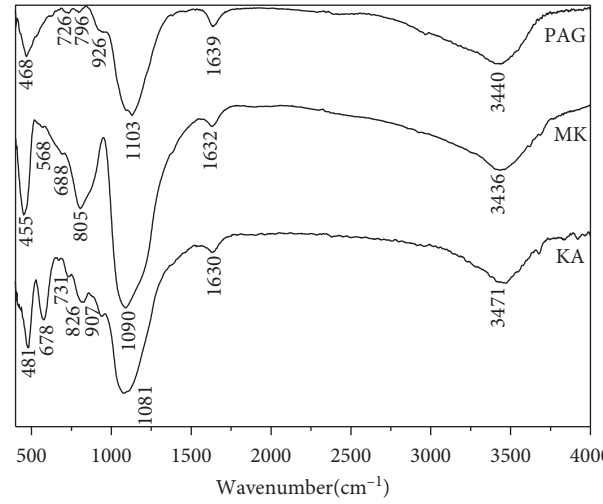

Figure 13: FTIR spectra of kaolin (KA) [12], calcined kaolin (MK) [12], and phosphate acid-based geopolymer (PAG).

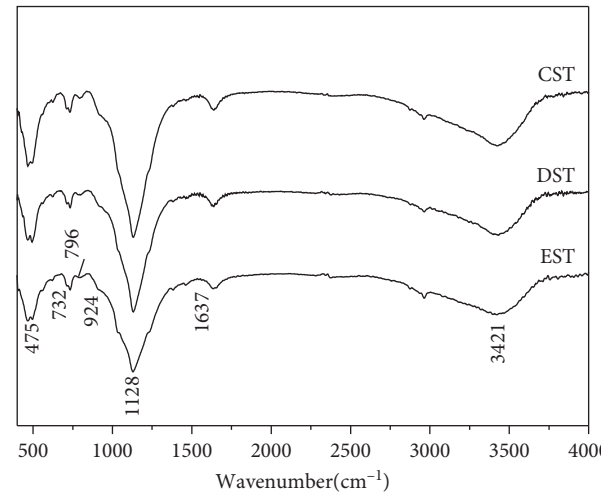

Figure 14: FTIR spectra of the PAG-solidified CST, DST, and EST samples.

Al(V), and -Si-O-Al(VI), respectively, appeared in the spectra of calcined kaolin. These bands disappeared after geopolymerization, and new bands at 726 cm^{-1}, indicative of the formation of -P-O-Al-, were observed in the spectra of PAG [12]. The bands at 926 cm^{-1} are attributed to -P-O-P- vibrations [12, 13].

The Si-O symmetrical vibration of metakaolin at 1090 cm^{-1} shifted by approximately 13 cm^{-1} to 1103 cm^{-1} after geopolymerization. In the spectra of PAG, new bands at 796 cm^{-1} could be attributed to -Si-O-P- [14]. The bands at 455 cm^{-1} in the metakaolin spectrum, which could be ascribed to -Si-O-Si-, shifted to a higher wavenumber of 468 cm^{-1} in the hardened PAG spectrum. This shift indicates that Si-O was converted to -Si-O-P- [9]. This may be attributed to the partial replacement of the [SiO] tetrahedra by [PO] tetrahedra, thus resulting in a change in the local chemical environment. This implies that the formation of -Si-O-P-O-Si- occurred in the geopolymer network [15].

Table 1: Leaching rates of TBP/OK in PAG-solidified TBP/OK samples (SPT).

Samples	α (%)	Leaching of TBP/OK at 25°C 10^{-3}/(cm·d^{-1})									$P_{42}10^{-2}$ (cm)
		1 d	3 d	7 d	10 d	14 d	21 d	28 d	35 d	42 d	
CST	6	11.37	1.85	0.79	0.98	0.89	0.36	0.36	0.34	0.30	3.42
DST	12	12.16	2.11	1.04	1.29	0.97	0.49	0.44	0.42	0.41	4.13
EST	18	13.74	2.41	1.00	1.34	1.01	0.46	0.45	0.44	0.44	4.32

α: capacity of TBP/OK; P_{42}: cumulative leaching rate for 42 days (cm).

Table 2: Porosity and pore size distribution of PAG-solidified TBP/OK samples (SPT).

Samples	Pore size distribution				Porosity (%)
	≤10 nm	10–100 nm	100–1000 nm	≥1000 nm	
PAG	40.72	46.11	4.18	8.99	16.94
CST	35.52	47.66	7.58	9.24	17.44
DST	30.24	50.15	7.77	11.84	22.03
EST	26.82	52.36	8.59	12.23	23.47

In Figure 14, in the spectra of the CST, DST, and EST samples, the bands at 924 cm^{-1} were attributed to -P-O-P- vibrations [12, 13]. New bands at 732 cm^{-1} are in agreement with the formation of -P-O-Al-. The metakaolin bands at 455 cm^{-1} ascribed to -Si-O-Si- shift to a higher wavenumber of 475 cm^{-1} in the spectra of the hardened samples. Furthermore, new bands at 796 cm^{-1} related to -Si-O-P- were observed. The Si-O symmetrical vibration of metakaolin at 1090 cm^{-1} shifted to 1128 cm^{-1} after solidification. This indicates that the network structure of SPT comprises -Si-O-P-O-Si- and -P-O-Al- as well [12]. The products were nearly the same for PAG and SPT. Solidification of TBP/OK could occur by physical encapsulation.

3.4. Leaching Test of TBP/OK. The cumulative amounts of TBP/OK released into the leachates from SPT composite samples containing 6–18% TBP/OK at 25 ± 1°C are reported in Table 1. The cumulative quantity of TBP/OK released in the leachate increased slowly during the first two weeks of the experiment and then tended to remain stable for the remaining 42 days. The cumulative leaching rates of the CST, DST, and EST samples for 42 days were 3.42×10^{-2} cm, 4.13×10^{-2} cm, and 4.32×10^{-2} cm, respectively.

The pore size distribution of PAG and SPT is shown in Table 2. Most pore size diameters were smaller than 100 nm in PAG, CST, DST, and EST. The number of pores smaller than 10 nm decreased, while the number of pores between 10 nm and 100 nm increased. The number of pores larger than 1000 nm also increased in the CST, DST, and EST samples. The presence of emulsified droplets increased the setting time and prevented water molecules from evaporating, causing an increase in the pore size of SPT. The porosity increased with increasing TBP/OK content. The results demonstrate that TBP/OK was efficiently encapsulated in SPT and met the nuclear authorities' acceptance criteria for waste storage applications.

3.5. Discussion of Experimental Errors. To ensure the reliability of the data, including the measured compressive strength, fluidity, shrinkage, and loss of compressive strength of the solidified samples, 6 samples of each group were prepared for testing. The arithmetic mean of the values in one group of each experiment was selected as the result. If a test value in one group was larger or less than 15% of the arithmetic mean, all values in this group were discarded. The standard deviations of compressive strength were 8.91%, 6.44%, 7.28%, and 6.82%, and those of shrinkage were 0.35%, 0.29%, 0.36%, and 0.31%. The standard deviations of fluidity ranged from 0.58% to 0.94%. The standard deviations of loss of compressive strength after immersion and after freeze-thaw treatment ranged from 0.34% to 0.61% and from 1.17% to 3.02%, respectively. For setting time test, each test was repeated 4 times, and the arithmetic mean was selected. Six samples from each group were used to measure the leaching of TBP/OK and the porosity. The arithmetic mean of each experiment was selected as the result. The leaching of TBP/OK in Table 1 and porosities in Table 2 were the arithmetic means.

4. Conclusion

A method of solidifying spent TBP/OK organic liquids with phosphate acid-based geopolymer was investigated. The main findings of this study can be summarized as follows.

TBP/OK organic liquids can be solidified in PAG, and the stability of the TBP/OK emulsion in the phosphate acid solution and in the geopolymer paste during mixing allows the encapsulation of high TBP/OK contents in the composite (up to 18%).

The compressive strength of the SPT was up to 59.19 MPa when the content of TBP/OK was 18%. The loss of compressive strength of SPT was less than 10% after immersion and less than 25% after freeze-thaw treatment.

The fluidity of fresh SPT is 15.5 mm, the final setting time was 40.0 h, and the shrinkage of SPT was nearly 3% when the content of TBP/OK is 18%.

Leaching tests demonstrated that a very limited amount of TBP/OK was released from the PAG-solidified TBP/OK samples. Solidification of TBP/OK could occur by physical encapsulation.

Data Availability

The data used to support the findings of this study are available from the corresponding author upon request.

Conflicts of Interest

The authors declare that they have no conflicts of interest.

Acknowledgments

The authors gratefully acknowledge the support by the Research Foundation of Education Bureau of Huanan Province, China (Grant no. 18K075) and the National Students' Platform for Innovation and Entrepreneurship Training Program, China (Grant no. 201810555001).

References

[1] D. H. Du, L. Gong, and L. Cheng, "Study on the formulation of mass-pouring cement used to solidified organic waste liquid," *Radiation Protection*, vol. 12, no. 5, pp. 364–372, 1992.

[2] Z. Y. Chen, W. L. Huang, G. Q. Zhang, Y. J. Zhang, and J. S. Zhang, "Study on the formulation of cement solidification of 30% TBP/OK organic liquid waste," *Atomic Energy Science and Technology*, vol. 25, no. 4, p. 74, 1991.

[3] CSBTS, *Characteristic Requirements for Solidified Waste of Low and Intermediate Level Radioactive Waste-Cement Solidified Waste (GB14569.1-2011)*, CSBTS, Beijing, China, 2011.

[4] W. Zhang, J. Li, and J. Wang, "Solidification of spent radioactive organic solvent by sulfoaluminate and Portland cements," *Journal of Nuclear Science and Technology*, vol. 52, no. 11, pp. 1362–1368, 2015.

[5] R. Hua, Z. B. Zhang, S. J. Liu, and M. B. Lou, "Solidification of spent tributyl phosphate by alkali-activated slag," *Atomic Energy Science and Technology*, vol. 47, no. 11, pp. 1956–1960, 2013.

[6] Y. Pokhitonov, V. Babain, and V. Kamachev, "Russian: result and prospects of liquid solidification experiments at ROSATOM sites," in *Proceedings of the ASME 2011 14th International Conference on Environmental Remediation and Radioactive Waste Management ICEM2011*, Reims, France, September 2011.

[7] V. Cantarel, F. Nouaille, A. Rooses, D. Lambertin, A. Poulesquen, and F. Frizon, "Solidification/stabilisation of liquid oil waste in metakaolin-based geopolymer," *Journal of Nuclear Materials*, vol. 464, pp. 16–19, 2015.

[8] S. Z. Zhang and K. C. Gong, "Geopolymer," *Materials Science and Engineering*, vol. 21, no. 3, pp. 430–436, 2003.

[9] K. L. Li, "Solidification analysis of heavy metal and radioactive metal by alkali-activated cement," *Journal of Building Materials*, vol. 16, no. 2, pp. 310–314, 2013.

[10] J. Davidovits, *Geopolymer Chemistry and Applications*, National Defense Industry Press, Beijing, China, 2011.

[11] D. S. Perera, J. V. Hanna, J. Davis et al., "Relative strengths of phosphoric acid-reacted and alkali-reacted metakaolin materials," *Journal of Materials Science*, vol. 43, no. 19, pp. 6562–6566, 2008.

[12] T. Dong, S. B. Xie, J. S. Wang, Z. F. Chen, and Q. Liu, "Properties and characterization of a metakaolin phosphate acid-based geopolymer synthesized in a humid environment," *Journal of the Australian Ceramic Society*, 2019.

[13] N. R. Yang and R. H. Yue, *The Handbook of Inorganic Matalloid Materials Atlas*, Wuhan University of Technology Press, Wuhan, China, 2000.

[14] L. Stoch and M. Ś.oc, "Infrared spectroscopy in the investigation of oxide glasses structure," *Journal of Molecular Structure*, vol. 511-512, pp. 77–84, 1999.

[15] H. K. Tchakouté and C. H. Rüscher, "Mechanical and microstructural properties of metakaolin-based geopolymer cements from sodium waterglass and phosphoric acid solution as hardeners: a comparative study," *Applied Clay Science*, vol. 140, pp. 81–87, 2017.

Hindawi
Science and Technology of Nuclear Installations
Volume 2019, Article ID 3591925, 14 pages
https://doi.org/10.1155/2019/3591925

Research Article

A Fracture Criterion for Prediction of Fracture Initiation of Metal Materials at Various Stress States for Nuclear Waste Storage

Zhihui Li,[1,2,3] **Xue Yang**,[4] **and Anmin Tang**[4]

[1]*School of Aeronautics, Northwestern Polytechnical University, 710072 Xi'an, Shaanxi, China*
[2]*School of Mechanical Engineering, Baoji University of Arts and Sciences, 721016 Baoji, Shaanxi, China*
[3]*Shaanxi Province Key Laboratory of Advanced Manufacturing and Evaluation of Robot Key Components Co-founded by Baoji and the Shaanxi Department of Science and Technology, 721016 Baoji, Shaanxi, China*
[4]*School of Civil Engineering and Architecture, Xi'an University of Technology, 710048 Xi'an, Shaanxi, China*

Correspondence should be addressed to Zhihui Li; lizhihui@xaut.edu.cn

Received 25 April 2019; Accepted 2 November 2019; Published 28 November 2019

Guest Editor: Rema Abdulaziz

A fracture criterion is newly proposed to evaluate fracture behavior and predict fracture initiation of metal materials in different complicated stress states for four different fracture mechanisms including quasicleavage fracture, normal fracture with void, shear fracture with void, and shear fracture without void. The dominant factors of these four different mechanisms are distinct, so it is impossible to capture all features of fracture initiation under different stress states with a single criterion, and different functions are necessary to predict fracture initiation of different mechanisms. In the new fracture criterion, different branches of the fracture criterion have been proposed corresponding to different fracture mechanisms. Quasicleavage fracture and normal fracture with void are described as a function of the principal stress, shear fracture with void is a function of the stress triaxiality and maximal shear stress, and shear fracture without void is only controlled by the maximal shear stress. The new fracture criterion is applied to predict the fracture initiation site and the fracture direction of nodular cast iron QT400-15 in combined tension-torsion tests. Predicted results are compared with experimental results to validate the performance of the new criterion in the intermediate stress triaxiality between 0 and 1/3. The new criterion is also applied to predict the crack initiation site and the direction of crack initiation of LY12 aluminium alloy and HY130 mild steel in mixed mode fracture tests to validate the performance of the new criterion in the high stress triaxiality. The new fracture criterion gives consistent results for these materials in a wide stress triaxiality range. It is shown that the new fracture criterion is a better supplement to the deficiency of fracture mechanics and also a better amendment to traditional strength theory in complicated stress states. Therefore, the new fracture criterion is recommended to be utilized to evaluate the fracture initiation of metal structures in nuclear waste storage and other engineering applications.

1. Introduction

Metal containers of nuclear waste have been widely used around the world because of their easy removal, radiation protection, and durability. The disintegration and heat releasing of nuclear waste can cause the deterioration of material performance and deformation of the stored vessel, thus leading to fracture initiation of the metal stored vessel and waste material leaking. It is of major importance to be able to evaluate and predict the fracture behavior for design and analysis and testing purposes of nuclear waste containers, so appropriate fracture initiation criteria need to be determined to avoid fracture initiation, especially to avoid brittle fracture initiation. Despite extensive research efforts and experimental testing programs undertaken by the nuclear industry, the issue of fracture initiation has not been solved perfectly as the results obtained from such model and specimen tests cannot predict the fracture behavior of metals accurately [1–3]. Therefore, the main issue in nuclear waste storage and other engineering applications is still to provide

realistic information on the fracture mechanism and fracture criterion of such materials and to assess the safety factor against fracture initiation. Great efforts have been made in the attempt to develop reasonable models for predicting the occurrence of fracture in metal materials and structures under various loading conditions [4–6].

The most widely known model for a ductile material was put forth by Gurson in order to analyze the ductile fracture phenomena [7]. In Gurson model, an extrainternal variable, i.e., the void volume fraction, was introduced so as to capture the growth of cavities and its concomitant influence on material behavior. Tvergaard and Needleman modified the Gurson model by introducing two adjustment factors to account for the synergistic effects of void interactions and material hardening [8–10]. This approach has shown great success in predicting mode I crack growth and many other fracture phenomena caused by void nucleation, growth, and coalescence. The GTN model, although extensively used to study ductile failure and crack propagation, is also known to suffer from some limitations. For instance, the identification of a large number of material constants is required for the material under investigation. Consequently, it is difficult to evaluate possible mutual influence of the parameters. Also, the material constants are not physically based and cannot be directly measured for a material. An iterative calibration procedure, involving finite element simulations and experimental data, is necessary. Thirdly, the conjoint influence of stress triaxiality and initial void volume fraction on void growth and coalescence is not examined. The transferability of parameters to multiaxial stresses is not always proven, and possible stress triaxiality influence on damage parameters is often neglected. Especially, the void volume fraction which was used as the damage variable is a mesoscopic parameter with many influential factors and difficult to describe accurately. Therefore, the ductile fracture caused by void growth and coalescence can be modeled by the GTN relation, but the fracture caused by other mesoscopic mechanisms, for instance, the cleavage brittle fracture and the ductile fracture caused by the extension of local shear band, cannot be modeled.

Recently, there have been active studies on fracture mechanisms in different stress states, and emphasis have been laid on the relation between fracture criterion and different fracture mechanisms [11–18]. For instance, Tang and Wang [19] showed that the criterion based on only brittle and ductile fracture is not sufficient for the prediction of all fracture modes. It has also been shown that the triaxiality is an important factor for fracture. Bao and Wierzbicki [20, 21] evaluated seven fracture models based on the experimental results of Al 2024-T351 and proposed fracture strain criteria based on three different branches with shear mode for negative stress triaxialities, void-growth-dominated mode for large positive triaxialities, and mixed mode for lower positive stress triaxialities. Li et al. [22] applied the modified Mohr–Coulomb criterion to predict shear-induced fracture in sheet metal forming. In addition, many research works have focused on verification of the applicability of ductile fracture criteria to predict the fracture of metals.

Despite current research achievements on fracture criteria, there are still many unsolved issues to be explored. In nuclear waste storage and other engineering practice, metal structures are subjected to multiaxial stress states caused by their external loading conditions or changes of geometry during deformation. For a certain material, when the stress state varies, the fracture mechanisms are different [6, 23–25]. Similarly, under the same stress state, the fracture mechanisms may also change with varying material properties. For different fracture mechanisms, the corresponding parameters which dominate the fracture may vary, so it is impossible to capture all the features of fracture initiation under different stress states with a single criterion. In order to accurately evaluate and predict the fracture behavior, various controlling parameters and functions are necessary to predict fracture initiation of different mechanisms in the new fracture criterion. Moreover, ductile fracture criteria developed recently are mostly based on the assumption that the equivalent plastic strain at fracture depends on the stress triaxiality and regarded the equivalent plastic strain as fracture controlling parameters. The effects of the equivalent plastic strain on the fracture process, however, remain unclear. Previous research has found that the fracture mechanism of material depends on the amount of plastic deformation in the fracture process, but the plastic deformation is not a leading factor which dominates the occurrence of fracture, and "the fracture occurs when the plastic deformation is large" may be only a superficial phenomenon. Therefore, it is necessary to determine the controlling parameters and propose the fracture criteria for different fracture mechanisms.

In this paper, a fracture criterion will be proposed that is hopeful to overcome most of the limitations previously discussed. Based on the four different fracture mechanisms of metal materials [23], the effects of several parameters including stress triaxiality, principal stress, and maximum shear stress on the onset of fracture in metal materials are discussed. Different parameters are introduced to predict the fracture initiation of various fracture modes separately. By combining the calculating results of stress field with experimental data, a fracture criterion based on different fracture mechanisms is established. Different branches of this function are taken into account corresponding to different fracture mechanisms. In addition, identification of material parameters is discussed in detail. A series of tests including combined tension-torsion tests and I-II mixed mode fracture tests covering a wide range of stress triaxialities are used to verify this fracture criterion and calibrate material parameters and good correlation of tests and predicted results is achieved, which will provide a reasonable fracture initiation criterion for evaluating and predicting the fracture behavior in the design and analysis of nuclear waste containers.

In the following sections, we will present the experimental investigations to evaluate the effects of different stress states on the fracture mechanisms of commonly used metal materials and demonstrate the effects of the stress state on the fracture-controlling parameters and fracture criterion corresponding to different fracture mechanisms. The stress

triaxiality R_σ is used here to indicate and distinguish different stress states, and the relationship between stress state and its corresponding stress triaxiality is discussed in the authors' previous study [23].

2. Fracture Mechanisms in Different Stress States

Based on our previous studies [23], four fracture mechanisms for commonly used metal materials were discovered and defined, which were quasicleavage brittle fracture, normal fracture with void, shear fracture with void, and plastic shear fracture without void, respectively. The SEM (scanning electron microscope) images of the typical fracture surfaces of these four fracture mechanisms are shown in Figures 1(a)–1(d). From Figure 1(a), the fracture surface seems ragged as a whole; the microcracks grow mainly along grain boundaries, while there are no voids on this fracture surface. In the microscopic view, there is no law of fracture direction on a minor scale, while there is a possibility that the direction of fracture surface is only related to the local microstructures of materials and the directions of crystal interfaces. However, in the macroscopic view, the direction of fracture surface is approximately consistent with the plane of the maximal tension stress. Figure 1(b) shows that most microcracks have developed into voids, and the growth and coalescence of voids lead to the fracture. The growth of voids is dominated by the spherical tensor of stress. The fracture surface is also consistent with the plane of the maximal principal stress in the macroscopic view. Figure 1(c) shows that the shape of voids has grown into an ellipsoid or a long strip, the local shear bands have been produced among ligaments of voids, and it is the propagation of local shear bands that leads to this kind of fracture. From Figure 1(d), the fracture surface seems smooth and there are almost no voids, but there are many shear bands on the fracture surface. The extension of shear bands leads to an integrated plastic shear fracture in the specimen. Compared with the shear fracture with void, voids have no influence on this kind of fracture, so this kind of fracture is not affected by the normal stress, while it is dominated by the shear stress instead. Therefore, it is necessary to set up fracture criterion separately for these four different fracture mechanisms, because the controlling parameters dominated their fracture initiation are completely different. For a certain kind of metal material, with the stress state gradually changing from triaxial tension to compression, if the stress triaxiality is applied to describe the stress state, that is, with the decreasing stress triaxiality at the weakest position in the specimen, the fracture mechanisms may change from quasicleavage fracture to normal fracture with void, shear fracture with void, and plastic shear fracture without void. For a certain metal, whether it is an uncracked body or cracked body, and no matter what loading conditions are, the fracture mechanisms will be similar as long as the values of stress triaxiality at the dangerous point are close. That is, from a mesoscopic fracture mechanism point of view, the essence of fracture in an uncracked body or in a cracked body is the same. For instance, Zuo et al. [26, 27] have demonstrated that for LY12 aluminium alloy, there are the same normal fracture zone and shear fracture zone on both the cup cone-shaped fracture surfaces of specimens in uniaxial tension and the fracture surfaces of specimens in I-II mixed mode loading, which illustrates that their macroscopic fracture modes are similar. Meanwhile, seen from the scanning electron micrograph (SEM) of the fractures, the essence of fracture in I-II mixed mode specimen and in uniaxial tension is also the same. In fact, a macrocrack exists in a component or a structure, and it is equivalent to that a special boundary condition is introduced in the component or structure. The crack boundary condition easily leads to the stress concentration near the crack tip, and thus complicated triaxial tensile stress field is generated in the component, which makes the value of stress triaxiality at the crack tip larger than that in uncracked components.

In real components, the amount of plastic deformation generated in the fracture process will be different with the properties of materials themselves and multiaxial states of stress loading conditions induced by both geometry changes and external loading varying. The influence of plastic deformation on fracture and damage is also known as a complicated problem existing in different views. Nevertheless, it is shown that the amount of plastic deformation generated in the process of fracture has a direct impact on fracture mechanisms through a lot of experiments in various stress states of many metal materials. For a certain metal, the strain incompatibility will emerge near the microdefects or second-phase particles in the material once the triaxial stress reaches an unacceptable magnitude, and then microcracks will occur, leading to the localized stress concentration. With the increasing plastic deformation during the fracture process of metals, four fracture mechanisms under various stress states can be concluded:

(1) When only a little plastic deformation appears during the fracture process, the stress concentration at the microcrack tips cannot be relaxed and is further intensified with the growth of the microcracks until the specimen fractures, quasicleavage fracture will occur in the specimen.

(2) Compared with (1), when a little more plastic deformation which can relax the stress concentration at microcrack tips produces during the fracture process, these microcracks will blunt. When they blunt wide enough, they will be evolved into ellipsoid whose minor axis along the loading direction or subspheroidal voids gradually. Growth and coalescence of voids finally leads to the fracture whose mechanism is normal fracture with void occurring in the specimen.

(3) When the plastic deformation appeared in the fracture process is even more than (2), the further development of stress centralization will be constrained, and the voids formed by blunted microcracks are hence not easy to coalesce along the loading direction, and then the shape of voids will develop into ellipsoid whose major axis is along the loading direction, a long strip, or a slender; However,

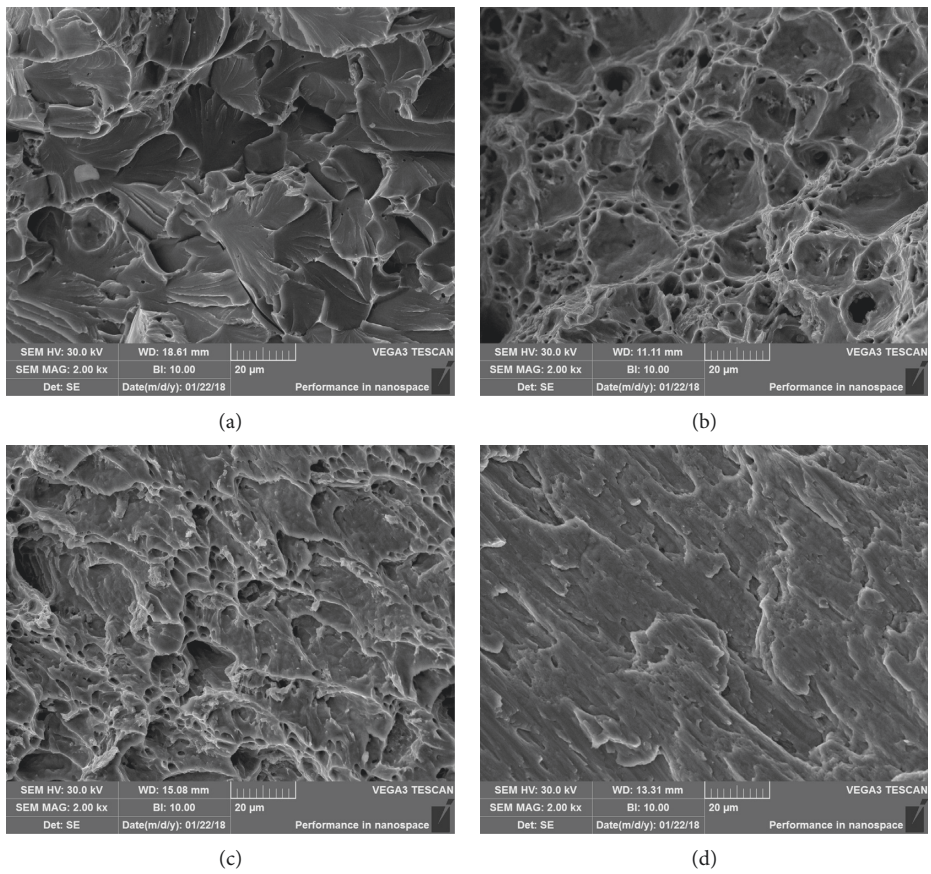

Figure 1: The SEM images of the typical fracture surfaces of four different fracture mechanisms: (a) quasicleavage fracture, (b) normal fracture with void, (c) shear fracture with void, and (d) shear fracture without void.

a large local plastic slip may produce local shear band among void ligaments, and propagation of shear bands will lead to shear fracture with void in the specimen.

(4) When the plastic deformation is too large to result in stress concentration in the specimen, voids cannot be produced; however, significantly continually large plastic slip will produce a lot of shear bands and lead to the integrated shear fracture in the specimen. Compared with shear fracture with void, voids have no influence on this kind of fracture; we therefore define this fracture mechanism as plastic shear fracture without void.

The amount of plastic deformation generated in the process of fracture will mainly depend on the stress states and the properties of materials such as grain size and grain uniformity, and the amount of plastic deformation will have a direct impact on the fracture mechanisms of metal materials. Therefore, for a given metal material, the fracture mechanisms may change from quasicleavage fracture to normal fracture with void, shear fracture with void, and plastic shear fracture without void with the decreasing stress triaxiality. Under the same stress state, the fracture mechanisms may also change according to the same rules with the grain size and grain uniformity improving. For a given metal material, the stress triaxiality R_σ can be regarded as a gauge to predict which fracture mechanism will occur, that is, there are three demarcation values of stress triaxiality between these four fracture mechanisms, and the relation can be quantified. It is assumed that R_1 is the demarcation value of stress triaxiality between quasicleavage fracture and normal fracture with void, R_2 is the demarcation value between normal fracture with void and shear fracture with void, and R_3 is the demarcation value between shear fracture with void and shear fracture without void for a certain kind of material. Then, if $R_\sigma \geq R_1$ at the weakest position, the fracture mechanism will be quasicleavage fracture; if $R_2 \leq R_\sigma < R_1$, the fracture mechanism will be normal fracture with void; if $R_3 \leq R_\sigma < R_2$, the fracture mechanism will be shear fracture with void; and if $R_\sigma < R_3$, the fracture mechanism will be shear fracture without void. The values of R_1, R_2, and R_3 are various for different materials.

3. Development of a New Fracture Criterion

3.1. Microscopic Analysis of Fracture Criterion. In the mesoscopic viewpoint, the fracture initiation of these four different mechanisms are dominated by dissimilar factors involving transgranular propagation of microcracks, nucleation, growth, and coalescence of voids, and extension of shear bands in metals; therefore, a proper modeling of these mechanisms at the mesoscale is the basis for the prediction of ductile fracture in real components and structures.

However, there are many physical quantities which can aspect the fracture process, including the dimension, the shape, and the orientation of the void, and the influence of initial inclusion and void distribution on fracture and the complexity of these quantities bring many difficulties to practical application. For this reason, the influencing parameters of fracture process with a viewpoint of statistically averaging will be discussed from a macroscopic view in this paper. These four mechanisms will be carefully analyzed, proper macroscopic parameters will be selected, and reasonable models will be proposed in this section, respectively.

3.1.1. Quasicleavage Fracture. For the quasicleavage fracture, transgranular propagation of microcracks leads to the occurrence of fracture. Microcracks initiate at interfaces of inclusions and second-phase particles with incompatible plastic deformation. A number of models have been proposed to explain the mechanism of microcrack propagation. However, it is difficult to explain the position and direction of microcrack initiation using the result of macroscopic stress field calculation, due to the existence of the microscopic tensile stress though the macroscopic mean stress is negative, the position and direction of microcracks initiation are possibly dominated by the microscopic stress fields, the microstructures of materials, and the directions of crystal interfaces. Nevertheless, through a large number of experiments [23], it is found that the direction of fracture surface is roughly consistent with the plane of the maximum tensile stress (the first principal stress which is positive) in the macroscopic view. The position of microcrack initiation is usually located in the place where the plastic deformation is incompatible, and it has been reported that the incompatible plastic deformation is caused by the stress concentration and triaxial tensile stress. From the analysis above, for the macroscopic modeling of quasicleavage fracture, the position of microcrack initiation can be considered as the position where the stress triaxiality is largest in the stress field, and the direction of microcracks initiation can be thought of as the plane of the maximum tensile stress. Consequently, the initiation of quasicleavage fracture can be modeled as a function of the stress triaxiality and the first principal tensile stress.

3.1.2. Normal Fracture with Void. For normal fracture with void, most microcracks have developed into voids, so the growth and coalescence of voids lead to the fracture. Void growth is mainly influenced by the mean stress according to the experimental observation [11]. High mean stress accelerates void growth, while negative mean stress suppresses void growth, thereby delaying fracture. Coalescence of voids is the final stage of normal fracture with void. Different coalescence modes of voids may lead to different fracture mechanisms and macroscopic fracture surfaces. For this kind of fracture, the coalescence mode is the necking of the ligaments between voids caused by the highest principal stress. Thus, the mean stress can be seen as the dominating factor regulating isotropic growth and the rate of coalescence of voids. Accordingly, the mean stress is adopted to describe the normal fracture with void caused by void growth and coalescence here. Meanwhile, through a large number of experiments [23], it is found that the fracture surface is obviously consistent with the plane of the maximal tensile stress in the macroscopic view. The position of fracture initiation is usually located in the place where the stress triaxiality is the largest because the degree of growth and coalescence of voids in this position is the highest. From the analysis above, for the macroscopic modeling of normal fracture with void, the position of fracture initiation can also be considered as the position where the stress triaxiality is the largest in the stress field, and the direction of fracture initiation can also be thought of as the plane of the maximum tensile stress. Consequently, the initiation of normal fracture with void is modeled as a function of the mean stress and the first principal tensile stress.

3.1.3. Shear Fracture with Void. For the shear fracture with void, because the large plastic deformation in the process of fracture can relax the stress concentration near the voids, the voids are difficult to grow and coalesce along the direction of the maximum tensile stress. Therefore, the shape of voids will grow into an ellipsoid or a long strip, and local shear bands will be produced among ligaments of voids, thus shear-linking up of voids along the direction of the maximal shear stress, and the propagation of shear bands are what lead to this kind of fracture. Since shear fracture with void is caused by the maximal shear stress and also affected by growth and coalescence of voids, it is modeled by the maximal shear stress and the stress triaxiality. The position of fracture initiation can also be considered as the position where the stress triaxiality is the largest in the stress field because the shear-linking up of voids is still the main mechanism of this kind of fracture, and the direction of fracture initiation can be thought of as the plane of the maximal shear stress.

3.1.4. Shear Fracture without Void. For the plastic shear fracture without void, there are almost no voids, but many shear bands on the fracture surface. The propagation of shear bands along the direction of the maximal shear stress leads to this kind of fracture. Compared with the shear fracture with void, voids have no influence on this kind of fracture, so it is not affected by the normal stress and is only controlled by the maximal shear stress. Since shear fracture without void is caused by the maximal shear stress, it is directly modeled by the maximal shear stress. Meanwhile, it is also found that the fracture surface is obviously consistent with the plane of the maximum shear stress in the macroscopic view [23]. Because the propagation of shear bands is the main mechanism of this kind of fracture and the propagation of shear bands is driven by maximal elastic shear stress, the position where the shear stress is largest should be the weakest. Many reports have shown that the distribution of elastic shear stress is usually similar to the distribution of Von Mises equivalent stress in the stress field. Therefore, the position of fracture initiation can be considered as the position where the Von Mises equivalent stress is largest in the stress field, and the

direction of fracture initiation can be thought of as the plane of the maximal shear stress.

3.2. A New Fracture Criterion for Prediction of Fracture Initiation. Based on the microscopic analysis of the four different fracture mechanisms, a new fracture criterion is proposed with selected models to describe the fracture initiation of different mechanisms in the form of equations (1)–(3).

For quasicleavage fracture and normal fracture with void, based on considerations discussed above, the maximal tensile stress is a leading factor which dominates the occurrence of fracture, and the influence of the stress triaxiality is considered; the fracture criterion can be given by

$$f_1(\sigma_{ij}) = \sigma_1 + b_1(\sigma_2 + \sigma_3) = c_1, \quad \text{when } R_\sigma \geq R_2, \tag{1}$$

where b_1 represents the influence coefficient, c_1 denotes the critical value of equivalent stress $f_1(\sigma_{ij})$ corresponding to the onset of fracture initiation, and R_2 is the demarcation value between normal fracture with void and shear fracture with void. In this fracture criterion, equation (1) is used to predict the initiation of the quasicleavage fracture and normal fracture with void; it is assumed that the weakest position is located in the position where the stress triaxiality is largest in the stress field, and the direction of fracture initiation is consistent with the plane of the maximum tensile stress at the weakest position. When the stress triaxiality of the weakest position in the specimen is more than or equal to R_2, the fracture mechanism will be normal fracture with void or quasicleavage fracture. The quasicleavage fracture and normal fracture with void is assumed to be proportional to the mean stress and stress triaxiality, and the influence coefficients b_1 is introduced to equation (1) to modulate the different effect of the stress triaxiality on fracture initiation of the quasicleavage fracture and normal fracture with void.

Shear fracture with void which is mainly caused by shear-linking up of voids and evolution of local shear bands is dominated by the maximal shear stress and influenced by stress triaxiality, so the corresponding fracture function is given by

$$f_2(\sigma_{ij}) = \tau_{\max} + b_2(R_\sigma - R_3) = c_2, \quad \text{when } R_3 \leq R_\sigma < R_2, \tag{2}$$

where b_2 denotes the influence of stress state on shear fracture with void for different materials, c_2 is the critical value of equivalent stress $f_2(\sigma_{ij})$ corresponding to the onset of fracture initiation, and R_3 is the demarcation value between shear fracture with void and shear fracture without void. Equation (2) is used for shear fracture with void, and it is supposed that the weakest position is also located in the position where the stress triaxiality is largest, and the direction of fracture initiation is consistent with the plane of the maximum shear stress at the weakest position. When $R_3 \leq R_\sigma < R_2$, the fracture mechanism will be shear fracture with void. The shear fracture with void is represented by a function of the stress triaxiality and maximal shear stress, and b_2 is introduced to equation (2) to model the different effect of the stress triaxiality on fracture initiation of the shear fracture with void.

Shear fracture without void is usually dominated by the propagation of shear bands. Based on considerations discussed above, the associated fracture function for predicting the shear fracture without void can be written in the form:

$$f_3(\sigma_{ij}) = \tau_{\max} = c_3, \quad \text{when } R_\sigma < R_3, \tag{3}$$

where c_3 is the critical equivalent stress $f_3(\sigma_{ij})$ corresponding to the onset of shear fracture without void, and when $R_\sigma < R_3$, the fracture mechanism is shear fracture without void. Equation (3) is used for shear fracture without void, with the assumption that the weakest position is located in the position where the Von Misses equivalent stress is largest in the stress field, and the direction of fracture initiation is consistent with the plane of the maximum shear stress at the weakest position. The shear fracture without void is described only by the maximal shear stress.

According to this fracture criterion, fracture initiates when the equivalent stress $f_i(\sigma_{ij})$ in equations (1)–(3) at the weakest position in the specimen reaches the critical equivalent stress c_i level, and the weakest position and the fracture initiation direction can also be predicted. The form above can be easily implemented into numerical analysis to describe fracture in complex loading conditions.

The existing fracture theory of metal material is divided into traditional strength theory and fracture mechanics due to some human factors, and then uncracked and cracked bodies are discussed by them, respectively. However, from a mesoscopic fracture mechanism point of view, the essence of fracture in an uncracked body or in a cracked body is the same. To a microelement, if the fracture mechanisms are the same, the fracture criterion should be similar, that is, the fracture criterion just depends on the stress state and deformation process of this microelement and is irrelevant to whether it is located in the cracked or uncracked component. Furthermore, an ideal crack does not exist in reality, crack tip blunts inevitably due to the occurrence of plastic deformation after loading especially for materials with good ductility, then the stress and strain at crack tip must be bounded; as a consequence, the crack propagation criterion is essentially related in the traditional strength theory. The fracture criterion proposed in this paper was based on mesoscopic fracture mechanisms of different kinds of metals in various stress states and could be applicable to different fracture mechanisms of uncracked and cracked bodies.

3.3. Parametric Study

3.3.1. Effect of the Material Constant b_1. The material constant b_1 modulates effect of the stress triaxiality on growth and coalescence of voids before the occurrence of normal fracture with void. As b_1 becomes large, influence of the stress triaxiality on fracture initiation increases, and the maximal tension stress at fracture reduces. Effects of b_1 are presented in the space of the stress triaxiality and the maximal principal stress in Figure 2. We assume that $c_1 = 500$ MPa and keep c_1

constant, and the relationships between the maximal tension stress σ_1 (y axis) and the stress triaxiality ($R_\sigma - R_2$) (x axis) are shown in Figure 2 when b_1 equals to 0.1, 0.2, 0.3, 0.4, and 0.5, respectively. As Figure 2 illustrates, the maximal tension stress at fracture is lower at high stress triaxiality than that at the low stress triaxiality, and the change rate of maximal tension stress increases with b_1 increasing from 0.1 to 0.5. This also matches well with the mesoscopic analysis of normal fracture with void in Section 3.1.2, in which high stress triaxiality promotes void growth and coalescence, thereby accelerating normal fracture with void. The effects of stress triaxiality on fracture initiation of distinct materials are different; therefore, b_1 is a material constant. Without the effect of the stress triaxiality, the maximal tension stress at fracture will be identical for different stress states. In fact, the maximal tension stress at fracture reduces with the increase of the stress triaxiality, and a curved relationship between the maximal tension stress at fracture and stress triaxiality has been shown in many reports [19]; however, the fracture criteria with single parameter cannot reflect this curved relationship. In equation (1), the introduction of the material constant b_1 into the fracture criterion can describe the linear relation between the maximal tension stress at fracture and the stress triaxiality, which can approximately substitute the curved relationship mentioned above. Therefore, this fracture criterion can be used for predicting all the fracture initiation whose mechanism is quasicleavage fracture or normal fracture with void in different stress states.

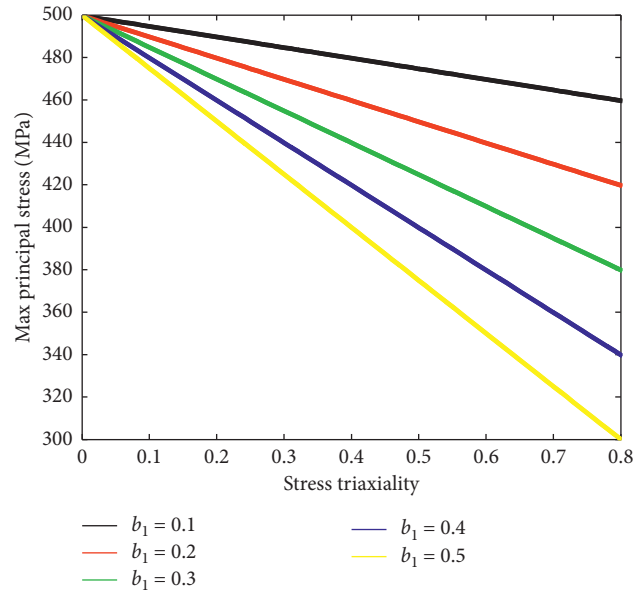

Figure 2: Effect of b_1 in the space of the stress triaxiality and maximal principal stress.

3.3.2. Effect of the Material Constant b_2. The role of the material constant b_2 is quite similar to that of b_1. The material constant b_2 modulates the effect of the stress triaxiality on fracture initiation of shear fracture with void. We keep c_2 constant and assume that $c_2 = 500$ MPa, and the relationship between the maximal shear stress $\tau_{\max}$ (y axis) and the stress triaxiality ($R_\sigma - R_3$) (x axis) is shown in Figure 3 when b_2/c_2 equals to 0.1, 0.2, 0.3, 0.4, and 0.5, respectively. As Figure 3 illustrates, the maximal shear stress at fracture is lower at high stress triaxiality than that at the low stress triaxiality, and the change rate of maximal shear stress increases with b_2/c_2 increasing from 0.1 to 0.5. Without the effect of the stress triaxiality, the fracture stress will be identical for the same maximal shear stress in different stress states, as proved in equation (3) when $b_2 = 0$.

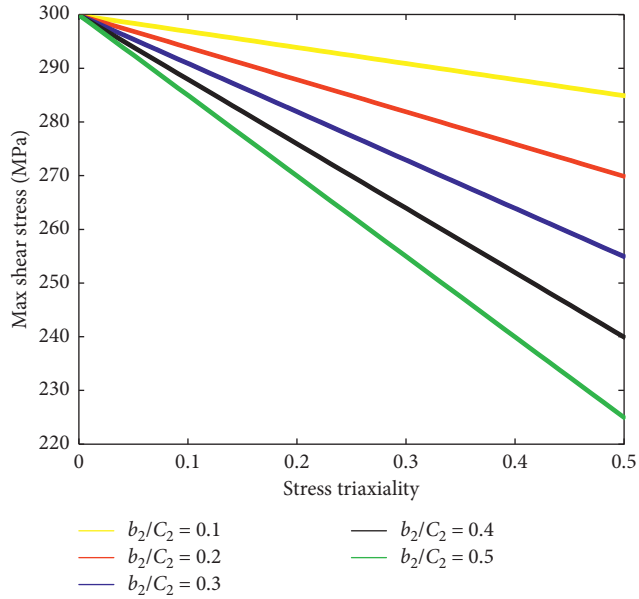

Figure 3: Effect of b_2 in the space of the stress triaxiality and maximal shear stress.

3.4. Calculation of Material Constants. There are five material constants in the new fracture criterion: b_1, b_2, c_1, c_2, and c_3. These material constants should be determined by experimental results. The common tests to be carried out for metal materials include uniaxial tensile test, torsion test, uniaxial compression test, combined tension-torsion test, and the mixed mode fracture test. In each loading condition, the principal stresses σ_1, σ_2, and σ_3, the stress triaxiality R_σ, and the maximal shear stress $\tau_{\max}$ at the weakest position can be calculated, so the new fracture criterion is reduced to a simple equation. If the mechanism is quasicleavage or normal fracture with void, the new fracture criterion is reduced to a simple equation in forms of b_1 and c_1; if the mechanism is shear fracture with void, the new fracture criterion is reduced to a simple equation in forms of b_2 and c_2; and if the mechanism is shear fracture without void, the new fracture criterion is reduced to a simple equation in form of c_3. Therefore, the material constants b_1 and c_1 in equation (1) should be calculated by considering at least two experimental data points within the range from quasicleavage fracture to normal fracture with void, and the material constants b_2 and c_2 in equation (2) should be calculated using at least two experimental data points at the range of shear fracture with void and at least one

experimental data point is required to calculate c_3 in equation (3) at the range of shear fracture with void. Moreover, more experimental data points are preferred to construct a fracture locus with high accuracy. Therefore, an optimization method is suggested to calculate these material constants such as the least square method (LSM) using more experimental data points at the range of a certain fracture mechanism.

For the material constant b_1, it should be a positive value of greater than 0 and less than 1. This is because that the material constant b_1 is defined as the influence coefficient which describes the extent of the impact of stress triaxiality on normal fracture with void. It may be justified that the critical equivalent stresses c_1, c_2, and c_3 should be varied with materials and should be constant for a certain material. For the stress triaxiality demarcation values between these four fracture mechanisms R_1, R_2, and R_3, they are also material constants and can be determined by a series of experiments in a wide range of stress states.

4. Experiment Calibration and Verification

4.1. Application to the Prediction of QT400 Nodular Cast Iron

4.1.1. Experiments. The material used is the nodular cast iron bar of QT400-15. Combined tension-torsion tests were carried out using smooth axisymmetric specimens with a gauge length of 50 mm and a cross section diameter of 10 mm. A comprehensive investigation of the fracture surfaces obtained in the tests of different tension-torsion ratios (and thus under various stress states) is carried out by using the scanning electron microscope at both low and high magnification. The overall features are observed at low magnification, while more details revealing the fracture mechanisms are observed at higher magnifications. In all the combined tension-torsion tests with different tension-torsion ratios, unnoticeable necking was present until the loads increased to their ultimate strengths, and the fracture surfaces were in the plane with different angles to the axis of specimen. The macroscopic fracture surface is shown in Figure 4. On a microscopic scale, Figures 5(a)–5(d) give the SEM images of the fracture surfaces in the combined tension-torsion tests with different tension-torsion ratios, respectively. All these figures demonstrate that lateral growth and coalescence of voids dominated the fracture, and all the fracture modes in the combined tension-torsion tests with different tension-torsion ratios are normal fracture with void. The experimental data points and the angles between fracture surfaces and the cross section of specimen measured in the tests with different tension-torsion ratios are shown in Table 1.

In Table 1, P/T denotes the ratio of tensile load to torsion moment setting in the experiment, P_b and T_b represent the tensile load and the torsion moment at fracture, respectively, φ_1 is the angle between the fracture surface and the cross section measured in the test, φ_2 is the angle between the plane of σ_1 at the fracture initiation point and the cross section, and R_σ is the value of stress triaxiality at the weakest point. The results in Table 1 showed that the fracture surface is consistent with the plane of the maximal tension stress σ_1.

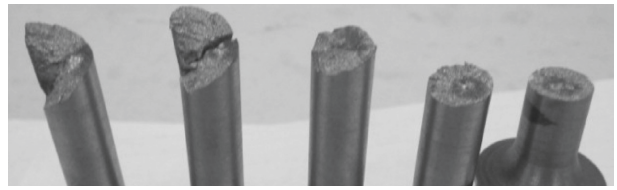

Figure 4: The macroscopic fracture surfaces of QT400-15 nodular cast iron in the tests of different stress states ranging from uniaxial tension to torsion.

4.1.2. Comparison of Predictions with Experimental Results. Since all the fracture mechanisms in combined tension-torsion tests of different ratios are normal fracture with void, equation (1) is utilized for the fracture prediction. Material constants b_1 and c_1 in the new fracture criterion are calculated by the least square method using all the experimental data points in Table 1: $b_1 = 0.09$, $c_1 = 535.8$ MPa. Therefore, the new fracture criterion for QT400-15 has a form of

$$f_1(\sigma_{ij}) = \sigma_1 + 0.09(\sigma_2 + \sigma_3) \le 535.8, \quad \text{when } 0 \le R_\sigma \le 1/3. \tag{4}$$

Equation (4) can be utilized for fracture prediction of QT400-15 in any stress states in the range from quasi-cleavage fracture to normal fracture with void. That is, for the quasicleavage fracture and normal fracture with void in any stress states, when the equivalent stress $f_1(\sigma_{ij})$ at the fracture initiation point reaches its critical value c_1, the fracture initiation will occur. The equation of error calculation can be expressed as

$$\eta = \frac{f_1(\sigma_{ij}) - c_1}{c_1} \times 100\%, \tag{5}$$

where η denotes the error between the experimental point and the result calculating from the new criterion. The predicted results of equivalent stress $f_1(\sigma_{ij})$ are compared with the experimental data points in Table 2, and the predicted results of fracture direction are compared with experimental results in Table 1. The comparison clearly demonstrates that the predicted results by the new criterion are very close to the experimental data points from the torsion to the uniaxial tension.

4.2. Application to Predict the Fracture Direction and the Fracture Initiation Position of LY12 Aluminium Alloy

4.2.1. Experimental Results. Zuo [26, 27] carried out I-II mixed mode fracture tests using compact tension-shear specimen on aluminium alloy LY12-M (annealed) and LY12-CZ (quenched) covering a wide range of the stress triaxialities which provide a clear clue to the effect of the stress triaxiality on the fracture initiation direction and the fracture initiation point of different mechanisms. The test results showed that, for the LY12-CZ aluminium alloy, with

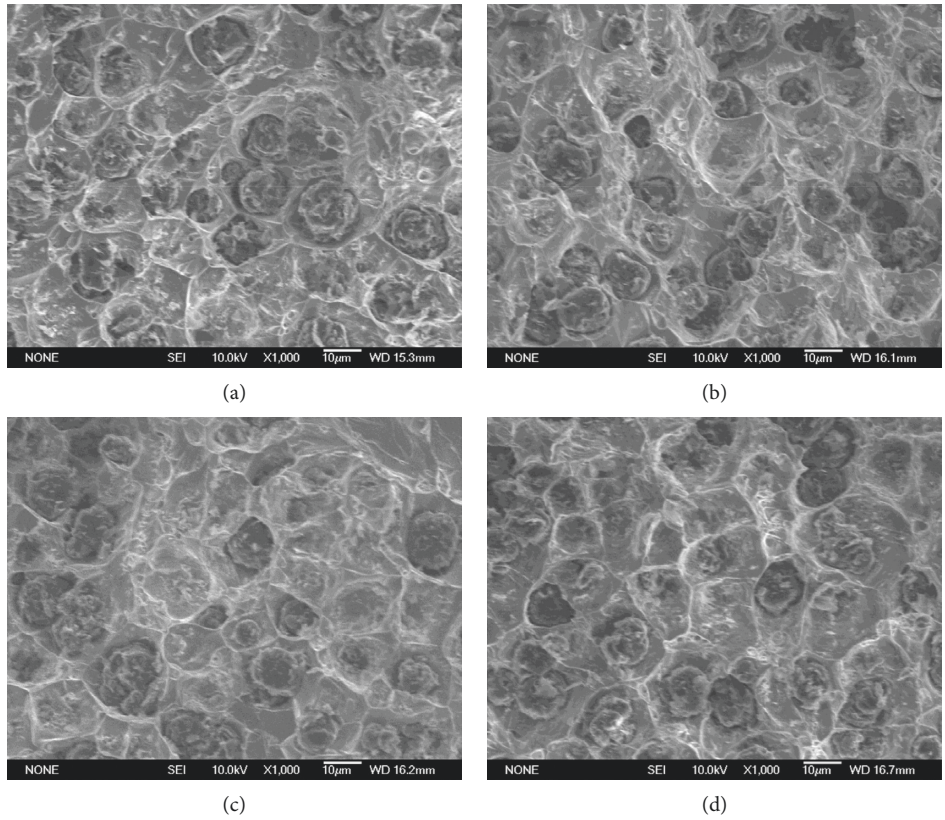

Figure 5: SEM images of fracture surfaces for QT400 nodular cast iron in combined tension-torsion tests with different tension-torsion ratios on the fracture surface of the specimen with tension-torsion ratio (a) $P/T = 0.0$, (b) $P/T = 0.17$, (c) $P/T = 0.38$, and (d) $P/T = 0.72$.

Table 1: The experimental data points of QT400-15 nodular cast iron in combined tension-torsion tests.

P/T	0.0	0.17	0.38	0.72	∞
P_b (kN)	0.0	15.5	25.3	34.4	42.1
T_b (N·m)	115.5	90.3	66.7	47.2	0.0
σ_1 (MPa)	588.5	568.6	555.0	544.4	536.6
σ_2 (MPa)	0	0	0	0	0
σ_3 (MPa)	−588.5	−371.6	−214.4	−106.2	0.0
R_σ	0.0	0.08	0.16	0.24	0.33
φ_1 (°)	42	38	32	22	0
φ_2 (°)	45	39	33	24	0

Table 2: The error calculation of the new fracture criterion in different stress states.

P/T	0.0	0.17	0.38	0.72	∞
R_σ	0.0	0.08	0.16	0.24	0.33
σ_1 (MPa)	588.5	568.6	555.0	544.4	536.6
σ_2 (MPa)	0	0	0	0	0
σ_3 (MPa)	−588.5	−371.6	−214.4	−106.2	0
$f_1(\sigma_{ij})$ (MPa)	535.5	535.2	535.7	534.8	536.6
η (%)	0.06	0.11	0.02	0.19	0.15

the loading conditions changing from mode I to mode II, the positions of crack initiation were always located in the blunted zone, the fracture mechanisms were normal fracture with void, and the angles between the direction of crack initiation and the original crack surface changed from 0° to −64.5°. For the LY12-M aluminium alloy, with the loading conditions changing from mode I to mode II, the positions of crack initiation were also always located in the blunted zone; however, in the loading condition of mode I, the fracture mechanism was normal fracture with void, the direction of crack initiation was along the original crack surface, while in the loading condition of mode II, the mechanism was shear fracture with void, and fracture surface was in the plane making the angle of −21° with the original crack surface, and in the loading condition of I/II mixed mode, the two mechanisms coexisted on the fracture surface [26, 27].

4.2.2. Comparison of Predictions with Experimental Results. The distributions of stress triaxiality, maximal principal stress, and maximal shear stress in the specimen are calculated in ANSYS using the real blunted model. Figures 6(a)–6(e) show the distributions of the stress triaxiality at the crack tip with the loading conditions changing from mode I ($\beta_{eq} = 90°$) to mode II ($\beta_{eq} = 0°$), respectively. Table 3 gives the position of maximal triaxiality at the crack tip and the direction of the maximal principal stress and the direction of the maximal shear stress at the position where the maximal stress triaxiality is located in the loading conditions from mode I to mode II. In Table 3, θ is the angle between the original crack and the line from the original crack tip to the point where the maximal stress triaxiality is

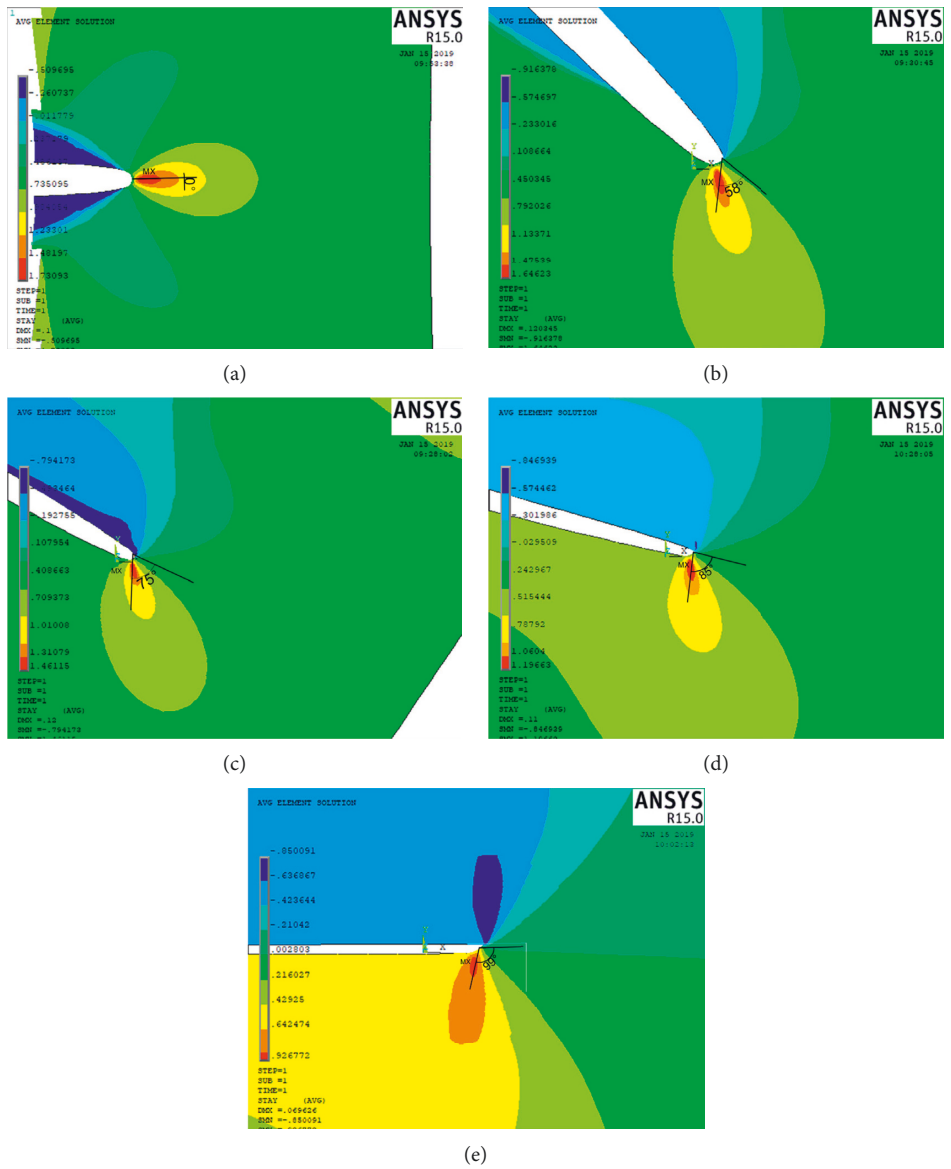

FIGURE 6: The distribution of stress triaxiality at the crack tip in the loading conditions of (a) mode I ($\beta_{eq} = 90^{\circ}$), (b) mixed mode I/II ($\beta_{eq} = 45^{\circ}$), (c) mixed mode I/II ($\beta_{eq} = 30^{\circ}$), (d) mixed mode I/II ($\beta_{eq} = 15^{\circ}$), (e) mode II ($\beta_{eq} = 0^{\circ}$).

TABLE 3: The position of maximal triaxiality at crack tip and the maximal principal stress and the maximal shear stress at the position where the maximal stress triaxiality is located in the loading conditions from mode I to mode II.

Loading condition	$\theta(^{\circ})$	$\alpha_1(^{\circ})$	$\alpha_2(^{\circ})$
$\beta_{eq} = 90^{\circ}$(mode I)	0	0	45
$\beta_{eq} = 45^{\circ}$	−58	−49.4	−4.4
$\beta_{eq} = 30^{\circ}$	−75	−55.7	−10.7
$\beta_{eq} = 15^{\circ}$	−85	−60.4	−15.4
$\beta_{eq} = 0^{\circ}$(mode II)	−99	−65.2	−20.2

located, α_1 is the angle between the original crack surface and the surface of the maximum principal stress at the point where the maximal stress triaxiality is located, and α_2 is the angle between the original crack surface and the surface of the maximum shear stress at the point where the maximal stress triaxiality is located, and the schematic diagram between θ and α is shown in Figure 7. The calculation results show that, with the loading conditions changing from mode I to mode II, the positions of the maximum stress triaxiality R_{σ} are always located in the blunted zone at the crack tip, and the angles between the original crack surface and the line from the original crack tip to the point where the maximal stress triaxiality is located change from 0° to -99°, and the maximal principal stress at the position where the maximal stress triaxiality is located was in the plane making the angle changing from $0^{\circ}$to $-65.2^{\circ}$with the original crack surface. In the loading condition of mode II, the maximal shear stress at the position where the maximal stress triaxiality is located was in the plane making the angle of $-20.2^{\circ}$with the original crack surface.

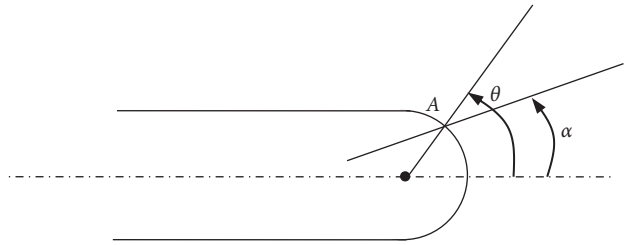

Figure 7: The schematic diagram of the relationship between θ and α.

For LY12-CZ, with the loading conditions changing from mode I to mode II, since the fracture mechanism is normal fracture with void, equation (1) is applied to predict the fracture direction and the fracture initiation point. A good match of the positions of the maximum stress triaxiality R_σ and the fracture initiation points has been shown, as well as of the plane of the maximal principal stress and the direction of fracture initiation. For LY12-M, equation (1) is utilized for the fracture prediction in the loading condition of mode I, while equation (2) is used for the fracture prediction in the loading condition of mode II. Compared with the experimental results, in the condition of mode I, the fracture initiation point and the fracture direction are predicted by equation (1) of the new criterion, i.e., the position of the maximum stress triaxiality R_σ and the plane of the maximal principal stress are consistent with the experimental results, and the fracture direction predicted by equation (2), i.e., the plane of the maximal shear stress is close to the fracture direction observed in the loading condition of mode II. The direction of crack initiation and the plane of the maximal principal stress at the fracture initiation point in the loading condition of mode I are compared in Figure 8(a), and the direction of crack initiation and the plane of the maximal shear stress at the fracture initiation point in the loading condition of mode II are compared in Figure 8(b). The comparison clearly demonstrates that the fracture directions and fracture initiation positions predicted by the new criterion are close to the experimental measurements from mode I to mode II.

4.3. Application to Predict the Fracture Direction and the Crack Initiation Position of HY130 Steel

4.3.1. Experimental Results. Maccagno [24] carried out mixed mode I/II testing on HY130 steel at room temperature. The SEM of the fracture surface near the slit front of the specimen loaded to $\beta_{eq} = 90^\circ$ (mode I) showed that the surface consists of many shallow parabolic dimples, while the SEM of the fracture surface near the slit front of the specimen loaded to $\beta_{eq} = 45^\circ$ and lower exhibits grooves. The results for the fracture angle and the appearance of parabolic dimples on the fracture surfaces suggest that mixed mode I/II fracture of the HY130 steel tested at room temperature occurs with the mechanism of shear fracture and in the direction of maximum shear. However, through the comparison of the fracture surfaces for the specimen loaded with $\beta_{eq} = 90^\circ$ (mode I) and $\beta_{eq} = 45^\circ$ and lower, it is found that parabolic dimples are such a dominant feature on the fracture surface of the specimen loaded to $\beta_{eq} = 90^\circ$, while localized shear bands are dominate to the specimen loaded to $\beta_{eq} = 45^\circ$ and lower, suggesting that the crack initiation mechanisms changed from shear fracture with void to shear fracture without void in the range from mode I to mode II gradually [1, 24].

For the direction of crack initiation, the test results showed that, the specimen loaded to $\beta_{eq} = 90^\circ$ (mode I) shows the zig-zag profile which fails by a shear mechanism, and the angle between the slit and the initial portion of the crack propagation (i.e., the fracture angle) is about 45°. The specimens loaded to $\beta_{eq} = 75^\circ$ and 60° also exhibit zig-zag fracture profiles, and the initial fracture angles for these specimens are about 35° and 20°, respectively. For all the specimens loaded to $\beta_{eq} = 45^\circ$ and lower, the fracture profiles reveal no tendency to zig-zag, and the trend is for the fracture angle to decrease with increasing mode II.

4.3.2. Comparison of Predictions with Experimental Results. The experimental results of HY130 indicated that none of the common mixed mode I/II fracture criteria (discussed in ref. [24]) can be used to describe this behavior, and the fact also emphasizes that the fracture mechanisms and the fracture criterion must be consistent with each other.

For HY130 steel, with the loading conditions changing from mode I to mode II, that is, with the decreasing stress triaxiality at the crack tip in the specimen, the crack initiation mechanisms changed from shear fracture with void to shear fracture without void; therefore, equation (2) is utilized for the fracture prediction in the loading conditions of $\beta_{eq} = 90^\circ$, 75°, and 60°, and equation (3) can be used for the fracture prediction in the loading conditions of $\beta_{eq} = 45^\circ$ and lower. Compared with the experimental results, in the condition of $\beta_{eq} = 90^\circ$, the crack initiation point and the fracture direction predicted by equation (2) of the new criterion, i.e., the position of the maximum stress triaxiality R_σ and the plane of the maximal shear stress, are consistent with the experimental results, and the fracture initiation point and the fracture direction predicted by equation (3), i.e., the position of the maximum Mises equivalent stress and the plane of the maximal shear stress, are also close to the fracture direction observed in the loading conditions of $\beta_{eq} = 45^\circ$ and lower. The comparison clearly demonstrates that the rule of fracture mechanism changing with the stress triaxiality, crack initiation positions and fracture directions predicted by the new criterion are very close to the experimental measurements from mode I to mode II.

Moreover, it is interesting to note that lightly tempered HY130 tested at room temperature fractures by a shear mechanism, while HY130 in the identical condition but tested at −196°C fractures by a cleavage mechanism. The fracture in all specimens of HY130 tested at −196°C loaded from $\beta_{eq} = 90^\circ$ to $\beta_{eq} = 60^\circ$ was by transgranular cleavage, while for the specimens loaded to $\beta_{eq} = 45^\circ$ and lower, a dimpled region was observed, and the SEM of fracture surface indicated the mechanism changed into normal fracture with void. It is also suggested that the crack

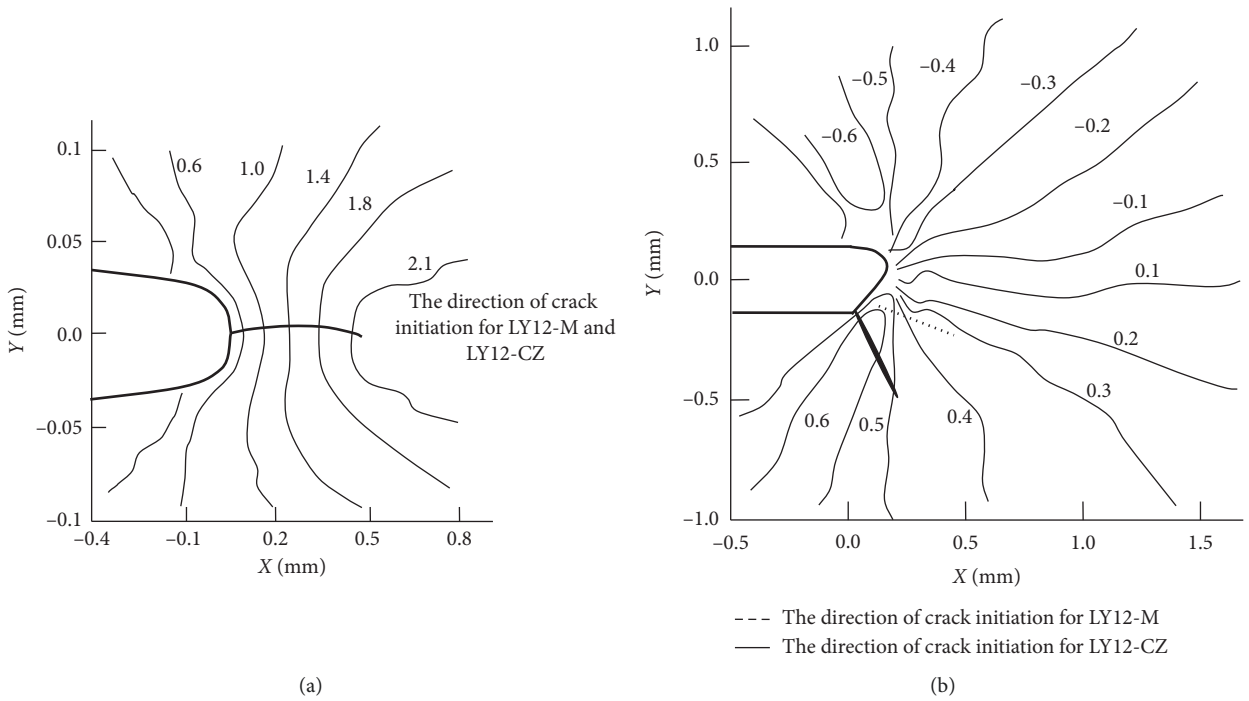

Figure 8: The schematic diagrams of relationship between the direction of crack initiation and the distribution of stress triaxiality in the loading condition of (a) mode I (b) mode II.

initiation mechanisms changed from quasicleavage to normal fracture with void in the range from mode I to mode II with the stress triaxiality decreasing. These findings serve to emphasize that the rule of fracture mechanism changing with the stress triaxiality predicted by the new criterion is reasonable, and no single fracture criterion can be expected to describe all types of crack propagation in complex loading situations. The actual microscale processes involved during fracture must be considered, and the criterion must be consistent with these processes.

4.4. Discussions. As what mentioned before, the amount of plastic deformation generated in the process of fracture will have a direct impact on the fracture mechanisms of metal materials. The amount of plastic deformation will mainly depend on the stress state and the property of the material itself. From the mixed mode I/II test results on LY12-CZ and LY12-M aluminium alloy at room temperature and HY130 steel at room temperature and −196°C, with the loading conditions changing from mode I to mode II, that is, with the decreasing stress triaxiality at crack tip in the specimen, for HY130 steel at −196°C, the crack initiation mechanisms changed from cleavage to normal fracture with void; for LY12-CZ aluminium alloy at room temperature, the crack initiation mechanism was normal fracture with void; for LY12-M aluminium alloy at room temperature, the crack initiation mechanism changed from normal fracture with void to shear fracture with void; and for HY130 steel at room temperature, the crack initiation mechanism changed from shear fracture with void to shear fracture without void. Obviously, under the same loading condition, with the plastic deformation capacity of the material improving, the amount of plastic deformation generated in the process of fracture increased, and the fracture mechanisms also changed regularly from quasicleavage fracture to normal fracture with void, shear fracture with void, and shear fracture without void.

5. Conclusions

The fracture mechanisms of metal materials changed regularly influenced by varied stress states and different material characteristics. The major fracture mechanisms of metal materials can be divided into four types including quasicleavage fracture, normal fracture with void dominated by nucleation, growth, and coalescence of voids, shear fracture with void caused by propagation of local shear bands among void ligaments and influenced by voids, and shear fracture without void driven by unstable slip of shear bands to both uncracked and cracked bodies. Different fracture modes correspond to various physical mechanisms, and the dominant factors resulting in the fracture initiation will also be different for different fracture mechanisms.

The maximum tensile stress is a dominant factor for initiation of normal fracture, and the maximum shear stress for shear fracture. Nevertheless, different fracture mechanisms were not clearly separated in existing fracture theories, so the corresponding fracture criteria cannot readily be fitted to different fracture mechanisms. Therefore, the influences of different mechanisms on fracture initiation are fully considered for establishing the fracture criteria, and it will be more accurate to predict fracture initiation of metal materials.

A fracture criterion is newly proposed with consideration of different fracture mechanisms including quasicleavage fracture, normal fracture with void, shear fracture with void, and shear fracture without void. These four different mechanisms are described as different functions of the stress triaxiality, the principal stress, and the maximal shear stress. Quasicleavage fracture and normal fracture with void are described as a function of the principal stress, shear fracture with void is a function of the stress triaxiality and maximal shear stress, and shear fracture without void is only controlled by the maximal shear stress. The new fracture criterion is successfully applied to predict the fracture initiation location and the fracture direction of nodular cast iron QT400-15 from the uniaxial tension to the torsion. Comparison of the predicted fracture equivalent stress by the new fracture criteria to the experimental data demonstrates the high accuracy of the new fracture criterion. The crack initiation site and the direction of crack initiation of LY12 aluminium alloy and HY130 steel in I/II mixed mode fracture tests can also be properly estimated by the new fracture criterion.

The fracture criterion constructed in this paper with consideration of different fracture mechanisms, reflecting mesoscopic mechanisms with macroscopic statistical parameters, is a better supplement to the deficiency of fracture mechanics in solving mixed mode fracture problems and also a better amendment to application of traditional strength theory in complicated stress states can be applied to predict fracture initiation of cracked and uncracked metal specimen.

This paper outlines the preliminary results of the fracture criteria for predicting the fracture initiation based on different fracture mechanisms of the metal materials under various stress states. Further experimental and numerical studies will be conducted to validate the present conclusions and determine their applicability and accuracy for other metal materials.

Data Availability

The data (test data including SEM images, fracture images, and other test data) used to support the findings of this study are available from the corresponding author upon request. Previously reported (test data) data were used to support this study and are available at https://doi.org/10.1016/0956-7151(94)90385-9, https://doi.org/10.1016/0013-7944(92)90233-5, and http://www.wanfangdata.com.cn/details/detail.do?_type=degree&id=Y220521. These prior studies are cited at relevant places within the text as references [1, 24, 27].

Conflicts of Interest

The authors declare that they have no conflicts of interest.

Acknowledgments

This work was supported by the Natural Science Foundation of China (grant no. 11302167) and the Science and Technology Project in Baoji (grant no. 2018JH-26).

References

[1] D. Bhattacharjee and J. F. Knott, "Ductile fracture in HY100 steel under mixed mode I/mode II loading," *Acta Metallurgica et Materialia*, vol. 42, no. 5, pp. 1747–1754, 1994.

[2] Y. Bao and T. Wierzbicki, "A comparative study on various ductile crack formation criteria," *Journal of Engineering Materials and Technology*, vol. 126, no. 3, pp. 314–324, 2004.

[3] T. Wierzbicki, Y. B. Bao, Y. W. Lee, and Y. Bai, "Calibration and evaluation of seven fracture models," *Int J Mech Sci*, vol. 47, no. 4-5, pp. 719–743, 2005.

[4] T. B. Stoughton and J. W. Yoon, "A new approach for failure criterion for sheet metals," *International Journal of Plasticity*, vol. 27, no. 3, pp. 440–459, 2011.

[5] M. Dunand and D. Mohr, "On the predictive capabilities of the shear modified Gurson and the modified Mohr-Coulomb fracture models over a wide range of stress triaxialities and Lode angles," *Journal of the Mechanics and Physics of Solids*, vol. 59, no. 7, pp. 1374–1394, 2011.

[6] G. Trattnig, T. Antretter, and R. Pippan, "Fracture of austenitic steel subject to a wide range of stress triaxiality ratios and crack deformation modes," *Eng Fract Mech*, vol. 75, no. 2, pp. 228–235, 2008.

[7] A. L. Gurson, "Continuum theory of ductile rupture by void nucleation and growth: Part I-yield criteria and flow rules for porous ductile media," *Journal of Engineering Materials and Technology*, vol. 99, no. 1, pp. 2–15, 1977.

[8] V. Tvergaard and A. Needleman, "Analysis of the cup-cone fracture in a round tensile bar," *Acta Metallurgica*, vol. 32, no. 1, pp. 157–169, 1984.

[9] V. Tvergaard, "On localization in ductile materials containing spherical voids," *International Journal of Fracture*, vol. 18, no. 4, pp. 237–252, 1982.

[10] V. Tvergaard, "Effect of void cluster on ductile failure evolution," *Meccanica*, vol. 51, no. 12, pp. 3097–3105, 2016.

[11] Y. Zhu, M. D. Engelhardt, and R. Kiran, "Combined effects of triaxiality, Lode parameter and shear stress on void growth and coalescence," *Engineering Fracture Mechanics*, vol. 199, pp. 410–437, 2018.

[12] M. Dunand and D. Mohr, "Effect of Lode parameter on plastic flow localization after proportional loading at low stress triaxialities," *Journal of the Mechanics and Physics of Solids*, vol. 66, pp. 133–153, 2014.

[13] Y. Bai and T. Wierzbicki, "A new model of metal plasticity and fracture with pressure and lode dependence," *International Journal of Plasticity*, vol. 24, no. 6, pp. 1071–1096, 2008.

[14] S. Balaguru, V. Murali, and P. Chellapandi, "Effects of different operating temperatures on the tensile properties of the grid plate hardfaced with colmonoy in a pool type sodium fast reactor," *Science and Technology of Nuclear Installations*, vol. 2017, Article ID 5926105, 9 pages, 2017.

[15] S. Liu, C. J. Yuh, and X. K. Zhu, "Tensile-shear transition in mixed-mode I/II fracture," *Int J Solids Struct*, vol. 41, no. 22-23, pp. 6147–6172, 2004.

[16] H. Zhu and F. Qi, "Mechanical properties and fracture behaviors on 6061 aluminum alloy under shear stress state," *Rare Metals*, vol. 30, no. 5, pp. 550–554, 2011.

[17] S. M. Graham, T. Zhang, X. Gao, and M. Hayden, "Development of a combined tension-torsion experiment for calibration of ductile fracture models under conditions of low triaxiality," *International Journal of Mechanical Sciences*, vol. 54, no. 1, pp. 172–181, 2012.

[18] M. Giglio, A. Manes, and F. Viganò, "Ductile fracture locus of Ti-6Al-4V titanium alloy," *International Journal of Mechanical Sciences*, vol. 54, no. 1, pp. 121–135, 2012.

[19] A. M. Tang and J. Wang, "Test analysis of the fracture modes for some metal materials," *Journal of Experimental Mechanics*, vol. 18, no. 4, pp. 440–444, 2003, in Chinese.

[20] Y. Bao and T. Wierzbicki, "On fracture locus in the equivalent strain and stress triaxiality space," *International Journal of Mechanical Sciences*, vol. 46, no. 1, pp. 81–98, 2004.

[21] Y. B. Bao and R. Treitler, "Ductile crack formation on notched Al 2024-T351 bars under compression-tension loading," *Materials Science and Engineering: A*, vol. 384, no. 1-2, pp. 385–394, 2004.

[22] Y. Li, M. Luo, J. Gerlach, and T. Wierzbicki, "Prediction of shear-induced fracture in sheet metal forming," *Journal of Materials Processing Technology*, vol. 210, no. 14, pp. 1858–1869, 2010.

[23] Z. Li, J. Shi, and A. Tang, "Investigation on fracture mechanisms of metals under various stress states," *Acta Mechanica*, vol. 225, no. 7, pp. 1867–1881, 2014.

[24] T. M. Maccagno and J. F. Knott, "The mixed mode I/II fracture behaviour of lightly tempered HY130 steel at room temperature," *Engineering Fracture Mechanics*, vol. 41, no. 6, pp. 805–820, 1992.

[25] M. Mostafavi, D. J. Smith, and M. J. Pavier, "Fracture of aluminium alloy 2024 under biaxial and triaxial loading," *Engineering Fracture Mechanics*, vol. 78, no. 8, pp. 1705–1716, 2011.

[26] H. Zuo, Y. H. Chen, and C. Q. Zheng, "Mixed mode ductile fracture experiment and its controlling parameter," *Acta Mechanica Sinica*, vol. 31, no. 5, pp. 534–540, 1999, in Chinese.

[27] H. Zuo, *Mechanical mechanism and criterion of elastoplastic mixed mode FRACTURE*, Ph.D thesis, Northwestern Polytechnical University, 1999, Xi'an, China, in Chinese.

Hindawi
Science and Technology of Nuclear Installations
Volume 2019, Article ID 5769147, 12 pages
https://doi.org/10.1155/2019/5769147

Research Article

Study on Transmutation of Minor Actinides as Burnable Poison in VVER-1000 Fuel Assembly

Vinh Thanh Tran,[1] **Hoai-Nam Tran**,[2] **Huu Tiep Nguyen**,[1] **Van-Khanh Hoang**,[1] **and Pham Nhu Viet Ha**[1]

[1]*Institute for Nuclear Science and Technology, VINATOM, 179 Hoang Quoc Viet Str., Cau Giay Dist., Hanoi 100000, Vietnam*
[2]*Institute of Fundamental and Applied Sciences, Duy Tan University, Ho Chi Minh City 700000, Vietnam*

Correspondence should be addressed to Vinh Thanh Tran; tvthanh@vinatom.gov.vn and Pham Nhu Viet Ha; hapnv0915@gmail.com

Received 29 March 2019; Revised 8 August 2019; Accepted 21 August 2019; Published 3 November 2019

Guest Editor: Dimitrios Tsaoulidis

Thermal reactors have been considered as interim solution for transmutation of minor actinides recycled from spent nuclear fuel. Various studies have been performed in recent decades to realize this possibility. This paper presents the neutronic feasibility study on transmutation of minor actinides as burnable poison in the VVER-1000 LEU (low enriched uranium) fuel assembly. The VVER-1000 LEU fuel assembly was modeled using the SRAC code system, and the SRAC calculation model was verified against the MCNP6 calculations and the available published benchmark data. Two models of minor actinide loading in the LEU fuel assembly have been investigated: homogeneous mixing in the UGD (Uranium-Gadolinium) pins and coating a thin layer to the UGD pins. The consequent negative reactivity insertion by minor actinides was compensated by reducing the gadolinium content and boron concentration. The reactivity of the LEU assembly versus burnup and the transmutation of minor actinide nuclides were examined in comparison with the reference case. The results demonstrate that transmutation of minor actinides as burnable poison in the VVER-1000 reactor is feasible as minor actinides could partially replace the functions of gadolinium and boric acid for excess reactivity control.

1. Introduction

It is recognized that the negative fames of nuclear energy, i.e., the current nuclear power plants (NPPs) being operated worldwide for electricity generation, are the release of radioactive materials under normal, abnormal, or accident conditions and the by-products of highly radioactive, long-lived spent nuclear fuels. Hence, a closed nuclear fuel cycle has been considered as the best option to overcome the issues with disposal of used fuel to geologic repository. On average, a light water reactor (LWR) with electric capacity of 1000 MWe produces 20–30 metric tons of spent nuclear fuel annually, which consist of approximately 95 wt.% uranium, 1 wt.% plutonium, 4 wt.% fission products, and minor actinides (MAs) [1, 2]. In the used fuel, the trans-uranic elements, i.e., plutonium and MAs, dominate the decay heat load to the repository and cumulative long-term radiotoxicity to the environment. To lessen the burden for disposal and storage of spent nuclear fuel and to reduce its cumulative radiotoxicity to the environment, separation and transmutation of the plutonium and MAs in the used fuel are indispensable [3]. It has been realized that the transmutation of these actinides into either short-lived fission products or valued fissile or stable isotopes can be accomplished in fast reactors, subcritical reactors, or thermal reactors [1, 2, 4–8].

Fast reactors and subcritical reactors have been studied as the most potential candidates for transmutation of the actinides, thanks to their hard neutron spectra. However, these future technologies are still not mature nowadays and require at least several decades or even longer to be well proved and deployed on a large commercial scale. This

indicates that an interim solution to the used nuclear fuel, i.e., transmutation of the plutonium and MAs, is needed in near-term until the commercial deployment of fast reactors or subcritical reactors in future. LWRs, e.g., pressurized water reactors (PWRs), which are the most proven nuclear energy technologies, have been thus extensively studied as well for their transuranic transmutation capability with consideration to their numerous numbers currently being operated commercially in the world. Namely, once the actinide transmutation capability of LWRs is demonstrated, the current LWRs can be immediately deployed on a large scale to destroy the actinides for the sake of generating power and reducing the burden from disposal and storage of used fuel. In this regard, the MA transmutation in LWRs has drawn much attention so far to serve as a near-term solution to the issues with spent fuel and various methods of loading MAs into the LWRs have been investigated to realize such possibility. Nonetheless, most of the studies are reported with the Western PWRs [9–16]. Similar studies with the Russian water-water energy reactors (VVERs) have rarely been found in the literature although a large number of NPPs based on the VVER technologies are being operated in various East European and Asian countries [17, 18].

The VVER reactor is obviously a potential candidate for transmutation of actinides in the spent fuel stock-pile, and various methods of loading and burning transuranic elements in the Western PWRs may be adopted similarly to the Russian VVERs. In the past studies, transmuting MAs in the burnable poison rods [19, 20] or in some other locations in the PWR fuel assemblies has been found technically feasible and recommended as potential transmutation methods for LWRs, especially the unique advantage of loading MAs to partially replace the excess reactivity control functions of gadolinium and boric acid.

The present study therefore aims at investigating the neutronic feasibility of MA transmutation in a VVER-1000 low enriched uranium (LEU) fuel assembly [21]. The goal is to determine how efficient the MAs (neptunium, americium, and curium) recycled from spent fuel can be transmuted in the VVER-1000 fuel assembly. The MA loading into the VVER-1000 fuel assembly will be performed without significant modification of the assembly configuration, because any significant change of the fuel assembly design will lead to a penalty in the cost for fuel fabrication process and respective changes in reactor core design. The SRAC code system [22] is used for modeling the VVER-1000 LEU fuel assembly based on the ENDF/B-VII.0 library. The calculation model with SRAC is verified against the Monte Carlo calculations with the MCNP6 code [23] and the available published benchmark results. In recent publications, the burnable absorber rods have been suggested as potential locations for loading and burning MAs [18–20] and therefore two approaches are examined in this study: (a) MAs are mixed homogeneously in the UGD (Uranium-Gadolinium) pellets and (b) a coating layer of MAs is included to the UGD pellets. The constraint for these MA loadings is to ensure insignificant change in the reactivity of the fuel assembly while providing considerable MA transmutation rate.

The paper is organized as follows. The analysis model and methods of loading MAs into the VVER-1000 LEU fuel assembly are given in Section 2. The verification of the SRAC model for the VVER-1000 LEU fuel assembly is presented in Section 3. The results and feasibility of burning MAs in the VVER-1000 LEU fuel assembly are shown and discussed in Section 4. Lastly, concluding remarks and further works are represented in Section 5.

2. Calculation Methodology

The VVER-1000 LEU fuel assembly specified in the OECD VVER-1000 LEU and MOX (mixed oxide) Assembly Computational Benchmark [21] is utilized in the present investigation to examine the feasibility of MA transmutation as burnable poison in the VVER-1000 reactor. The configuration and main design parameters of the VVER-1000 LEU fuel assembly are shown in Figure 1 and Table 1, respectively. It is recalled that the benchmark model is designed to verify the computational codes for VVER-1000 LEU and MOX fuel calculations in support for the weapon grade plutonium disposition mission. It consists of two different hexagonal fuel assemblies: a uniform LEU fuel assembly and a profiled MOX fuel assembly. The LEU assembly consists of 300 fuel pin cells with 3.7 wt.% ^{235}U, 12 UGD pin cells with 3.6 wt.% ^{235}U, and 4 wt.% Gd_2O_3, 18 water filled guide tubes for control insertion, and one central water filled instrumentation tube. The MOX assembly consists of 138 fuel pin cells with 4.2 wt.% fissile Pu in the central region, surrounded by 96 fuel pin cells with 3 wt.% fissile Pu and 66 fuel pin cells with 2 wt.% fissile Pu at the outermost region, 12 UGD pin cells with 3.6 wt.% ^{235}U and 4 wt.% Gd_2O_3, 18 water filled guide tubes, and one central water filled instrumentation tube. These two assemblies are representative of the advanced designs under active R&D in Russia for VVER-1000 reactors and similar to the designs that are expected to be used in the plutonium disposition mission. In these assembly designs, the burnable absorber Gd_2O_3 is mixed with UO_2 to form the UGD pin cells for excess reactivity control at the beginning of cycle.

The VVER-1000 LEU fuel assembly is modeled in this work using the SRAC code system. In the SRAC simulation, the one-sixth of the LEU fuel assembly is modeled with the PIJ module (see Figure 2), the fuel burnup calculations are performed with the BURN-UP module, and the 107 energy groups based on the ENDF/B-VII.0 nuclear data library are used. The LEU fuel assembly modeled with SRAC is verified against the Monte Carlo code MCNP6 calculations and the published benchmark data for the S1 state, i.e., the normal operating poisoned state with ^{135}Xe and ^{149}Sm equilibrium concentrations. The parameters to be compared include the infinite multiplication factor (k-inf) of the fuel assembly versus burnup and nuclide concentrations.

According to [24], a combination of VVER-1000 and fast reactors was recommended for transmuting actinides recycled from spent fuel. The VVER-1000 reactor can be used for burning the plutonium in the form of MOX fuel. The fast reactor can be used for burning the MAs recycled from spent fuels of the VVER-1000 and fast reactors and the

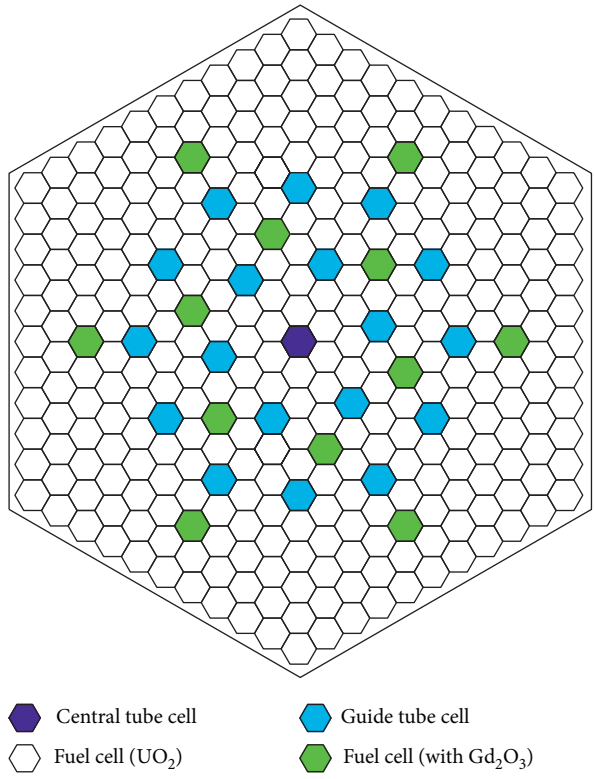

Figure 1: Configuration of the VVER-1000 LEU fuel assembly.

Table 1: Main design parameters of the VVER-1000 LEU fuel assembly.

Parameter	Value
Number of UO_2 fuel cells	300
Number of fuel cells with Gd	12
Number of guide tubes	18
Number of central tubes	1
Fuel cell inner radius (cm)	0.3860
Fuel cell outer radius (cm)	0.4582
Central tube cell inner radius (cm)	0.5450
Central tube cell outer radius (cm)	0.6323
Pin pitch (cm)	1.2750
Fuel assembly pitch (cm)	23.6
Fuel temperature (K)	1027.0
Nonfuel temperature (K)	575.0
^{235}U enrichment (wt.%)	3.7
Gd_2O_3 density (g/cm^3)	7.4

plutonium recycled from the spent fuel of the fast reactor. Another study showed the possibility of actinide transmutation in the VVER-440 reactor by loading the non-uranium pins consisting of actinides recycled from spent fuel to the periphery of the VVER-440 fuel assemblies [17]. The replacement of UGD pins in the VVER-1000 reactor by target elements containing a mixture of graphite and transmuted actinides has been also studied for the transmutation of americium and curium, and it was reported that the VVER-1000 reactor can operate in the self-service mode, i.e., the mode of transmutation when the number of transmuted nuclides is equal to the amount of their buildup in the fuel of the reactor itself [18]. It indicates that the VVER reactors can be used not only for the weapon grade plutonium disposition mission but also for the burning of actinides recycled from used fuel. Thus, the MA transmutation capability of VVER reactors should be carefully examined.

In this investigation, we intend to load the MAs in the UGD pins of the VVER-1000 LEU fuel assembly for their transmutation without significant change in the fuel assembly configuration. The purpose is to investigate the transmutation capability of the VVER-1000 LEU fuel assembly. To this end, we consider two approaches to load the MAs into the fuel assembly while tuning the gadolinium content and boron concentration: (1) mixing MAs homogeneously with UO_2 and Gd_2O_3 in the UGD pellets and (2) coating a thin layer of MAs around the UGD pellets. The rationale is that MAs can partially act as burnable poison and thus can partially replace the functions of the gadolinium and boric acid to control excess reactivity of the fuel assembly [19, 20].

It is recalled that the greatest industrial experience exists for UO_2 fuels for LWRs without any special shielding consideration in the fabrication process. Additionally, MOX fuels, which are fabricated in glove boxes with steel or lead shielding, have been mastered at the industrial level, especially with highly automated plants operating in France and the UK [1, 2]. However, the fabrication of MA bearing fuels with high gamma and neutron doses from MAs requires extra biological protection in the form of lead (for gamma radiation) and a combination of water, lead, and cadmium or boron (for neutron radiation). Also, adequate shielding should be provided during the transport and handling of fresh MA containing fuels [2]. These challenges for fabrication, transport, and handling of MA fuels must be overcome in a dedicated MA fuel development program. The present work focuses mainly on the neutronic feasibility of MA transmutation as burnable poison in the VVER-1000 fuel assembly.

For the purpose of this study, the MA vector consisting of neptunium, americium, and curium from spent fuel of the VVER-440 [5] is adopted and given in Table 2. The parameters to be investigated are the k-inf of the fuel assembly versus burnup and the transmutation rates of MAs in the VVER-1000 LEU fuel assembly. The results are expected to reveal the MA transmutation possibility in the VVER-1000 LEU fuel assembly and the capability of MAs to substitute partially the gadolinium and boric acid in the VVER-1000 reactor.

3. Verification of the SRAC Model for the VVER-1000 LEU Fuel Assembly

The SRAC calculation model of the VVER-1000 LEU fuel assembly was verified against the MCNP6 calculations and the benchmark mean (BM) values [21]. The Monte Carlo calculations with the MCNP6 code using a modern nuclear data library were performed herein to support the verification of the SRAC deterministic model. In the SRAC calculations, the ENDF/B-VII.0 library that is the latest one

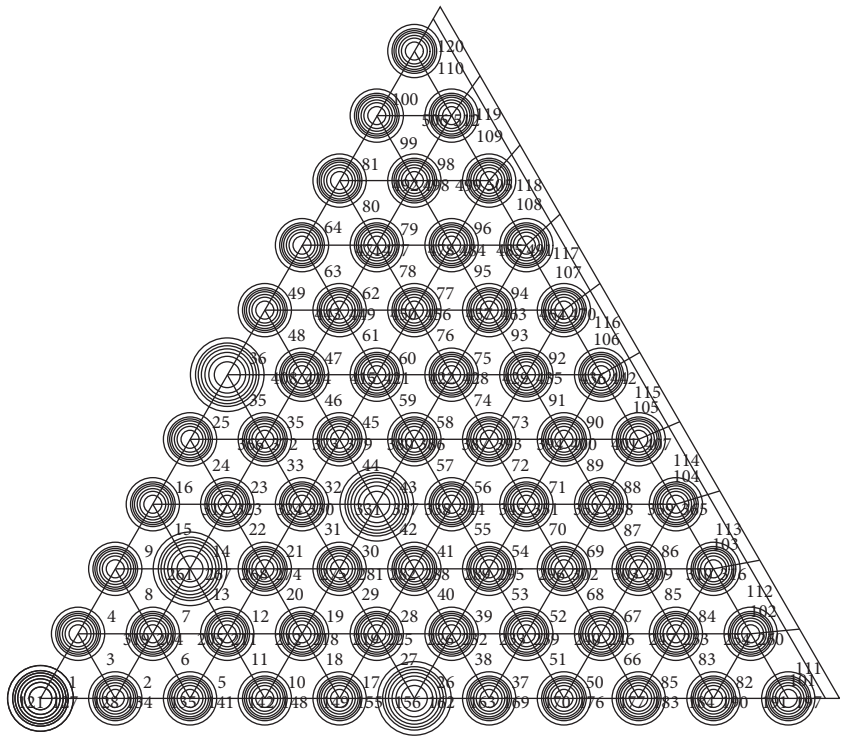

Figure 2: One-sixth model of the VVER-1000 LEU fuel assembly with SRAC.

Table 2: MA vector of VVER-440 spent fuel.

MA vector									
Isotope	^{237}Np	^{241}Am	^{242m}Am	^{243}Am	^{242}Cm	^{243}Cm	^{244}Cm	^{245}Cm	^{246}Cm
Fraction (at.%)	48.89	31.56	0.11	14.65	0.001	0.049	4.43	0.26	0.05

integrated with the SRAC code system was used whereas the ENDF/B-VII.1 library was utilized in the MCNP6 simulation. The burnup calculation for the VVER-1000 LEU fuel assembly was then performed with SRAC and MCNP6 under the operating poisoned condition (the S1 state) [21]. Under this condition, the fuel temperature is 1027 K and the moderator temperature is 575 K with equilibrium ^{135}Xe and ^{149}Sm concentrations and a power density of 108 MWt/m^3 up to a burnup of 40 MWd/kgHM. In both the SRAC and MCNP6 calculations, the UGD pins have been radially divided into five rings as required in the benchmark document [21] to account for the shielding effect due to the gadolinium isotopes and allow the calculation of nuclide concentrations as a function of the radial position in the UGD pins.

In the MCNP6 simulation, the statistical error of ~30 pcm was obtained as the neutron history of 5×10^6 for parallel depletion calculation was selected. Burnup calculations were performed with 160 steps of 0.25 MWd/kgHM. MCNP6 includes the new depletion capability linking steady state flux calculations in MCNP6 and nuclide depletion calculations in CINDER90 [23]. A steady state flux calculation is run to determine the system eigenvalue, group fluxes, energy integrated reaction rates, fission multiplicity, and recoverable energy per fission. CINDER90 then uses these values generated by MCNP6 to perform depletion calculation for number densities of the next burnup step. MCNP6 takes the new number densities generated by CINDER90 for the next steady state flux calculation. This linked process is repeated until the end of the final burnup step. However, the default nuclear data in MCNP6 are given at certain temperatures for heavy isotopes (293.6, 600, 900, 1200, and 2500 K) while the fuel temperature of 1027 K is needed in this calculation. There are various methods to cope with such kind of temperature dependence [25]. One of the suitable methods for MCNP6 is the on-the-fly (OTF) methodology for fitting of Doppler broadened cross sections and this method was applied in the present study. The OTF data for heavy isotopes in the VVER-1000 LEU fuel assembly that correspond to the temperature range of 293.6 to 1200 K were created from the ENDF/B-VII.1 library at the temperature of 293.6 K.

The PIJ module with its cell burnup routine of the SRAC code system [22] was utilized for the burnup calculation of the VVER-1000 LEU benchmark assembly. The PIJ module that is based on the collision probability method was used for lattice cell calculations. The cell burnup routine used one-group collapsed flux distribution and the collapsed microscopic cross sections to solve the depletion equation using Bateman's method. The burnup calculation using the cell burnup routine of the PIJ module was performed with 40 steps of 0.25 MWd/kgHM followed by 5 steps of 1.0 MWd/kgHM and 10 steps of 2.5 MWd/kgHM. The 107 neutron

energy groups based on the ENDF/B-VII.0 library were collapsed to four groups for use in the SRAC calculations.

The results for the k-inf as a function of burnup for the S1 state, i.e., the operating poisoned state, are shown in Figure 3. It can be seen that the k-inf calculated using SRAC agreed well with that calculated with MCNP6 and the BM value. Comparing with the BM values, the maximum differences of k-inf obtained from SRAC and MCNP6 calculations are 352 and 413 pcm, respectively, whereas those for other computational codes used in the benchmark such as MCU, TVS-M, WIMS8A, HELIOS, and MULTICELL are 440, 400, 460, 260, and 360 pcm, respectively [21]. The reactivity curve of the fuel assembly is relatively flat in the early burnup stage due to the use of Gd_2O_3 in the UGD pins for excess reactivity control. As the gadolinium isotopes burn out, the reactivity decreases with burnup in a nearly linear manner due to the effect of fissile material depletion and neutron absorber accumulation. It can also be seen that the effect of gadolinium depletion on the reactivity curve was well simulated by SRAC and MCNP6. The differences in the results obtained from SRAC and MCNP6 are attributed to the different transport and depletion calculation methods, the different nuclear data libraries used in SRAC and MCNP6, and the models using the two codes.

In addition, it was also confirmed that the nuclide concentrations for Cell 1 (UO_2 pin) and Cell 24 (UGD pin) as specified in the benchmark problem [21] as well as the radial nuclide concentrations for five rings of Cell 24 (UGD pin) calculated with SRAC and MCNP6 generally compare well with the BM values. Therefore, it is demonstrated that the SRAC calculation model for the VVER-1000 LEU fuel assembly developed in this study is reliable and it will be used for the investigation of MA transmutation possibility in the VVER-1000 LEU fuel assembly.

4. MA Transmutation in VVER-1000 LEU Fuel Assembly

4.1. Homogeneous Mixing of MAs in the UGD Pins. As the MAs are homogeneously mixed in the UGD pins of the VVER-1000 LEU fuel assembly, the gadolinium content and boron concentration were adjusted with varying content of MAs in order to maintain the reactivity of the fuel assembly. It is because the MAs can act as burnable poison and thus can partially replace functions of the gadolinium in the UGD pins and boric acid in the coolant [19, 20]. In this calculation, the content of MAs was loaded from 6 wt.% to 10 wt.%; the content of the gadolinium was reduced from 4 wt.% in the reference case to 2 wt.%, 2.5 wt.%, and 3 wt.% and the boron concentration was reduced correspondingly to compensate the negative reactivity insertion by the MAs. Table 3 summarizes the cases investigated here.

Although in the current practice the MA content in MA bearing fuels should be limited to a few percent (up to 5 wt.%) for the homogeneous case [2], the relatively high MA content from 6 wt.% to 10 wt.% was selected in this investigation to allow high MA loading amount so as to demonstrate a considerable MA transmutation rate from neutronic viewpoint. As the VVER-1000 LEU fuel assembly used in this study has 12 UGD pins, its configuration can be redesigned to accommodate more UGD pins (up to 36 pins) [26, 27]. With a larger number of the UGD pins, equivalent or even higher MA loading amount in the UGD pins as compared with this study can be easily obtained with the MA content not higher than 5 wt.%.

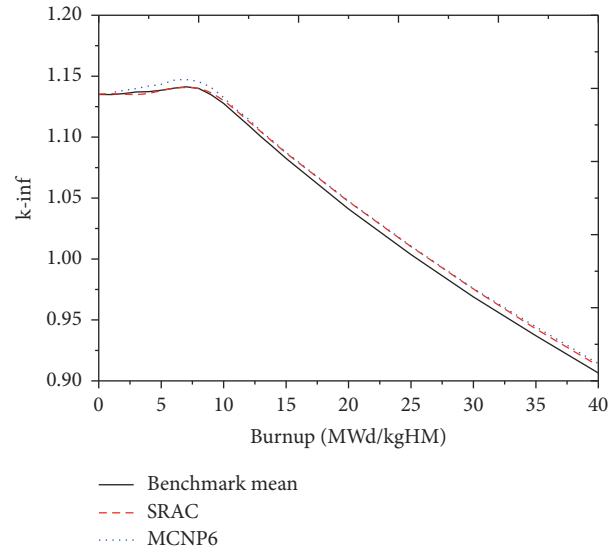

Figure 3: Infinite multiplication factor (k-inf) of the VVER-1000 LEU fuel assembly versus burnup obtained with SRAC and MCNP6 calculations.

Table 3: MA content, gadolinium content, and boron concentration used in this investigation.

MA content, wt.%	Gadolinium content, wt.%; Boron concentration, ppm		
6	2; 550	2.5; 500	3; 450
8	2; 500	2.5; 450	3; 400
10	2; 450	2.5; 400	3; 350

As shown in Table 3, the gadolinium content was first reduced to 2 wt.% and the boron concentration was decreased from 600 ppm (reference case) to 550 ppm, 500 ppm, and 450 ppm with respect to the MA content of 6 wt.%, 8 wt.%, and 10 wt.%. The results of the k-inf of the VVER-1000 LEU fuel assembly versus burnup were displayed in Figures 4–6 for the cases when reducing the gadolinium content to 2 wt.% and loading the MA content of 6, 8, and 10 wt.%. It was found that the fuel cycle length when loading MAs from 6 to 10 wt.% and decreasing the gadolinium content to 2 wt.% was substantially reduced as compared to the reference case. As can be seen in Figures 4–6, the combined reduction of gadolinium content to 2 wt.% and respective boron concentration could lead to a cycle length comparable to the reference case. However, the excess reactivity in these cases was generally higher at the early burnup steps and became smaller than the reference case after about 7 MWd/kgHM as gadolinium burned out.

The gadolinium content was therefore increased from 2 to 2.5 wt.% to expect a decrease of the aforementioned high

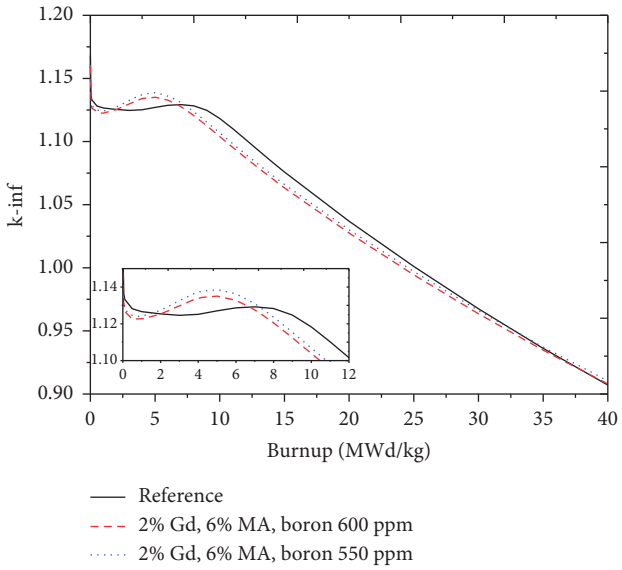

Figure 4: The k-inf versus burnup when loading 6 wt.% of MAs and reducing GD to 2 wt.%.

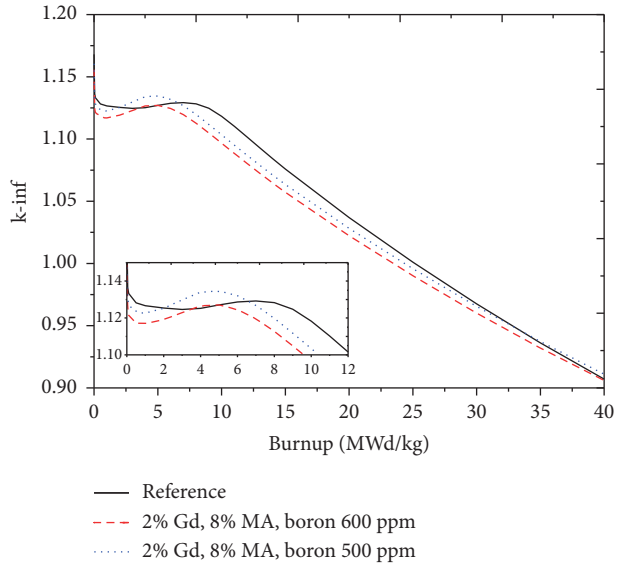

Figure 5: The k-inf versus burnup when loading 8 wt.% of MAs and reducing GD to 2 wt.%.

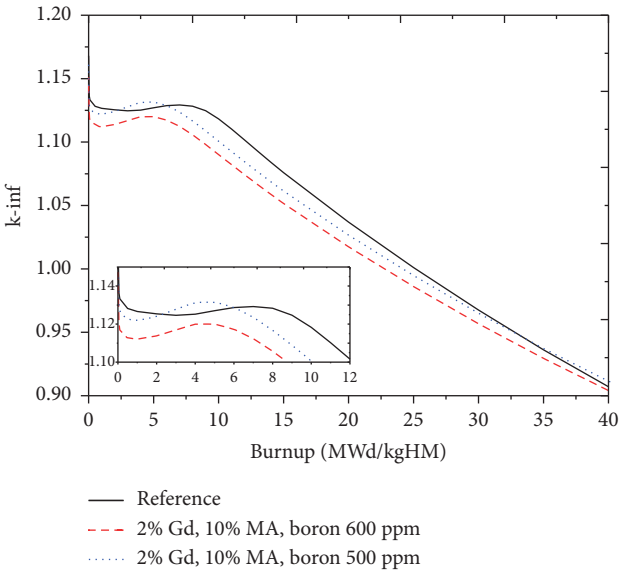

Figure 6: The k-inf versus burnup when loading 10 wt.% of MAs and reducing GD to 2 wt.%.

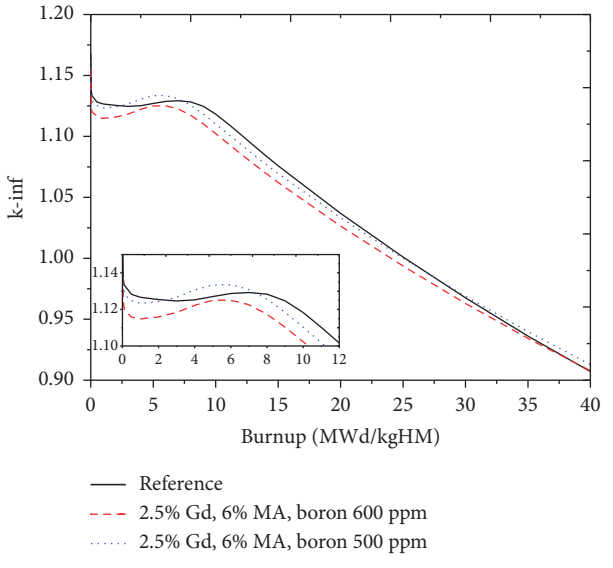

Figure 7: The k-inf versus burnup when loading 6 wt.% of MAs and reducing GD to 2.5 wt.%.

excess reactivity at the early burnup steps and the boron concentration was adjusted to 500 ppm, 450 ppm, and 400 ppm with respect to the MA content of 6 wt.%, 8 wt.%, and 10 wt.%. Figures 7–9 show that the behavior of the k-inf versus burnup in the case of reducing the gadolinium content to 2.5 wt.% was somewhat different from that with the gadolinium content of 2 wt.%. Namely, the excess reactivity in the cases of reducing only the gadolinium content to 2.5 wt.% was smaller, leading to smaller cycle lengths. To overcome this disadvantage, reducing the boron concentration to 500 ppm, 450 ppm, and 400 ppm with respect to the MA content of 6 wt.%, 8 wt.%, and 10 wt.% could lead to a comparable cycle length while still keeping the excess reactivity equivalent or even somewhat lower than the reference case as can be seen in Figures 7–9.

The gadolinium content was further increased from 2.5 to 3 wt.% and the boron concentration was adjusted to 450 ppm, 400 ppm, and 350 ppm with respect to the MAs content of 6 wt.%, 8 wt.%, and 10 wt.%. It was found that the behavior of the k-inf versus burnup in these cases (see Figures 10–12) is very similar to that with the gadolinium content of 2.5 wt.% as mentioned previously. Nonetheless, the cycle length when loading 6 wt.%, 8 wt.%, and 10 wt.% of MAs with the gadolinium content of 3 wt.% was further improved and became almost identical to the reference case as the boron concentration was reduced to 450 ppm,

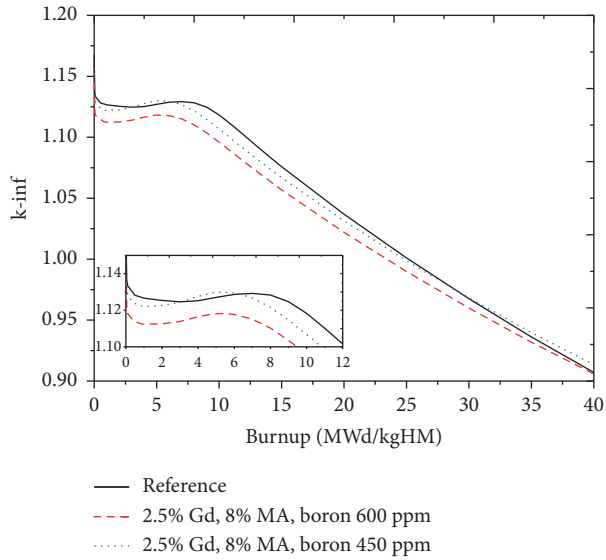

Figure 8: The k-inf versus burnup when loading 8 wt.% of MAs and reducing GD to 2.5 wt.%.

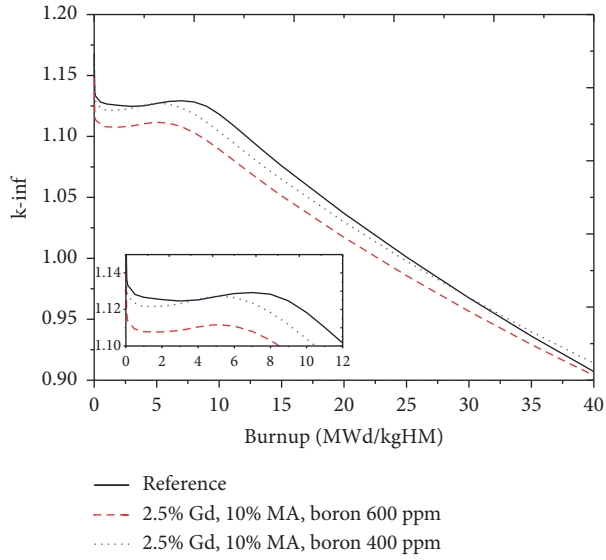

Figure 9: The k-inf versus burnup when loading 10 wt.% of MAs and reducing GD to 2.5 wt.%.

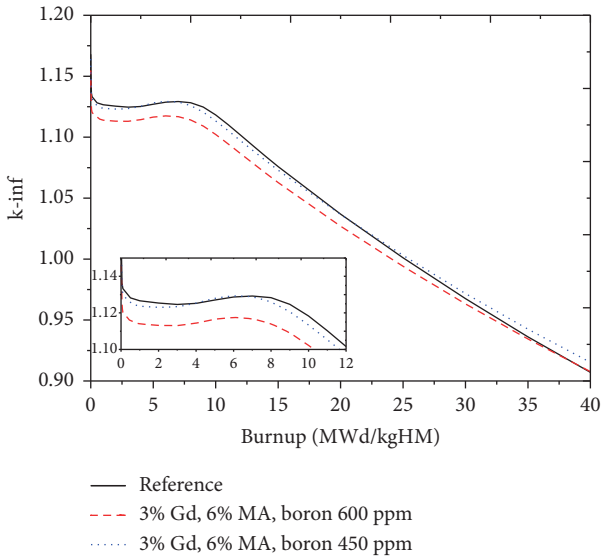

Figure 10: The k-inf versus burnup when loading 6 wt.% of MAs and reducing GD to 3 wt.%.

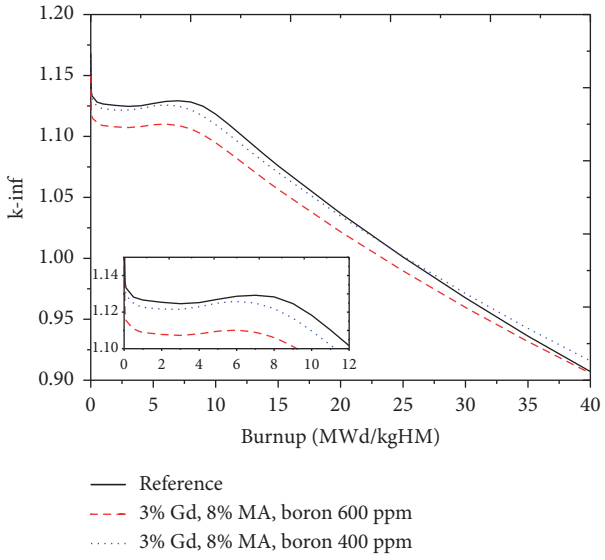

Figure 11: The k-inf versus burnup when loading 8 wt.% of MAs and reducing GD to 3 wt.%.

400 ppm, and 350 ppm, respectively, as shown in Figures 10–12. Moreover, the excess reactivity at the beginning of the cycle was also generally reduced in comparison to the reference case.

The results illustrated in Figures 4–12 also imply that the MAs with the content of up to 10 wt.% can be loaded into the VVER-1000 LEU fuel assembly without significantly affecting the fuel cycle length by means of reducing the gadolinium content and the boron concentration to offset the negative reactivity insertion by the MAs. For the MA loading from 8 to 10 wt.%, it was found that the lower excess reactivity and equivalent cycle length as compared to the reference case can be obtained with the gadolinium content being reduced to around 2.5–3.0 wt.% and the boron concentration being reduced to around 350–400 ppm. As a result, loading 10 wt.% of MAs into the UGD pins is recommended for the sake of excess reactivity control and high loading amount of MAs while keeping almost the same cycle length with the reference case.

The transmutation of the MA isotopes is shown in Figures 13–17 for the cases when loading 10 wt.% of MAs and adjusting the gadolinium content and boron concentration. As can be seen in these figures, the concentrations of ^{237}Np, ^{241}Am, and ^{243}Am decreased with fuel burnup while those of ^{244}Cm and ^{245}Cm accumulated with fuel burnup. Figures 13–17 also indicate that the transmutation of the MA

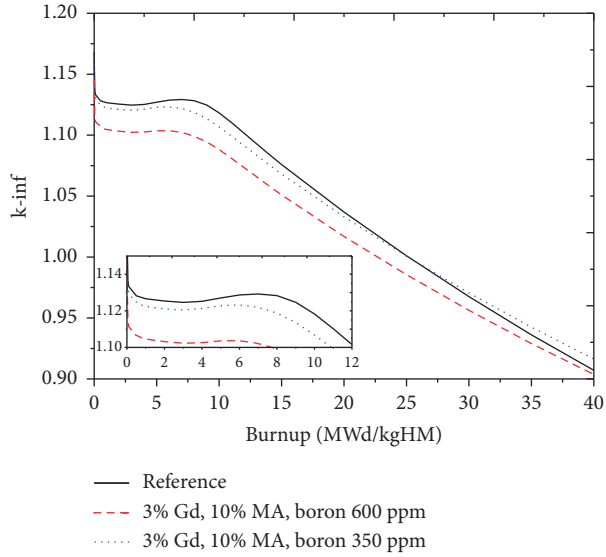

Figure 12: The k-inf versus burnup when loading 10 wt.% of MAs and reducing GD to 3 wt.%.

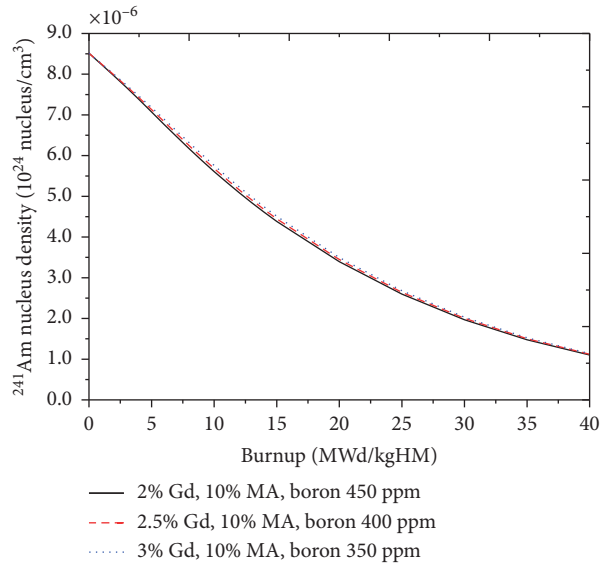

Figure 14: Transmutation of ^{241}Am versus burnup when loading 10 wt.% of MAs.

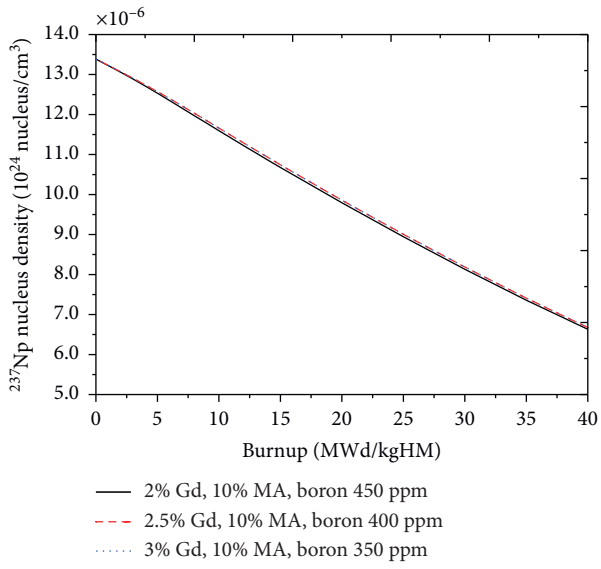

Figure 13: Transmutation of ^{237}Np versus burnup when loading 10 wt.% of MAs.

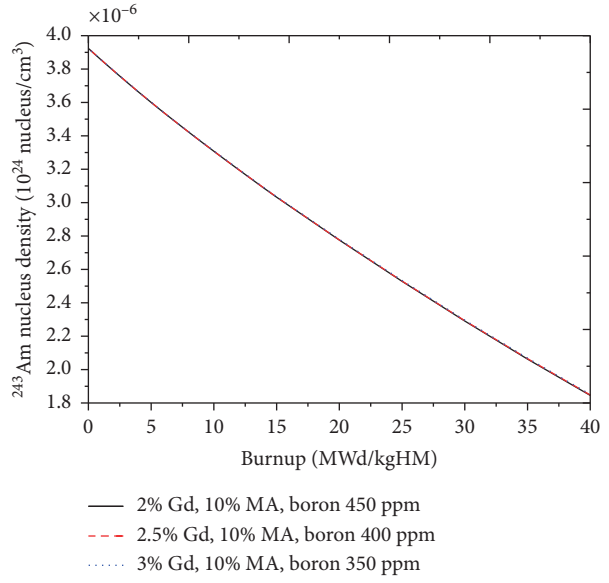

Figure 15: Transmutation of ^{243}Am versus burnup when loading 10 wt.% of MAs.

isotopes versus burnup slightly depends on the adjustments of the gadolinium content and boron concentration. After 306 days, the ^{237}Np concentration reduced to ~15.63%, the ^{241}Am concentration reduced to ~38.58%, and the ^{243}Am concentration reduced to ~18.48%, whereas those of ^{244}Cm and ^{245}Cm increased to ~51.60% and ~103.13% as illustrated in Table 4 when loading 10 wt.% of MAs and reducing the gadolinium content to 3 wt.% and boron concentration to 350 ppm. Hence, ^{237}Np, ^{241}Am, and ^{243}Am can be significantly transmuted with a transmutation rate as high as 38.58% for ^{241}Am. Nevertheless it is noticed that ^{244}Cm and ^{245}Cm accumulate with high rates though their concentrations are relatively small. This issue was also reported in recent publications for thermal reactors [2, 20]. It is recalled that the radiotoxicity of MAs in spent fuel from power reactors is mainly contributed by ^{241}Am (half-life of 432.2 years) and ^{244}Cm (half-life of 18.1 years). If actinides from PWR-type reactors over 100 years of storage are considered, the radiotoxicity of ^{241}Am contributes more than 90% of the total radiotoxicity while the contribution from other actinides is less than 10% [18]. Hence, transmutation of ^{241}Am could contribute to a significant reduction of the radiotoxicity level of the long-lived radioactive waste.

The results demonstrate that the transmutation of MAs recycled from spent nuclear fuel in the VVER-1000 fuel assembly is feasible from neutronic viewpoint and the

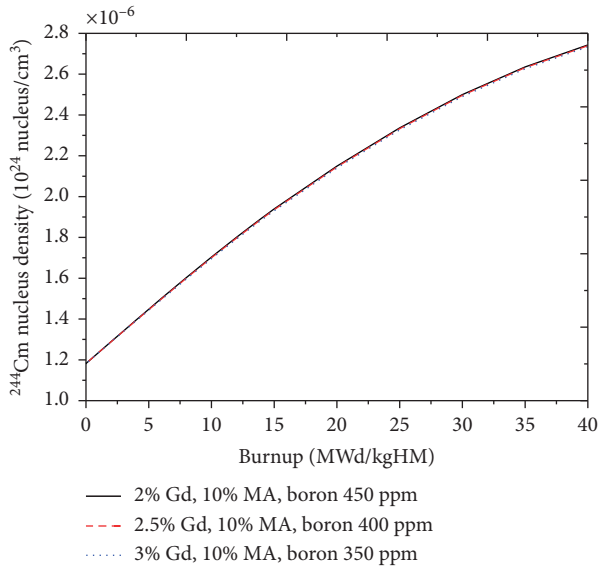

Figure 16: Transmutation of ^{244}Cm versus burnup when loading 10 wt.% of MAs.

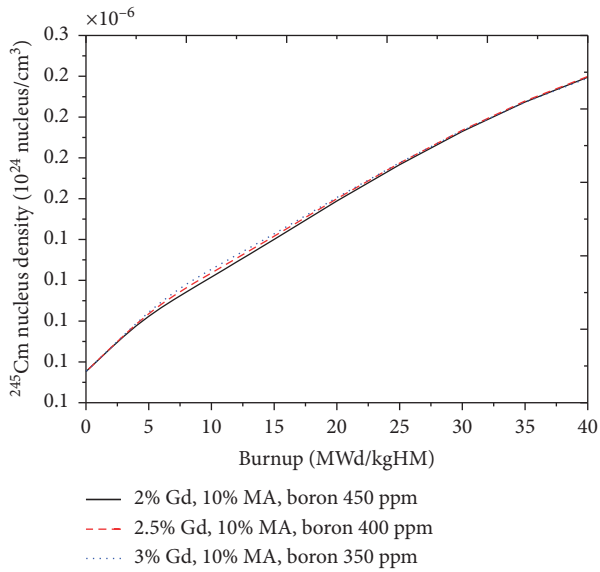

Figure 17: Transmutation of ^{245}Cm versus burnup when loading 10 wt.% of MAs.

total transmutation rate of ~20% can be achieved. Also, the role of MAs as burnable absorbers in partial replacement to the gadolinium and boric acid in the VVER-1000 reactor was confirmed and in line with recent publications for PWRs [19, 20]. It is worth noting that the reduction of the boron concentration not only could help attain a more negative moderator temperature coefficient during the core lifetime but also could allow minimizing the operation of a complicated chemical control system as well as reducing the corrosion of structural materials [26]. Furthermore, the reduced gadolinium content could help improve the thermal conductivity and melting point of the UGD pins [28].

Table 4: Transmutation rate in case of homogeneous loading with 10 wt.% of MAs.

Isotope	Initial amount (g)	Residual amount at 306 days (g)	Mass reduced after 306 days (g)	Disappearance rate after 306 days (%)
^{237}Np	896.78	756.59	140.19	15.63
^{241}Am	580.05	356.29	223.76	38.58
^{243}Am	269.52	219.72	49.80	18.48
^{244}Cm	81.54	123.62	−42.08	−51.60
^{245}Cm	4.79	9.73	−4.94	−103.13
Total	1832.67	1465.94	366.73	20.01

4.2. Coating a Thin Layer of MAs to the UGD Pins. In addition to homogeneous mixing of MAs in the UGD pins as above, the heterogeneous loading of MAs in the UGD pins of the VVER-1000 LEU fuel assembly was also considered herein. The MAs were coated as a thin layer at the outside of the UGD pellets as shown in Figure 18. The thickness of the cladding was kept untouched and the outer radius of the UGD region was reduced to accommodate the layer of MAs. For the purpose of MA burning, the MA content of 10 wt.% was selected in this investigation. The MA-coated layer (see Figure 18) equivalent to homogeneous loading with 10 wt.% of MAs is 0.01981 cm thick. Similar to the case of homogeneous mixing, the gadolinium content and boron concentration were also reduced to compensate the negative reactivity insertion by the MAs.

The results of the k-inf of the VVER-1000 LEU assembly versus burnup when coating MAs to the UGD pins and reducing the gadolinium content and boron concentration are shown in Figures 19–21 in relation to the reference case. It can be seen that the cases of reducing only the gadolinium content led to a significantly lower excess reactivity at the beginning of the cycle and a considerably shorter cycle length. This behavior of the k-inf versus burnup is very similar to that shown in Figures 6, 9, and 12 for the cases of homogeneous loading. Hence, the boron concentration was again reduced to 450 ppm, 400 ppm, and 350 ppm with respect to the gadolinium content of 2 wt.%, 2.5 wt.%, and 3 wt.%. Figures 19–21 show that the excess reactivity at the early burnup steps when reducing both the gadolinium content and boron concentration was smaller than or comparable to the reference case. Nevertheless, the cycle length when reducing the boron concentration to 350 ppm became identical to the reference case, while that with the boron concentration of 400 ppm and 450 ppm was somewhat shorter. Consequently, reducing the gadolinium content to 3 wt.% and boron concentration to 350 ppm is recommended when coating with 10 wt.% of MAs to the UGD pellets.

The transmutation of the MA isotopes when coating with 10 wt.% of MAs and reducing the gadolinium content to 3 wt.% and boron concentration to 350 ppm is given in Table 5. Comparing the results shown in Tables 4 and 5 shows that the difference in the transmutation rate of the MA isotopes between homogeneous and heterogeneous loadings was relatively small. However, the transmutation mass in the case of heterogeneous loading was ~6.8% higher

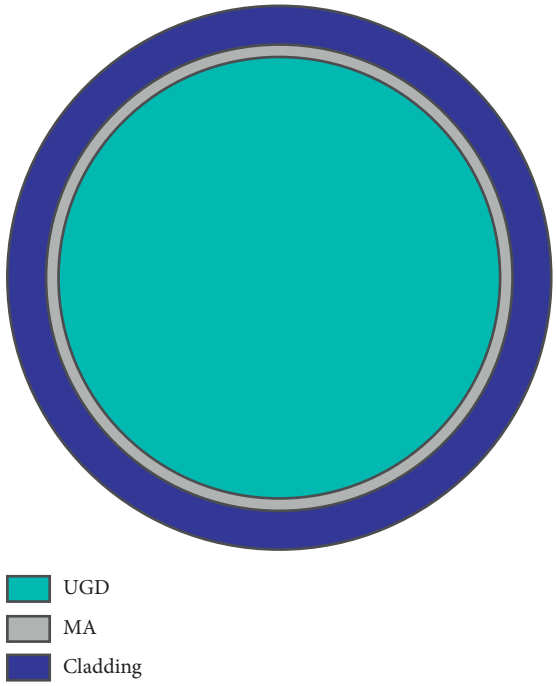

Figure 18: Coating a thin layer of MAs to the UGD pellet.

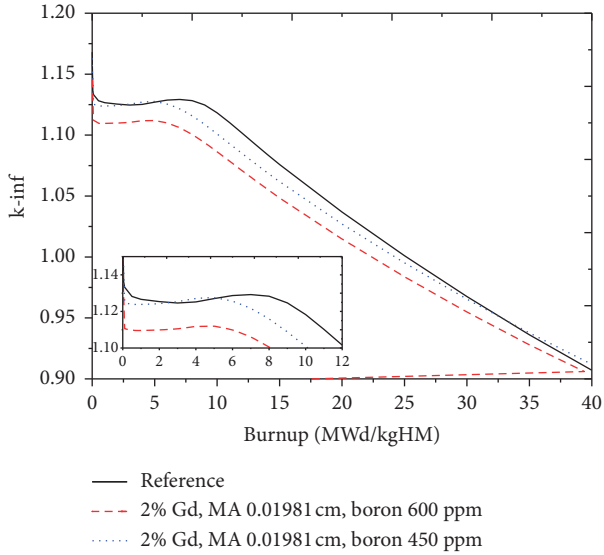

Figure 19: The k-inf versus burnup when coating a thin layer of MAs to the UGD pins and reducing GD to 2 wt.%.

than that of homogeneous loading. It is because the spatial self-shielding effect due to the heterogeneous loading of MAs will affect the burnup of the fuel and the transmutation of MAs [20]. For the case of heterogeneous loading in this study, the core neutrons reach the MA layer firstly and the MA layer is thin enough, leading to such increase in the transmutation of MAs as compared to the case of homogeneous mixing. Furthermore, the spatial self-shielding effect also affected the depletion of ^{155}Gd and ^{157}Gd as illustrated in Figures 22 and 23, which show that the

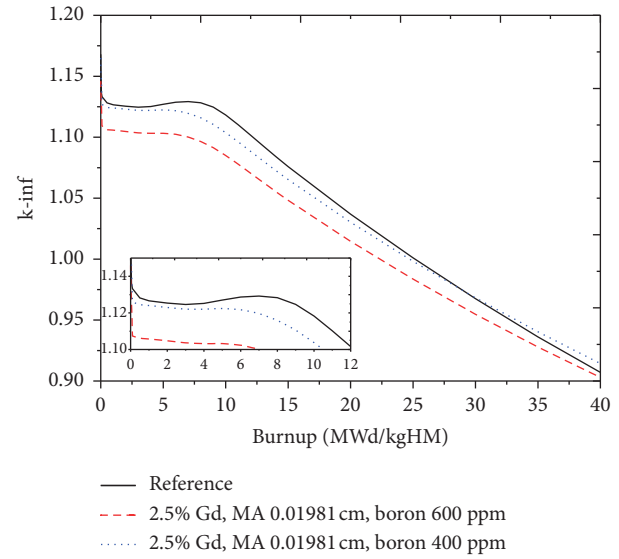

Figure 20: The k-inf versus burnup when coating a thin layer of MAs to the UGD pins and reducing GD to 2.5 wt.%.

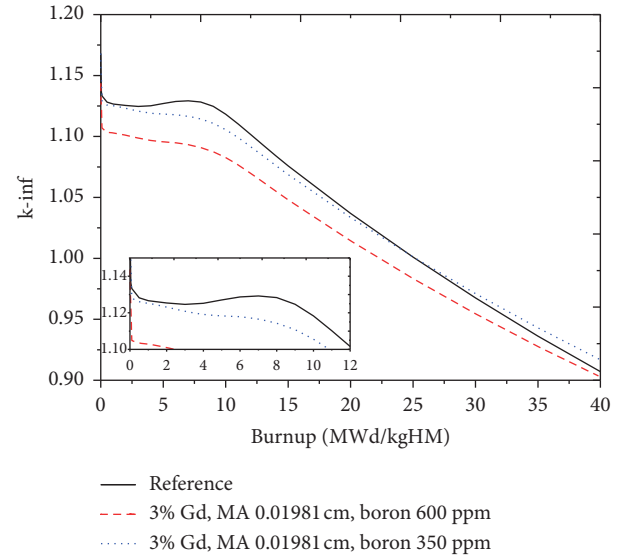

Figure 21: The k-inf versus burnup when coating a thin layer of MAs to the UGD pins and reducing GD to 3.0 wt.%.

Table 5: Transmutation rate in case of heterogeneous loading with 10 wt.% of MAs.

Isotope	Initial amount (g)	Residual amount after 306 days (g)	Mass reduced after 306 days (g)	Disappearance rate after 306 days (%)
^{237}Np	896.78	746.44	150.34	16.76
^{241}Am	580.05	341.73	238.32	41.09
^{243}Am	269.52	218.40	51.12	18.97
^{244}Cm	81.54	122.82	−41.28	−50.63
^{245}Cm	4.79	11.60	−6.81	−142.17
Total	1832.67	1440.98	391.69	21.37

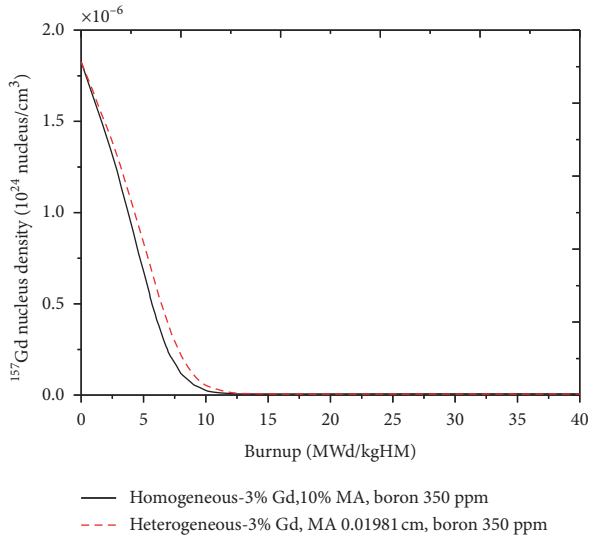

Figure 22: Comparison of the depletion of ^{155}Gd for two MA loading models.

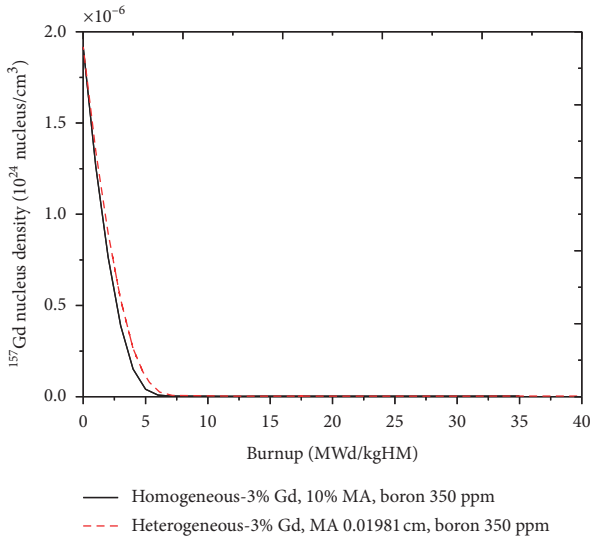

Figure 23: Comparison of the depletion of ^{157}Gd for two MA loading models.

gadolinium isotopes depleted somewhat slower in the case of heterogeneous loading.

5. Conclusions

The possibility of MA transmutation as burnable poison in the VVER-1000 LEU fuel assembly was examined using the SRAC code system. The SRAC calculation model for the VVER-1000 LEU fuel assembly was verified against the MCNP6 calculations and the available published benchmark results. Two models of MA loading were considered: homogeneous mixture in the UGD pellet and heterogeneous coated layer around the UGD pellet. The gadolinium content and the boron concentration were reduced correspondingly to compensate the negative reactivity insertion by MA loading.

It was found that the MAs can be loaded up to 10 wt.% into the UGD pins and the combined reduction in the gadolinium content and boron concentration could help facilitate the excess reactivity control at the beginning of the fuel cycle without significant effect on the cycle length. As in the current practice the MA content in MA bearing fuels should be limited to a few percent (up to 5 wt.%) for the homogeneous case [2], the limitations regarding the relatively high MA content from 6 wt.% to 10 wt.% can be possibly overcome by increasing the number of the UGD pins (up to 36 pins) in the VVER-1000 fuel assembly [26, 27]. Increasing the number of the UGD pins could reduce the MA content in the UGD pins less than 5 wt.% while allowing a high total MA loading amount in the whole assembly and thus avoid serious shielding issues in the fabrication, transport, and handling of MA bearing fuels.

For both cases of homogeneous and heterogeneous loadings, the total transmutation rate of ~20% could be obtained. However, the comparison between the two cases shows that the transmutation mass could be increased by ~6.8% for the case of coating a thin layer of MA to the UGD pins. The results show that ^{237}Np, ^{241}Am, and ^{243}Am can be significantly transmuted with a transmutation rate as high as ~40% for ^{241}Am. This advantage is somewhat offset by the unfavorable accumulation of ^{244}Cm and ^{245}Cm at high rates with fuel burnup. However, if actinides from PWR-type reactors over 100 years of storage are considered, more than 90% of the total radiotoxicity is contributed by ^{241}Am [18]. Therefore, transmuting ^{241}Am could lead to a significant decrease of the total long-term radiotoxicity of MAs.

Consequently, it is highly recommended that transmutation of MAs as burnable poison in the VVER-1000 reactor is feasible taking into account the fact that the excess reactivity control and the inherent safety characteristics of the VVER-1000 reactor can be further improved as MAs can partially replace the gadolinium and boric acid. Further investigation on transmutation of MAs at a full core level and MOX core of the VVER-1000 reactor when coating a thin layer of MA to the UGD pins is being planned.

Data Availability

Data will be available upon request.

Conflicts of Interest

The authors declare that they have no conflicts of interest.

Acknowledgments

This research was funded by the Ministry of Science and Technology of Vietnam under Grant no. DTCB.04/17/VKHKTHN.

References

[1] International Atomic Energy Agency, "Status of minor actinide fuel development," IAEA Nuclear Energy Series, Vienna, Austria, 2009.

[2] OECD/NEA, *Minor Actinide Burning in Thermal Reactors*, Nuclear Energy Agency, Paris, France, 2013.

[3] R. Jubin, "Spent fuel reprocessing, introduction to nuclear chemistry and fuel cycle separations course, consortium for risk evaluation with stakeholder participation," 2008, http://www.cresp.org/education/courses/shortcourse/.

[4] C. H. M. Broeders, E. Kiefhaber, and H. W. Wiese, "Burning transuranium isotopes in thermal and fast reactors," *Nuclear Engineering and Design*, vol. 202, no. 2-3, pp. 157–172, 2000.

[5] Z. Perkó, J. L. Kloosterman, and S. Fehér, "Minor actinide transmutation in GFR600," *Nuclear Technology*, vol. 177, no. 1, pp. 83–97, 2012.

[6] T. Kooyman, L. Buiron, and G. Rimpault, "A comparison of curium, neptunium and americium transmutation feasibility," *Annals of Nuclear Energy*, vol. 112, pp. 748–758, 2018.

[7] H. N. Tran and Y. Kato, "New^{237}Np burning strategy in a supercritical CO_2-cooled fast reactor core attaining zero burnup reactivity loss," *Nuclear Science and Engineering*, vol. 159, no. 1, pp. 83–93, 2008.

[8] H. N. Tran, Y. Kato, P. H. Liem, V. K. Hoang, and S. M. T. Hoang, "Minor actinide transmutation in supercritical-CO_2-cooled and sodium-cooled fast reactors with low burnup reactivity swings," *Nuclear Technology*, vol. 205, no. 11, pp. 1460–1473, 2019.

[9] N. Takaki, "Neutronic potential of water cooled reactor with actinide closed fuel cycle," *Progress in Nuclear Energy*, vol. 37, no. 1–4, pp. 223–228, 2000.

[10] E. Shwageraus, P. Hejzlar, and M. S. Kazimi, "A combined nonfertile and UO_2 PWR fuel assembly for actinide waste minimization," *Nuclear Technology*, vol. 149, no. 3, pp. 281–303, 2005.

[11] T. A. Taiwo, T. K. Kim, J. A. Stillman, R. N. Hill, M. Salvatores, and P. J. Finck, "Assessment of a heterogeneous PWR assembly for plutonium and minor actinide recycle," *Nuclear Technology*, vol. 155, no. 1, pp. 34–54, 2006.

[12] D. Tincher and T. W. Knight, "Feasibility study of minor actinide transmutation in light water reactors with various Am/Cm separation efficiencies," *Nuclear Engineering and Design*, vol. 241, no. 12, pp. 5295–5307, 2011.

[13] M. A. Pope, R. S. Sen, A. M. Ougouag, G. Youinou, and B. Boer, "Neutronic analysis of the burning of transuranics in fully ceramic micro-encapsulated tri-isotropic particle-fuel in a PWR," *Nuclear Engineering and Design*, vol. 252, pp. 215–225, 2012.

[14] B. Liu, K. Wang, J. Tu, F. Liu, L. Huang, and W. Hu, "Transmutation of minor actinides in the pressurized water reactors," *Annals of Nuclear Energy*, vol. 64, pp. 86–92, 2014.

[15] A.-A. Zakari-Issoufou, X. Doligez, A. Somaini et al., "Americium mono-recycling in PWR: a step towards transmutation," *Annals of Nuclear Energy*, vol. 102, pp. 220–230, 2017.

[16] B. Liu, R. Jia, R. Han, X. Lyu, J. Han, and W. Li, "Minor actinide transmutation characteristics in AP1000," *Annals of Nuclear Energy*, vol. 115, pp. 116–125, 2018.

[17] V. Sebian, V. Necas, and P. Darilek, "Transmutation of spent fuel in reactor VVER-440," *Journal of Electrical Engineering*, vol. 52, no. 9-10, pp. 299–302, 2001.

[18] B. R. Bergelson, A. S. Gerasimov, and G. V. Tikhomirov, "Transmutation of actinides in power reactors," *Radiation Protection Dosimetry*, vol. 116, no. 1–4, pp. 675–678, 2005.

[19] W. Hu, B. Liu, X. Ouyang et al., "Minor actinide transmutation on PWR burnable poison rods," *Annals of Nuclear Energy*, vol. 77, pp. 74–82, 2015.

[20] W. Hu, J. Jing, J. Bi, C. Zhao, B. Liu, and X. Ouyang, "Minor actinides transmutation on pressurized water reactor burnable poison rods," *Annals of Nuclear Energy*, vol. 110, pp. 222–229, 2017.

[21] OECD/NEA, *A VVER-1000 LEU and MOX Assembly ComputationalBenchmark*, vol. 10, Nuclear Energy Agency, NEA/NSC/DOC, Paris, France, 2002.

[22] K. Okumura, T. Kugo, K. Kaneko, and K. Tsuchihashi, *SRAC2006: A Comprehensive Neutronics Calculation Code System*, JAEA-Data/Code 2007-004, Tokai, Japan, 2007.

[23] D. B. Pelowitz, *MCNP6TM User's Manual*, Los Alamos National Laboratory, Santa Fe, NM, USA, 2013.

[24] A. Kotchetkov, I. Krivitskiy, N. Rabotnov, A. Tsiboulia, and S. Iougai, "Calculation and experimental studies on minor actinides reactor transmutation," in *Proceedings of the Fifth OECD/NEA Information Exchange Meeting on Actinide and Fission Product Partitioning and Transmutation*, pp. 289–303, Mol, Belgium, November 1998.

[25] F. Brown, W. Martin, G. Yesilyurt, and S. Wilderman, *On-The-Fly Neutron Doppler Broadening for MCNP*, Los Alamos National Laboratory, Santa Fe, NM, USA, 2012.

[26] H. N. Tran, V. K. Hoang, P. H. Liem, and H. T. P. Hoang, "Neutronics design of VVER-1000 fuel assembly with burnable poison particles," *Nuclear Engineering and Technology*, vol. 51, no. 7, pp. 1729–1737, 2019.

[27] L. Frybortova, "Recommended strategy and limitations of burnable absorbers used in VVER fuel assemblies," *Nuclear Science and Techniques*, vol. 30, no. 8, p. 129, 2019.

[28] P. Cudrnak and V. Necas, "Optimization of fuel assembly with gadolinium for LWRS," *Journal of Power Technologies*, vol. 91, no. 4, pp. 186–190, 2011.

Hindawi
Science and Technology of Nuclear Installations
Volume 2019, Article ID 6572606, 6 pages
https://doi.org/10.1155/2019/6572606

Research Article

Contribution of Ternary Reaction to Pd Sorption on MX-80 in Na-Ca-Cl Solution at High Ionic Strength

Shinya Nagasaki, Justin Riddoch, and Joshua Racette

Department of Engineering Physics, McMaster University, 1280 Main Street West, Hamilton L8S 4L7, Canada

Correspondence should be addressed to Shinya Nagasaki; nagasas@mcmaster.ca

Received 1 April 2019; Revised 23 May 2019; Accepted 10 June 2019; Published 24 June 2019

Guest Editor: Rema Abdulaziz

In this study, we first examined the sorption of Pd on MX-80 in Na-Ca-ClO_4 solution as a function of pH_c (3–9) and ionic strength (0.1 M–4 M) and confirmed that the experimentally derived K_d values could be fitted by a 2-site protolysis nonelectrostatic surface complexation and cation exchange (2SPNE SC/CE) model using three binary surface complexation constants previously estimated. Then, we investigated the sorption of Pd on MX-80 in Na-Ca-Cl-ClO_4 solution as a function of pH_c (3–9) and Cl^-/ClO_4^- molar concentration ratio (0–∞) at the ionic strength = 4 M. We found that the sorption of Pd on MX-80 in Na-Ca-Cl-ClO_4 solution could be simulated only by the three binary and one ternary surface complexations (S-OH + Pd^{2+} + 4Cl^- ⟷ S-OPdCl_4^{3-} + H^+). This suggests that the contribution of other ternary surface complexations such as ≡S-OH + Pd^{2+} + xCl^- ⟷ ≡S-OP$dCl_x^{(x-1)-}$ + H^+ (x = 1, 2 and 3) to Pd sorption in Na-Ca-Cl-ClO_4 solution with ionic strength = 4 M was negligibly small.

1. Introduction

Canadian sedimentary rocks are being considered as potential host rocks for a deep geologic repository (DGR) for used nuclear fuel. Some of these rocks in Canada (for example, Southern Ontario, Michigan Basin [1]) contain Na-Ca-Cl type brine solutions with total dissolved solids (TDS) concentration up to 350 g/L or with the ionic strength (I) as high as 7.2 M. Sorption of radionuclides onto host rocks surrounding a DGR and onto materials comprising the engineered barrier system is considered an important mechanism for retarding their subsurface transport from the repository to the biosphere [2–6]. Therefore, it is important to elucidate the sorption behaviour of radionuclides not only on host rocks, but also on engineered barrier materials such as bentonite.

The Nuclear Waste Management Organization of Canada (NWMO) has been maintaining a database of sorption distribution coefficients, K_d, for Canadian sedimentary rocks and bentonite [2]. Palladium is selected as an element of interest by the NWMO, but the only existing relevant sorption data for Pd on bentonite had been measured in 0.01 and 0.1 M NaCl solutions [7]. Hence, sorption of Pd onto Queenston shale, illite (the major mineral constituent of Queenston shale), and MX-80 bentonite (the candidate material for engineered barrier in Canada) in Na-Ca-Cl solutions with pH_c ranging from 3 to 9 and I ranging from 0.01 M to 6 M was studied in our previous paper [8]. The 2-site protolysis nonelectrostatic surface complexation and cation exchange (2SPNE SC/CE) model [9, 10] with SIT parameters was applied to the pH_c dependence of K_d values for illite and MX-80 ($I \leq 4$ M), and the optimized surface complexation and cation exchange constants were estimated [8]. Since Pitzer parameters for Pd in Na-Ca-Cl solution are not completely compiled, we did not apply the 2SPNE SC/CE model to the K_d values at I = 6 M. We found that Pd sorption could largely be accounted for with the formation of the ≡S-OPdOH, ≡S-$OPd(OH)_2^-$, ≡S-$OPdCl_4^{3-}$ surface species, and the ≡S-O_2Pd exchange species with 2Na^+ for both sorbents, with the additional ≡S-OPd^+ surface species for MX-80. We included four possible ternary surface complexations (≡S-OH + Pd^{2+} + xCl^- ⟷ ≡S-$OPdCl_x^{(x-1)-}$ + H^+; x = 1 – 4) in the fitting by 2SPNE SC/CE model, but only one reaction (≡S-OH + Pd^{2+} + 4Cl^- ⟷ ≡S-$OPdCl_4^{3-}$ + H^+) was found to contribute to the sorption in Na-Ca-Cl solutions with high I.

In this work, we first measured the sorption of Pd on MX-80 in Na-Ca-ClO_4 solutions as a function of pH_c and I and studied whether the experimentally derived K_d values in the absence of Cl^- can be simulated by using our previously optimized constants. Then, we measured the sorption of Pd on MX-80 in Na-Ca-Cl-ClO_4 solutions as a function of pH_c and Cl^-/ClO_4^- molar concentration ratio (0–∞) at I = 4 M and investigated the contribution of ternary surface complexation to the Pd sorption on MX-80 at I = 4 M.

2. Materials and Methods

2.1. Chemicals, Solids, and Solutions. All chemicals used were reagent grade and were supplied from Fisher Scientific. Deionized water was prepared using a Milli-Q Direct 8 (18.2 MΩ·cm). The MX-80 bentonite sample was supplied by the American Colloid Company and was used as received. Pd used in experiments was derived from a 1000 ± 1 μg/mL standard solution with a natural isotopic abundance supplied by Agilent Technology. A Precise Controlled Atmosphere Glove Box (GB) supplied by Labconco was filled with N_2 gas (>99.999 %). The concentration of O_2 in the GB was smaller than 2 ppm.

The reference brine solution in Southern Ontario, SR-270-PW, is proposed by the NWMO [2]. It has a Na/Ca molar concentration ratio of 2.7. In this study, Na-Ca-ClO_4 solutions (Na/Ca molar concentration ratio = 2.7) with I = 0.1, 1, 2, 4 M were prepared by $NaClO_4 \cdot H_2O$ and $Ca(ClO_4)_2 \cdot 4H_2O$, and Na-Ca-Cl-ClO_4 solutions (Na/Ca ratio = 2.7; Cl^-/ClO_4^- ratio = 0.01, 0.1, 1, 10, 100, ∞) with I = 4 M were prepared by NaCl, $CaCl_2 \cdot 2H_2O$, and $NaClO_4 \cdot H_2O$. Na-Ca-ClO_4 solution with I = 4 M was considered a case of Cl^-/ClO_4^- ratio = 0.

The pH values indicated on the pH meter ($pH_{measure}$) should be considered as operational values at high ionic strength ($I \geq 0.1$ M) [11]. The relationships between the operational $pH_{measure}$ and the molar H^+ concentrations ($pH_c = -\log c_{H+}$) or the molal H^+ concentration ($pH_m = -\log m_{H+}$) were discussed in detail by Altmaier et al. [12, 13]. In this study, the relationships between $pH_{measure}$ (Fisher Scientific Accumet AB 150/micro accupHast pH combination electrode) and pH_c in solutions were determined by titration (Metrohm Ti-Touch 916), and the $pH_{measure}$ values were converted to the pH_c values.

2.2. Sorption Experiments. All sorption experiments were carried out in triplicate at 25°C. In preliminary tests, the sorption of Pd on the wall of a polycarbonate reaction vessel was found to be negligible. Initial concentration of Pd for all sorption tests was 1.0×10^{-7} M and was confirmed to be smaller than solubility of Pd [8]. The liquid/solid ratio was set to be 0.5 m^3/kg.

We followed the sorption experimental procedure we conducted in Np(V) and Np(IV) sorption previously [14–16]. In the GB, MX-80 was added into a polycarbonate reaction vessel and Na-Ca-ClO_4 or Na-Ca-Cl-ClO_4 solution was added into the reaction vessel. The suspensions were kept in the GB for 3 to 4 days for preequilibration (the pH_c of solutions in contact with MX-80 was confirmed to be stabilized within 1 day in the preliminary tests). The reaction vessels were removed from the GB and the liquid and solid were separated by centrifugation for 120 min at 18,000 rpm (Beckman Coulter, Allegra X-30R). The reactions vessels were then transferred back into the GB and the liquid was removed by pipette. Na-Ca-ClO_4 or Na-Ca-Cl-ClO_4 solution was then added into the reaction vessel again, and a portion of the Pd standard solution was spiked into the reaction vessel. The pH_c of the solution was adjusted to the predecided values at $3 \leq pH_c \leq 9$ by addition of 0.01 M $HClO_4$, 0.01 M HCl, or 0.01 M NaOH solution in the GB, and the reaction vessel was tightly sealed. Change in I and Cl^-/ClO_4^- ratio by addition of $HClO_4$, HCl, or NaOH could be neglected.

The reaction vessels were transferred from the GB to an incubator at 25°C (Infors HT Ectron) and were shaken for 14 days. Fourteen days were enough to reach to the sorption equilibrium [8]. The pH_c of the solution was measured once a day in the GB and readjusted to the original pH_c value if the pH_c changed by more than ± 0.3 from the original value. After 14 days, the liquid was separated from the solid by centrifugation for 120 minutes at 18,000 rpm at 25°C. We previously confirmed that the liquid phase was sufficiently separated from the solid phase by this method [14]. The pH_c of the liquid was measured in the GB, and an aliquot was sampled from the liquid phase of each reaction vessel. The concentration of Pd in the aliquot was measured by ICP-MS (Agilent ICP-MS 8800).

The K_d value (m^3/kg) is calculated according to Equation (1), where C_i is the initial concentration of Pd in solution (1.0×10^{-7} M), C_{eq} the concentration at sorption equilibrium (M), L the volume of liquid used in the sample (m^3), and M the mass of solid used (kg). In this paper, the sorption of Pd on MX-80 is described by K_d values.

$$K_d = \frac{C_i - C_{eq}}{C_{eq}} \times \frac{L}{M} \quad (1)$$

2.3. Sorption Modelling. The pH_c, I, and Cl^-/ClO_4^- ratio dependence of K_d values for MX-80 was fitted using the 2SPNE SC/CE model with the program PHREEQC [17]. The specific-ion interaction theory (SIT) was used for the computational method, as it accounts for the electrostatic interactions of all other ions in solution with the one ion of interest. This is necessary for accuracy when computing activity coefficients in solutions of high I. The Pitzer computational method can be more accurate in higher I solutions; however, Pitzer parameters for Pd were not completely known at the present. SIT is known to be inaccurate at I > 4.0 M and, therefore, sorption was modelled at $I \leq 4.0$ M in this study [18].

The Japan Atomic Energy Agency (JAEA) thermodynamic database (TDB) was chosen as the reference database since it contains the necessary thermodynamic data for Pd [19]. However, no thermodynamic data for $PdOH^+$ and $Pd(OH)_4^{2-}$ are available in JAEA TDB, so the values contained in the SIT database (v9a) included in the PHREEQC [20] were added to the JAEA TDB. The hydrolysis and

Table 1: Thermodynamic data of Pd(II) species used in this work [19, 20].

Hydrolysis and complexation reaction	log K	Reference
$Pd^{2+} + H_2O - H^+ \longleftrightarrow PdOH^+$	1.86	[18]
$Pd^{2+} + 2H_2O - 2H^+ \longleftrightarrow Pd(OH)_2$	-3.49	[17]
$Pd^{2+} + 3H_2O - 3H^+ \longleftrightarrow Pd(OH)_3^-$	-15.48	[17]
$Pd^{2+} + 4H_2O - 4H^+ \longleftrightarrow Pd(OH)_4^{2-}$	-29.36	[18]
$Pd^{2+} + Cl^- \longleftrightarrow PdCl^+$	5.00	[17]
$Pd^{2+} + 2Cl^- \longleftrightarrow PdCl_2$	8.42	[17]
$Pd^{2+} + 3Cl^- \longleftrightarrow PdCl_3^-$	10.93	[17]
$Pd^{2+} + 4Cl^- \longleftrightarrow PdCl_4^{2-}$	13.05	[17]
$Pd^{2+} + 3Cl^- + H_2O - H^+ \longleftrightarrow PdCl_3OH^{2-}$	3.77	[17]

Table 2: Optimized surface complexation and cation exchange constants [8].

Sorption reaction	log K
Binary surface complexation:	
$\equiv$S-OH + $Pd^{2+} \longleftrightarrow \equiv$S-OP$d^+ + H^+$	8.2 ± 0.2
$\equiv$S-OH + $Pd^{2+} + H_2O \longleftrightarrow \equiv$S-OPdOH + $2H^+$	2.3 ± 0.2
$\equiv$S-OH + $Pd^{2+} + 2H_2O \longleftrightarrow \equiv$S-OP$d(OH)_2^- + 3H^+$	-5.5 ± 0.2
Ternary surface complexation:	
$\equiv$S-OH + $Pd^{2+} + 4Cl^- \longleftrightarrow \equiv$S-OP$dCl_4^{3-} + H^+$	13.05 ± 0.2
Cation exchange:	
$2\equiv$S-ONa + $Pd^{2+} \longleftrightarrow (\equiv$S-O$)_2$Pd + $2Na^+$	5.90 ± 0.2

complexation constants used in this work are summarized in Table 1.

The specific surface area and the cation exchange capacity of MX-80 were 26.2 m^2/g [21] and 102.1 meq/100g [22], respectively. However, the sorption site capacity was not measured. Hence, we assumed that the sorption site capacity is proportional to the specific surface area [14]. As shown in Supplementary Materials, the contribution of cation exchange reaction to the sorption of Pd on MX-80 was negligibly small. Therefore, the slight difference in the value of the cation exchange capacity did not affect the calculation results. Since the concentration of Pd in the solution was much smaller than the total sorption site number in the MX-80 used, the slight difference in the value of the specific surface area also did not influence the calculation results.

In the 2SPNE SC/CE model, Bradbury and Baeyens considered both strong and weak surface sites [9, 10]. In our previous work [8], we could simulate the Pd sorption on MX-80 in Na-Ca-Cl solution by considering the strong site only and estimate the optimized surface complexation and cation exchange constants at I = 0 M, as shown in Table 2.

For the Pd sorption in Na-Ca-ClO_4 solutions, the 2SPNE SC/CE model calculation was conducted using the binary surface complexation and cation exchange constants illustrated in Table 2.

For the Pd sorption in Na-Ca-Cl-ClO_4 solutions, we included the additional three ternary surface complexations ($\equiv$S-OH + Pd^{2+} + xCl^- $\longleftrightarrow \equiv$S-OP$dCl_x^{(x-1)-}$ + H^+; x = 1 – 3) in the modelling. Bradbury and Baeyens proposed the linear free energy relationships (LFER) between the surface complexation constants for montmorillonite and the hydrolysis constants [9]. In the fitting of the 2SPNE SC/CE model to the K_d values experimentally derived, we set the initial values for additional ternary surface complexation constants, by assuming that the proposed LFER equation for montmorillonite can be used for the surface complexation constants and the $PdCl_x^{(x-2)-}$ complexation constants (x = 1 – 3). The initial value of ternary surface complexation constant for $\equiv$S-OH + Pd^{2+} + $4Cl^-$ $\longleftrightarrow \equiv$S-OP$dCl_4^{3-}$ + H^+ was set as 13.05. In the fitting, the values of four ternary sorption reaction constants were used as the fitting parameters to obtain the best optimized fitting, and other values were fixed.

3. Results and Discussion

3.1. Sorption in Na-Ca-ClO_4 Solution. The pH_c and I dependence of K_d values for MX-80 is plotted in Figure 1. It was found that the K_d values decreased with pH_c (3–7) and then became constant against pH_c (7–10). Little dependence of K_d values on I was also observed. These tendencies are consistent with the previous study by Tachi et al. [7].

The 2SPNE SC/CE model with the binary surface complexation and cation exchange constants previously estimated in the Na-Ca-Cl solutions [8] was applied to the pH_c and I dependence of K_d values in the Na-Ca-ClO_4 solutions. The model calculation results are also illustrated in Figure 1. We could find the consistency between the experimental and calculation results.

In the pH region of 3 – 10, $Pd(OH)_2$ is a dominant species in the solution (Pd speciation in Na-Ca-ClO_4 solution at I = 4 M is shown in Figure S-1. Pd speciation at I < 4 M is not shown here). As shown in Figure S-8, the binary

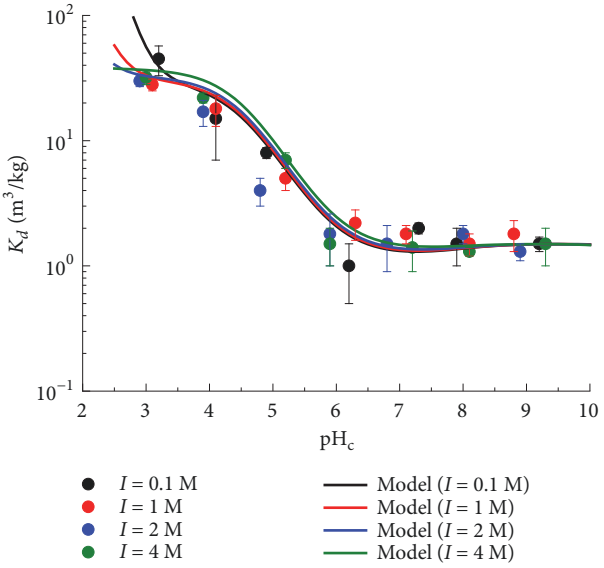

FIGURE 1: pH$_c$ and I dependence of K_d in Na-Ca-ClO$_4$ solutions. Plots are the experimentally measured K_d values. The solid lines are the 2SPNE SC/CE model calculation results. The error bars represent the standard deviation of triplicate measurements.

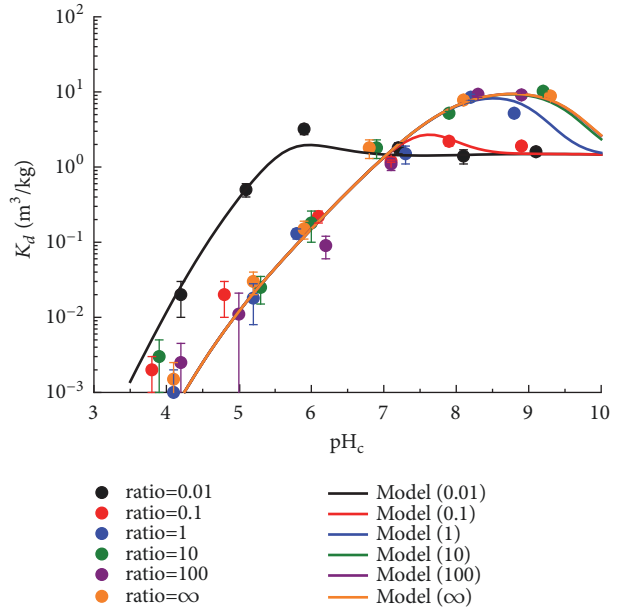

FIGURE 2: pH$_c$ and Cl^-/ClO_4^- molar concentration ratio dependence of K_d in Na-Ca-Cl-ClO$_4$ solutions at I = 4 M. Plots are the experimentally measured K_d values. The solid lines are the 2SPNE SC/CE model calculation results. The error bars represent the standard deviation of triplicate measurements.

surface complexations ≡S-OH + Pd^{2+} ⟷ ≡S-OPd$^+$ + H^+, ≡S-OH + Pd^{2+} + H_2O ⟷ ≡S-OPdOH + 2H^+, and ≡S-OH + Pd^{2+} + 2H_2O ⟷ ≡S-OPd(OH)$_2^-$ + 3H^+ dominate the sorption at pH = 3–6, 6–8, and 8–10, respectively. This indicates that Pd sorbs on MX-80 markedly in the acidic pH region through the ≡S-OH + Pd^{2+} ⟷ ≡S-OPd$^+$ + H^+ surface complexation in the absence of Cl^-. From Figure S-8, the contribution of cation exchange reaction was also found to be negligibly small. These demonstrate that the binary surface complexation constants we previously estimated [8] can be used to simulate the sorption of Pd on MX-80 in the Na-Ca-ClO$_4$ solutions quantitatively.

3.2. Sorption in Na-Ca-Cl-ClO$_4$ Solutions. Figure 2 illustrates the pH$_c$ and Cl^-/ClO_4^- ratio dependence of K_d values for MX-80. We found that the K_d values at pH$_c$ < 7 decreased as the Cl^-/ClO_4^- ratio increased. Particularly, the K_d values at pH$_c$ < 6 for MX-80 were drastically suppressed in the presence of Cl^- even at Cl^-/ClO_4^- ratio = 0.01, compared to the K_d values in the absence of Cl^- (Figure 1). On the other hand, the K_d values at pH$_c$ = 7 – 9 slightly increased with Cl^-/ClO_4^- ratio up to 1 and did not change any more at Cl^-/ClO_4^- ratio ≥ 10.

The Pd speciation in Na-Ca-Cl-ClO$_4$ solutions at I = 4 M at Cl^-/ClO_4^- ratio = 0.01, 0.1, 1, 10, 100 and infinity are shown in Figures S-2–S-7, respectively. It was found that the pH region of $PdCl_4^{2-}$ dominance expanded with Cl^-/ClO_4^- ratio, while that of Pd(OH)$_2$ dominance shrank. Figure 2 suggests that the formation of $PdCl_4^{2-}$ complex strongly suppressed the Pd sorption, especially the surface complexation ≡S-OH + Pd^{2+} ⟷ ≡S-OPd$^+$ + H^+, on MX-80 at pH$_c$ < 7.

The fitting results of the 2SPNE SC/CE model to the experimentally measured K_d values using three binary and four ternary surface complexations and cation exchange reaction are also drawn in Figure 2. It was shown that the pH$_c$ dependence of K_d values in the wide range of Cl^-/ClO_4^- ratio could be also quantitatively fitted by the 2SPNE SC/CE model. It was found that the fitting results could be obtained only with three binary and one ternary surface complexations as we studied in Na-Ca-Cl solutions [8]. Namely, only the ternary surface complexation, ≡S-OH + Pd^{2+} + 4Cl^- ⟷ ≡S-OPdCl_4^{3-} + H^+, among the four complexations considered in the modelling contributed to the Pd sorption on MX-80 in Na-Ca-Cl-ClO$_4$ solutions. The contribution of other three ternary surface complexations was negligible. The surface complexation constant for this ternary sorption reaction was estimated as 13.3 ± 0.3. This value is consistent with 13.05 ± 0.2 which was previously estimated [8].

The pH dependence of surface complexation and cation exchange reaction at Cl^-/ClO_4^- ratio = 0, 0.01, 0.1, 1, 10, 100 and infinity is shown in Figures S-8–S-14, respectively. Three binary surface complexations dominated the sorption at Cl^-/ClO_4^- ratio = 0. In the presence of Cl^-, the surface complexation, ≡S-OH + Pd^{2+} ⟷ ≡S-OPd$^+$ + H^+, was drastically suppressed even at Cl^-/ClO_4^- ratio = 0.01. As the Cl^-/ClO_4^- ratio increased, the contribution of surface complexations, ≡S-OH + Pd^{2+} ⟷ ≡S-OPd$^+$ + H^+ and ≡S-OH + Pd^{2+} + H_2O ⟷ ≡S-OPdOH + 2H^+, became small and was finally zero. This led to the decrease in the measured K_d values at pH$_c$ < 7. On the other hand, the contribution of ternary surface complexation, ≡S-OH + Pd^{2+} + 4Cl^- ⟷

≡S-$OPdCl_4^{3-}$ + H^+, became large at Cl^-/ClO_4^- ratio = 0.1 and was significant and dominated the sorption at Cl^-/ClO_4^- ratio ≥ 1. The increase in the measured K_d values at pH_c 7–9 was attributed to this ternary surface complexation.

The complexation constant for Pd^{2+} + $3Cl^-$ + H_2O - $H^+ \longleftrightarrow PdCl_3OH^{2-}$ is compiled in the JAEA TDB (Table 1). Although $PdCl_3OH^{2-}$ did not appear in Na-Ca-Cl-ClO_4 solutions at I = 4 M (Figures S-1–S-7), the 2SPNE SC/CE model including the ternary surface complexation ≡S-OH + Pd^{2+} + $3Cl^-$ + $H_2O \longleftrightarrow$ ≡S-$OPdCl_3OH^{3-}$ + $2H^+$ was also applied to the measured K_d values to make sure of the contribution of ternary surface complexation in the Pd sorption on MX-80. However, it was found that this ternary surface complexation could be negligible.

4. Conclusions

The K_d values of Pd for MX-80 were systematically measured as a function of pH_c, I, and Cl^-/ClO_4^- molar concentration ratio in Na-Ca-ClO_4 ($3 \le pH_c \le 9$ and $0.1\ M \le I \le 4M$) and Na-Ca-Cl-ClO_4 ($3 \le pH_c \le 9$ and $0 \le Cl^-/ClO_4^-$ ratio $\le \infty$; I = 4 M) solutions.

It was found that the pH_c, I, and Cl^-/ClO_4^- ratio dependence of K_d values was quantitatively fitted by the 2SPNE SC/CE model. The model calculation indicated that, in the presence of Cl^-, the contributions of binary surface complexations were suppressed while that of the ternary surface complexation dominated the sorption as the Cl^-/ClO_4^- ratio increased.

It was also found that the pH_c dependence of K_d values for MX-80 in the Na-Ca-Cl-ClO_4 solutions at I = 4 M could be simulated by considering only one ternary surface complexation reaction (≡S-OH + Pd^{2+} + $4Cl^-$ $\longleftrightarrow$ ≡S-$OPdCl_4^{3-}$ + H^+) besides the binary surface complexation reactions in all range of Cl^-/ClO_4^- ratio (0–∞).

Data Availability

The sorption data used to support the findings of this study are available from the corresponding author upon request.

Conflicts of Interest

The authors declare that there are no conflicts of interest regarding the publication of this paper.

Acknowledgments

The authors would like to show their gratitude to Dr. Takumi Saito (the University of Tokyo), Drs. Tetsuji Yamaguchi, Yoshihisa Iida, Yukio Tachi, and Akira Kitamura (Japan Atomic Energy Agency), Dr. Tammy Yang (Nuclear Waste Management Organization of Canada), and Dr. Peter Vilks (Canadian Nuclear Laboratories) for their fruitful and valuable comments throughout this work and would like to thank Dr. Naoki Sugiyama and Mr. Wijdan Malik of Agilent Technologies for helpful discussion on the Pd measurement and improvement of detection limit of Pd by ICP-MS. This research was supported by NSERC Discovery Grant (RGPIN-2014-05732).

Supplementary Materials

Figure S-1: Pd speciation in Na-Ca-Cl-ClO_4 solution (Cl^-/ClO_4^- molar concentration ratio = 0) at I = 4 M. Figure S-2: Pd speciation in Na-Ca-Cl-ClO_4 solution (Cl^-/ClO_4^- molar concentration ratio = 0.01) at I = 4 M. Figure S-3: Pd speciation in Na-Ca-Cl-ClO_4 solution (Cl^-/ClO_4^- molar concentration ratio = 0.1) at I = 4 M. Figure S-4: Pd speciation in Na-Ca-Cl-ClO_4 solution (Cl^-/ClO_4^- molar concentration ratio = 1) at I = 4 M. Figure S-5: Pd speciation in Na-Ca-Cl-ClO_4 solution (Cl^-/ClO_4^- molar concentration ratio = 10) at I = 4 M. Figure S-6: Pd speciation in Na-Ca-Cl-ClO_4 solution (Cl^-/ClO_4^- molar concentration ratio = 100) at I = 4 M. Figure S-7: Pd speciation in Na-Ca-Cl-ClO_4 solution (Cl^-/ClO_4^- molar concentration ratio = ∞) at I = 4 M. Figure S-8: Pd sorption reaction on MX-80 in Na-Ca-Cl-ClO_4 solution (Cl^-/ClO_4^- molar concentration ratio = 0) at I = 4 M. Figure S-9: Pd sorption reaction on MX-80 in Na-Ca-Cl-ClO_4 solution (Cl^-/ClO_4^- molar concentration ratio = 0.01) at I = 4 M. Figure S-10: Pd sorption reaction on MX-80 in Na-Ca-Cl-ClO_4 solution (Cl^-/ClO_4^- molar concentration ratio = 0.1) at I = 4 M. Figure S-11: Pd sorption reaction on MX-80 in Na-Ca-Cl-ClO_4 solution (Cl^-/ClO_4^- molar concentration ratio = 1) at I = 4 M. Figure S-12: Pd sorption reaction on MX-80 in Na-Ca-Cl-ClO_4 solution (Cl^-/ClO_4^- molar concentration ratio = 10) at I = 4 M. Figure S-13: Pd sorption reaction on MX-80 in Na-Ca-Cl-ClO_4 solution (Cl^-/ClO_4^- molar concentration ratio = 100) at I = 4 M. Figure S-14: Pd sorption reaction on MX-80 in Na-Ca-Cl-ClO_4 solution (Cl^-/ClO_4^- molar concentration ratio = ∞) at I = 4 M. *(Supplementary Materials)*

References

[1] M. Y. Hobbs, S. K. Frape, O. Shouakar-Stash, and L. R. Kennel, "Regional hydrogeochemistry – Southern Ontario," NWMO DGR-TR-2011-12, Nuclear Waste Management Organization, 2011.

[2] P. Vilks, "Sorption of selected radionuclides on sedimentary rocks in saline conditions - Literature review," NWMO TR-2011-12, Nuclear Waste Management Organization, 2011.

[3] H. Geckeis, J. Lützenkirchen, R. Polly, T. Rabung, and M. Schmidt, "Mineral–water interface reactions of actinides," *Chemical Reviews*, vol. 113, no. 2, pp. 1016–1062, 2012.

[4] M. Zavarin, B. A. Powell, M. Bourbin, P. Zhao, and A. B. Kersting, "Np(V) and Pu(V) ion exchange and surface-mediated reduction mechanisms on montmorillonite," *Environmental Science & Technology*, vol. 46, no. 5, pp. 2692–2698, 2012.

[5] N. Chapman, M. Apted, W. Aspinall et al., "TOPAZ Project long-term tectonic hazard to geological repositories," NUMO-TR-12-05, Nuclear Waste Management Organization of Japan, 2012.

[6] National Academy of Science, *A Study of The Isolation for Geologic Disposal of Radioactive Wastes*, Waste Isolation Systems Panels, Board on Radioactive Waste Management, Washington DC, USA, 1983.

[7] Y. Tachi, T. Shibutani, H. Sato, and M. Shibata, "Sorption and diffusion behavior of palladium in bentonite, granodiorite and tuff," JNC TN8400 99-088, Japan Nuclear Fuel Cycle Development Institute, 1999.

[8] J. Goguen, A. Walker, J. Riddoch, and S. Nagasaki, "Sorption of Pd on illite, MX-80 and shale in Na-Ca-Cl solutions," *Nuclear Engineering and Technology (submitted)*.

[9] M. H. Bradbury and B. Baeyens, "Modelling the sorption of Mn(II), Co(II), Ni(II), Zn(II), Cd(II), Eu(III), Am(III), Sn(IV), Th(IV), Np(V) and U(VI) on montmorillonite: Linear free energy relationships and estimates of surface binding constants for some selected heavy metals and actinides," *Geochimica et Cosmochimica Acta*, vol. 69, no. 4, pp. 875–892, 2005.

[10] M. Bradbury and B. Baeyens, "Sorption modelling on illite. Part II: Actinide sorption and linear free energy relationships," *Geochimica et Cosmochimica Acta*, vol. 73, no. 4, pp. 1004–1013, 2009.

[11] T. Fanghänel, V. Neck, and J. I. Kim, "The ion product of H2O, dissociation constants of H2CO3 and Pitzer parameters in the system Na+/H+/OH-/HCO-3/CO 2-3/ClO-4/H2O at 25∘C," *Journal of Solution Chemistry*, vol. 25, no. 4, pp. 327–343, 1996.

[12] M. Altmaier, V. Metz, V. Neck, R. Müller, and T. Fanghänel, "Solid-liquid equilibria of Mg(OH)2(cr) and Mg2(OH) 3Cl·4H2O(cr) in the system Mg-Na-H-OH-Cl- H2O at 25∘C," *Geochimica et Cosmochimica Acta*, vol. 67, no. 19, pp. 3595–3601, 2003.

[13] M. Altmaier, V. Neck, and T. Fanghänel, "Solubility of Zr(IV), Th(IV) and Pu(IV) hydrous oxides in CaCl2 solutions and the formation of ternary Ca-M(IV)-OH complexes," *Radiochimica Acta*, vol. 96, no. 9-11, pp. 541–550, 2008.

[14] S. Nagasaki, "Sorption properties of Np on shale, illite and bentonite under saline, oxidizing and reducing conditions," NWMO-TR-2018-02, Nuclear Waste Management Organization, 2018.

[15] S. Nagasaki, T. Saito, and T. T. Yang, "Sorption behavior of Np(V) on illite, shale and MX-80 in high ionic strength solutions," *Journal of Radioanalytical and Nuclear Chemistry*, vol. 308, no. 1, pp. 143–153, 2016.

[16] S. Nagasaki, J. Riddoch, T. Saito, J. Goguen, A. Walker, and T. T. Yang, "Sorption behaviour of Np(IV) on illite, shale and MX-80 in high ionic strength solutions," *Journal of Radioanalytical and Nuclear Chemistry*, vol. 313, pp. 1–11, 2017.

[17] D. L. Parkhurst and C. A. J. Appelo, "User's Guide to PHREEQC (Version 2) (Equations on which the program is based," Water-Resources Investigations Report 99-4259, U.S. Department of the Interior, U.S. Geological Survey, 1999.

[18] I. Grenthe and A. Plyasunov, "On the use of semiempirical electrolyte theories for the modeling of solution chemical data," *Pure and Applied Chemistry*, vol. 69, no. 5, pp. 951–958, 1997.

[19] Thermodynamic Database, Japan Atomic Energy Agency, TDB Ver. 2014/03, June 2014, https://migrationdb.jaea.go.jp/cgi-bin/db_menu.cgi?title=TDB&ej=1.

[20] PHREEQC (Version 3) – A computer program for speciation, batch-reaction, one-dimensional transport, and inverse geochemical calculations, United States Geological Survey, 2017, https://wwwbrr.cr.usgs.gov/projects/GWC_coupled/phreeqc/.

[21] F. P. Bertetti, "Determination of sorption properties for sedimentary rocks under saline, reducing conditions – Key radionuclides," NWMO-TR-2016-08, Nuclear Waste Management Organization, 2016.

[22] E. Galunin, M. D. Alba, M. J. Santos, T. Abrão, and M. Vidal, "Lanthanide sorption on smectitic clays in presence of cement leachates," *Geochimica et Cosmochimica Acta*, vol. 74, no. 3, pp. 862–875, 2010.

Hindawi
Science and Technology of Nuclear Installations
Volume 2019, Article ID 6789506, 13 pages
https://doi.org/10.1155/2019/6789506

Research Article

Logistical Simulation Modeling for Planning a Soil Remediation Process

David Kessel, Jihan Jeon, Jaeyeon Jung, Eutteum Oh, and Chang-Lak Kim

KEPCO International Nuclear Graduate School, 658-91 Haemaji-ro, Seosaeng-myeon, Ulju-gun, Ulsan 54014, Republic of Korea

Correspondence should be addressed to Chang-Lak Kim; clkim@kings.ac.kr

Received 15 November 2018; Revised 11 March 2019; Accepted 9 April 2019; Published 2 May 2019

Guest Editor: Rema Abdulaziz

This paper describes the development of a discrete event simulation model using the FlexSim software to support planning for soil remediation at Korean nuclear power plants that are undergoing decommissioning. Soil remediation may be required if site characterization shows that there has been radioactive contamination of soil from plant operations or the decommissioning process. The simulation model was developed using a dry soil separation and soil washing process. Preliminary soil data from the Kori 1 nuclear power plant was used in the model. It was shown that a batch process such as soil washing can be effectively modeled as a discrete event process. Efficient allocation of resources and efficient waste management including volume and classification reduction can be achieved by use of the model for planning the soil remediation process. Cost will be an important criterion in the choice of suitable technologies for soil remediation but is not included in this conceptual model.

1. Introduction

This paper describes the development of a conceptual simulation model that can be used for logistics planning for site remediation at Korean nuclear power plants and specifically the Kori 1 reactor site. A FlexSim discrete event simulation model of the site soil remediation and waste management process was developed to support optimization of performance, resources, and time and to minimize nuclear waste. Cost will be an important criterion in the choice of suitable technologies for soil remediation but is not included in this first conceptual model.

Kori Unit 1, the oldest nuclear power plant (NPP) in Korea, was permanently shut down in June 2017. The decommissioning of Kori Unit 1 will follow in the future and site remediation will be carried out at the end of the decommissioning project.

Operation of a nuclear power plant may lead the release of radioactive materials to the soil and groundwater at the site which could migrate to the surrounding environment. Small radioactive releases may not be discovered until the NPP undergoes decommissioning and must be remediated to prevent migration of radioactive materials [1].

Nuclear power plant site remediation is performed after site structures have been removed and is the last step in decommissioning. Remediation may be required remove contamination from the site soil to allow the reuse of the site subject to the regulatory requirements for site release.

Site remediation has two safety-related objectives. One is to reduce radiation exposure to workers and the general public, and the other is to reduce the radioactivity to the level required for the intended use of the site after its release.

Korea does not have domestic experience in NPP decommissioning and site remediation. Furthermore, the decommissioning and remediation work at Kori 1 has not started and so the site soil and groundwater conditions have not been characterized. The extent and nature of radioactive contamination at the site is uncertain, and as such the development of this simulation model must be preliminary. This does not diminish the fact that effective planning is necessary to reduce project uncertainty and risk to achieve the site remediation objectives.

A review of the literature for site remediation has shown that simulation modeling is a useful tool for planning decommissioning and site remediation. The literature has also shown the value of simulation models for design and optimization of industrial processes. In order to develop a preliminary simulation model, soil washing was chosen for the remediation technology.

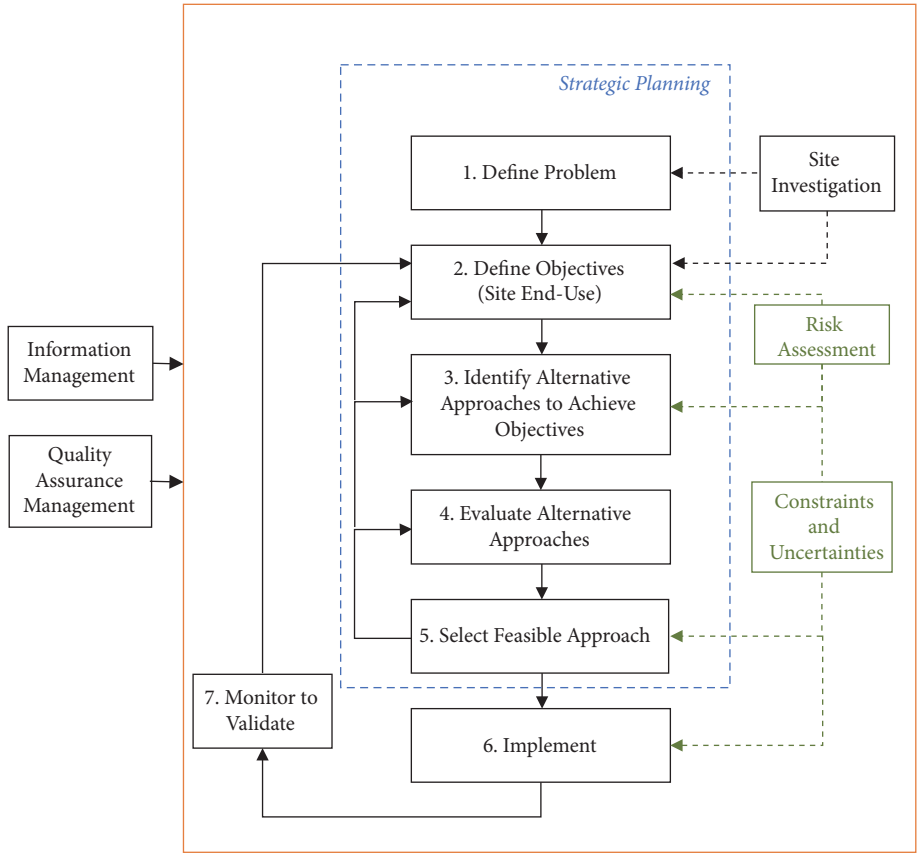

Figure 1: IAEA integrated planning process [1].

Once decommissioning commences at the Kori 1 site, the simulation model can be further developed to include actual site conditions and data for radionuclide contamination.

This paper includes a literature review of remediation planning, soil remediation technology, and the application of discrete event simulation for nuclear-related industrial process operations. Selection of the appropriate technology and a conceptual process model based on soil washing is presented. A discrete event simulation model was developed and verified.

2. Literature Review

International and Korean domestic experience in remediation planning, applicable technologies, and the use of discrete event simulation for remediation projects was reviewed.

2.1. Planning for Remediation. The International Atomic Energy Agency (IAEA) defined soil remediation as an iterative process that includes identification of contaminants, spatial distribution, appropriate decontamination technology, performing remediation, verification of effectiveness, and postremediation monitoring. IAEA recommended that plans for decommissioning and remediation should consider the interfaces and interactions between both processes to improve effectiveness and efficiency and reduce overall costs. The IAEA process for site remediation is shown in Figure 1. The figure depicts an iterative decision process for selecting the appropriate technology. IAEA recommended that decision tools such as simulation modeling, multicriteria decision analysis, and risk assessment be used to select the remediation technology [1].

The OECD Nuclear Energy Agency (NEA) defines remediation as a six-phase process as shown in Figure 2 [3]. The phases are defined as follows:

(i) Phase 1: problem identification

(ii) Phase 2: remedial investigation (assessment and characterization)

(iii) Phase 3: remedy planning (alternative evaluation and selection)

(iv) Phase 4: remedial action (implementation)

(v) Phase 5: project closeout

(vi) Phase 6: institutional control

The Nuclear Energy Agency (NEA) recommended the development of a conceptual site model (CSM) as the as part of an overall site remediation process as shown in Figure 2. The CSM is based on characterization data including site geology, soil classification, and contaminant type, concentration, and spatial distribution. The CSM is used to guide remediation planning and implementation [3].

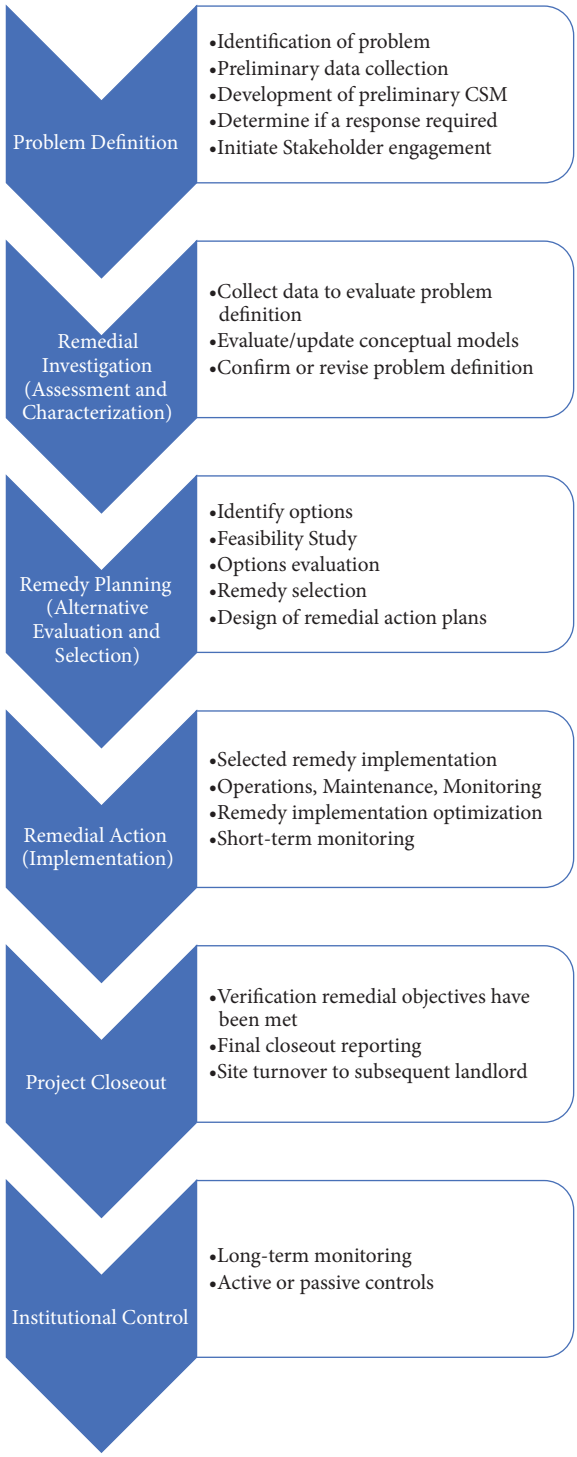

Figure 2: NEA nuclear site remediation phases [3].

The Electric Power Research Institute (EPRI) summarized the experience in US decommissioning and site remediation projects. EPRI found that contamination below structures was difficult to identify and characterize until after the structures are removed in the decommissioning phase. Therefore, site characterization must be an iterative process performed throughout a decommissioning project [4].

2.2. Soil Remediation Technologies. The US EPA issued the *Technology Reference Guide for Radioactively Contaminated Media* that summarized technologies for the remediation of radioactive contamination in soil and groundwater. The guide focused on existing technologies rather than experimental approaches [5].

The guide identified solvent extraction (Figure 3) as an established ex situ technology to remove radionuclides from soils to reduce the volume of nuclear waste or reduce its classification. Solvent extraction has been widely used in the nuclear industry, for example, in conventional uranium milling operations. Solvent extraction, when used for soil remediation, is operated as a batch process to remove the radionuclides. The solvent containing the contaminants is then volume reduced for disposal.

Other methods can be used in combination with solvent extraction. These include physical separation and water washing [5].

Physical separation is an established technology for removing radionuclides from soil. Radionuclides preferentially adsorb soil fines (silts and clays) as opposed to the course fraction (sand and gravel). Thus, the fine-grained soils tend to capture the radionuclides, and physically separating the fine and course fractions is the basis for decontamination. The simplest physical separation method is dry separation that uses sieving with successively finer screens to separate the fines from course fraction. This method concentrates the contaminated soil and reduces the volume of soil for treatment or disposal [5].

A more complex dry separation method, the segmented gate system, uses radiation detectors to improve the separation factor for some radionuclides (Figure 4). This method effectively treats soils contaminated with gamma emitting radionuclides. This method is normally only used for soil contaminated with no more than two radionuclides with different gamma energies [5].

Soil washing is an established technology that is often used in combination with dry separation. Soil washing is an ex situ process using water and surfactants to remove radionuclides from soil. Soil washing can reduce bulk soil or minimize the waste by selectively removing fine-grained particles (silts and clays), which contain most of the contamination, from the bulk soil. It is possible based on the principle that contaminants are generally bound more tightly to the fine-grained particles and not to the larger course grained.

The contaminated wash solution can be volume reduced for disposal. Soil washing is more effective for soils containing less than 25% fines and more than 50% course material. Effectiveness diminishes for soils with more than 10% total organics. Soil washing has been used to treat soil contaminated with radionuclides including plutonium, radium, uranium, thorium, technetium, strontium, and cesium [5]. A process flow diagram of the soil washing process is shown in Figure 5.

The electrokinetic remediation (ER) process has been used to remove radionuclides from low permeability soil. The ER process is an emerging in situ or ex situ soil remediation technology that can separate radionuclides from soil, sludge, and sediment (Figure 6). ER removes metals and organic

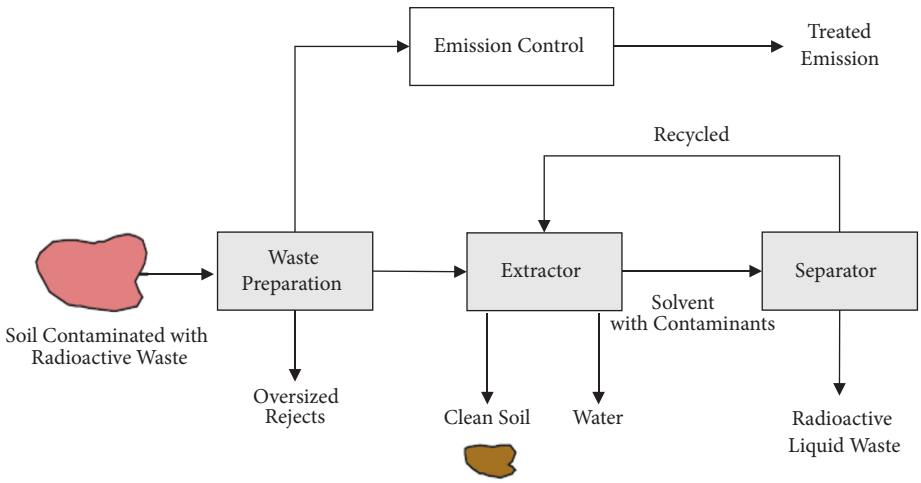

Figure 3: Solvent extraction.

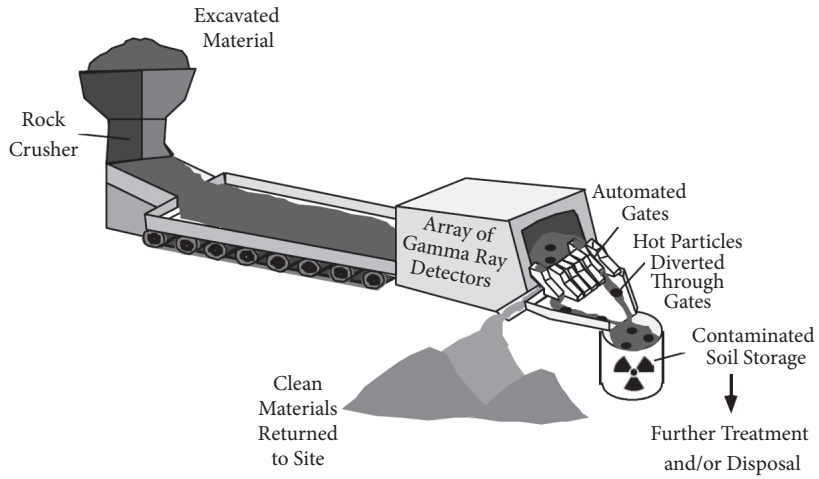

Figure 4: Segmented gate dry soil separation [5].

contaminants from low permeability soil. ER uses electrochemical and electrokinetic processes to desorb, and then remove, metals and polar organics. In situ ER is performed by applying low voltage direct current across electrode pairs that are implanted in the ground containing contaminated soil. The current carries ions and charged compounds to the electrodes. The negatively charged contaminants move to the cathode and the positively charged anions move to the anode.

The Korean Atomic Energy Research Institute (KAERI) has developed an ex situ electrochemical method using soil washing, electrokinetic separation, and waste solution treatment for soils contaminated with radionuclides. This method has been tested successfully at the bench scale [10].

Electrokinetic technology has been demonstrated at the pilot scale and at full scale at several US sites. Geokinetics International Inc. has demonstrated an in situ electrokinetic remediation process at five sites in Europe [11].

2.3. Discrete Event Simulation for Soil Remediation. Simulation models are an abstraction of the real system that represent the key characteristics and features of a specific system or process. Simulation models may be discrete or continuous.

Discrete event simulation (DES) uses a transaction-based approach to model the dynamic behavior of a system. In discrete event simulation state changes occur only at discrete times as opposed to continuous simulations in which the state variables change continuously. DES is an appropriate tool for modeling batch processing systems [12].

Heilala et al. discussed the use of DES as a system analysis tool to evaluate production system concepts, system configuration, and control logic. Simulation models provide the ability to evaluate the throughput of a system, identify bottlenecks, and answer "what-if" questions about proposed changes to the system. Process of optimization requires decisions to be made in a comprehensive way, including budget, schedules, and possible resources such as engineers and technologies. Figure 7 shows the potential for using simulation in the planning phase [7].

Dottavio et al. have demonstrated the application of DES for nuclear power plant decommissioning, site remediation, and nuclear waste management. Nuclear waste flows for a

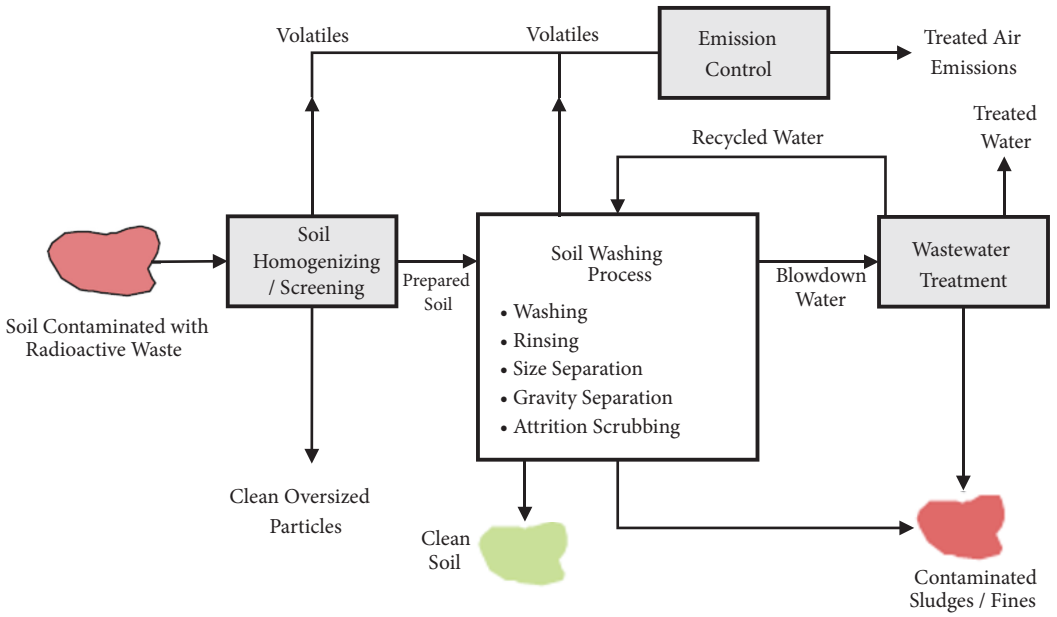

Figure 5: Soil washing process [5].

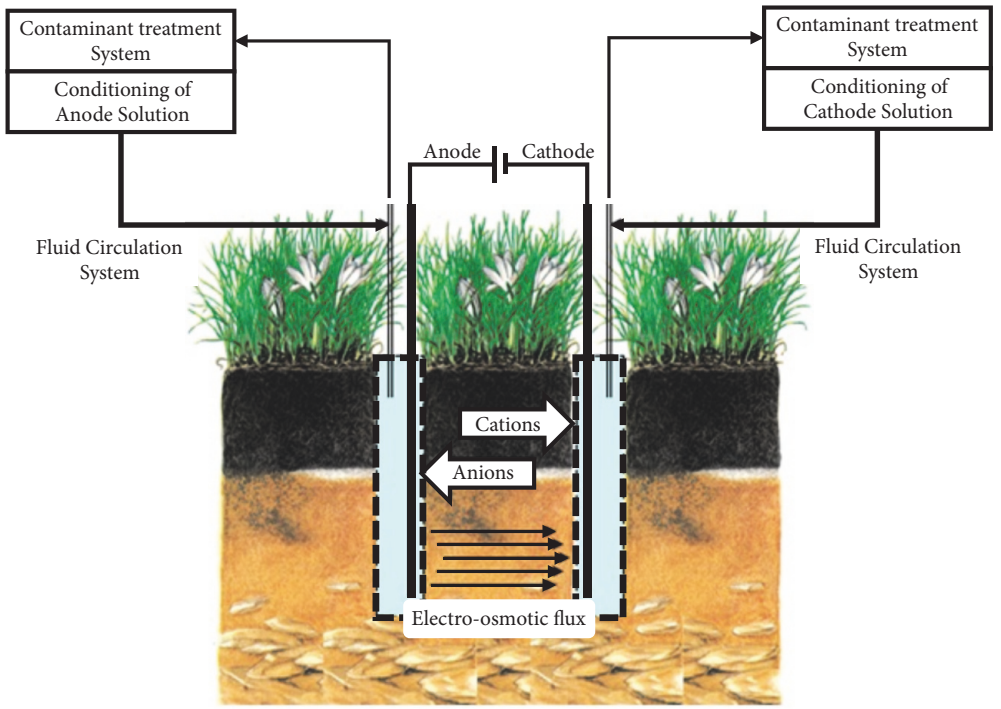

Figure 6: Electrokinetic remediation [6].

typical decommissioning process were modeled using the FlexSim software application. The purpose was to identify and evaluate improvements in process performance. The authors identified process rate limiting steps and other key performance parameters [13].

DES models have been used by the Sellafield Operational Research Group in number of varied nuclear waste management applications and as an overall project planning tool in decommissioning [14].

Worker radiation dose modeling has been integrated with DES models by both Los Alamos National Laboratory and the Sellafield Operational Research Group [14, 15].

3. Selection of Soil Remediation Technology

As shown in Figures 1 and 2, the soil treatment technology alternatives must first be identified and evaluated based on site-specific objectives and criteria. In general,

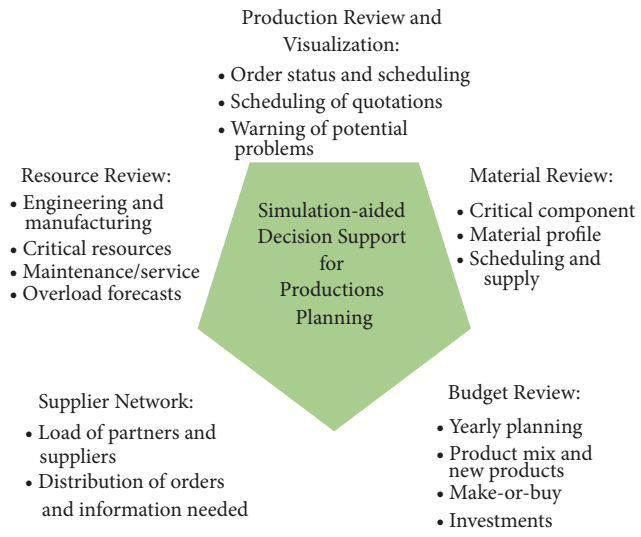

Figure 7: Potential use of simulation-aided decision support for production planning [7].

the site-specific objectives should consider (i) current or future site use, (ii) availability, appropriateness, and cost of remediation technologies, (iii) budget and timeframe, and (iv) regulatory requirements. Site investigation and characterization should be performed to determine the type and distribution of radioactive contamination. Finally, the alternative technologies should be evaluated against the technical, regulatory, and economic criteria to select the preferred alternative.

The remediation options considered in this study are solvent extraction, dry soil separation, soil washing, electrokinetic remediation, and the KAERI combined soil washing and electrokinetic separation process. The combination of dry soil separation and soil washing (hereafter referred to as soil washing) was determined to be the most appropriate technology to demonstrate the use of DES for soil remediation for Korean nuclear power plant sites.

There are several reasons for selecting a soil washing technology at the conceptual stage in developing the DES model for this study. First, the soil washing process is relatively simple and is based on the physical properties of soils. It excludes the consideration of chemical and electrical properties of contaminated soils. Second, soil washing has been used extensively in commercial applications and is easily modified to remove various radionuclides from soils. And third, the waste water from soil washing is less difficult to manage than the solvents in an extraction process. Finally, the soil washing process has a model structure similar to the KAERI ex situ electrochemical method which we think is a viable option, and a simple soil washing model could be modified to use the KAERI methodology in future applications. Soil washing is, therefore, a good technical basis for the simulation model.

4. Soil Remediation Process

4.1. Principles. Soil washing is a repetitive batch process that is time-consuming and has considerable uncertainty due to the lack of Korean domestic experience. It is based on the principle that contaminants are generally bound more tightly to the fine-grained particles and not to the larger course grained soil. Because of this, data for the particle size distribution of the soil at the remediation site is needed to model the soil washing process. Figure 8 shows the radioactivity concentration according to the soil particle size near a Korean nuclear facility. The figure shows the inverse relationship between particle size and radioactivity [8].

The soil washing process uses dry soil sieving in the first stage to separate the fine and course fractions prior to water washing. This reduces the contaminated soil volume prior to the washing stage potentially reducing secondary waste generation. Soil washing must be used with other treatments, such as precipitation, filtration, and/or ion exchange. Through this multistage process, the contaminated residuals (fine particles and washing solution) are treated and volume reduced for disposal. The cleaned soil that meets regulatory clearance requirements could be returned to the site and reused as backfill.

4.2. Operational Procedure. Soil washing systems normally use a six-step process [9]:

(1) Pretreatment: large size material such as rubble is removed, or optionally crushed, and scrubbed if necessary.

(2) Separation: course and fine grain soils are separated.

(3) Coarse-grained treatment: the remaining fine grain material is separated

(4) Fine-grained treatment: silt is separated from clay.

(5) Process water treatment: process water is recycled or treated for disposal.

(6) Residuals management: remediated soil can be recycled as backfill at the nuclear site. Fines and sludge are contaminated and must be managed as radioactive waste.

Soil washing processes range from relatively simple methods with several particle separation processes to complex methods including several additional processes such as magnetic or chemical treatments. However, simple soil washing processes are commonly used in the most soil washing systems and they generally remove fine fractions from the bulk soil. Simple designs have a combination of screening, classification and solids dewatering. The typical equipment used for most soil washing processes is summarized in Table 1 [2].

After the completion of soil separation according to its particle sizes using equipment listed in Table 1, additional equipment should be considered for treatment of concentrated residue and process water. In order to discharge the concentrated residue from soil washing system, the clay is subjected to dewatering process through press filter equipment. For the treatment of process water which is essential in physical separation processes, ion exchangers can be used. Water is continuously consumed during the operation, so make-up water is supplied and used process water is recycled in the system during operation [2].

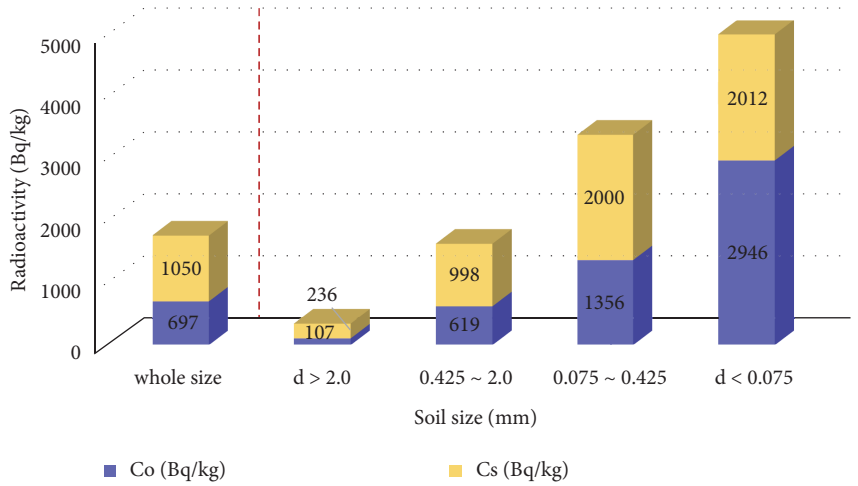

Figure 8: Radioactivity concentration versus particle size [8].

Table 1: Typical soil washing equipment [2].

Exploitable Soil	Process Equipment
Size	Vibratory Screens (sieves)
	Sieve Bends
	Trommel (rotary) Screens
Hydraulic Size (settling Velocity)	Classifiers
	Hydrosizers
	Hydrocyclones
Specific Gravity	Jigs
	Sluices
	Dense Media Separators
	Spirals
	Shaking Tables
Surface Chemistry	Froth Flotation Systems

5. FlexSim Simulation Model

5.1. Process Model. The soil washing process has two main objectives. These are to reduce the volume of waste through separation by particle size and to properly manage the concentrated residues. The process in the diagram (Figure 9) is a relatively simple abstraction that contains only elements that are essential to meet the two main objectives.

The first step in developing the simulation model is to visualize the target system through schematization. The simplified soil washing system is expressed in Figure 9 as a process flow block diagram.

Each block represents the equipment used in the soil washing process and the work being performed in each stage. Black and blue arrows, respectively, indicate the flow of soils and wash water. The black arrow implies process logic such as the distinction and separation of the soil flow according to particle sizes. Soil screening and an attrition scrubber are used for the pretreatment phase; two sand screws, a cyclone, and a filter press, are used for the separation phase. It is assumed that the treatments of coarse- and fine-grained soils, such as rinsing and dewatering, are included in each of the blocks for simplification of the model. Wash water is injected to each block for separation and circulated through a water treatment system. Additional water must be injected to compensate for water lost with the cleaned soil. Finally, the treated sludge/residue must be managed as radioactive waste.

5.2. FlexSim Model Development Approach. A simulation model of the soil washing process was developed using FlexSim, a discrete event simulation modeling application that is widely used in industries such as material handling, manufacturing, logistics, transportation, and mining [16]. In this study, a simple process model representing a soil remediation plant was developed to demonstrate the use of simulation for planning a soil remediation process.

To be effective, simulation development should use a systematic approach. In this study, development of the simulation used the following approach [7]:

(i) Project definition
(ii) Process mapping (static diagram)
(iii) Simulation model (dynamic)
(iv) Verification
(v) Simulation of cases for study
(vi) Findings, conclusions, and recommendations

5.3. FlexSim Model Assumptions. The simulation model has several simplifying assumptions as follows:

(i) Fifteen tons of soil can be treated per a batch. The system has 240 tons/day processing capacity under 8-hour operation a day.
(ii) There is no need for warming-up between the idle state and steady state. In the simulation, the system equipment enters the steady state immediately with the beginning of operation.
(iii) Due to lack of detailed commercial data except for general information about overseas experience,

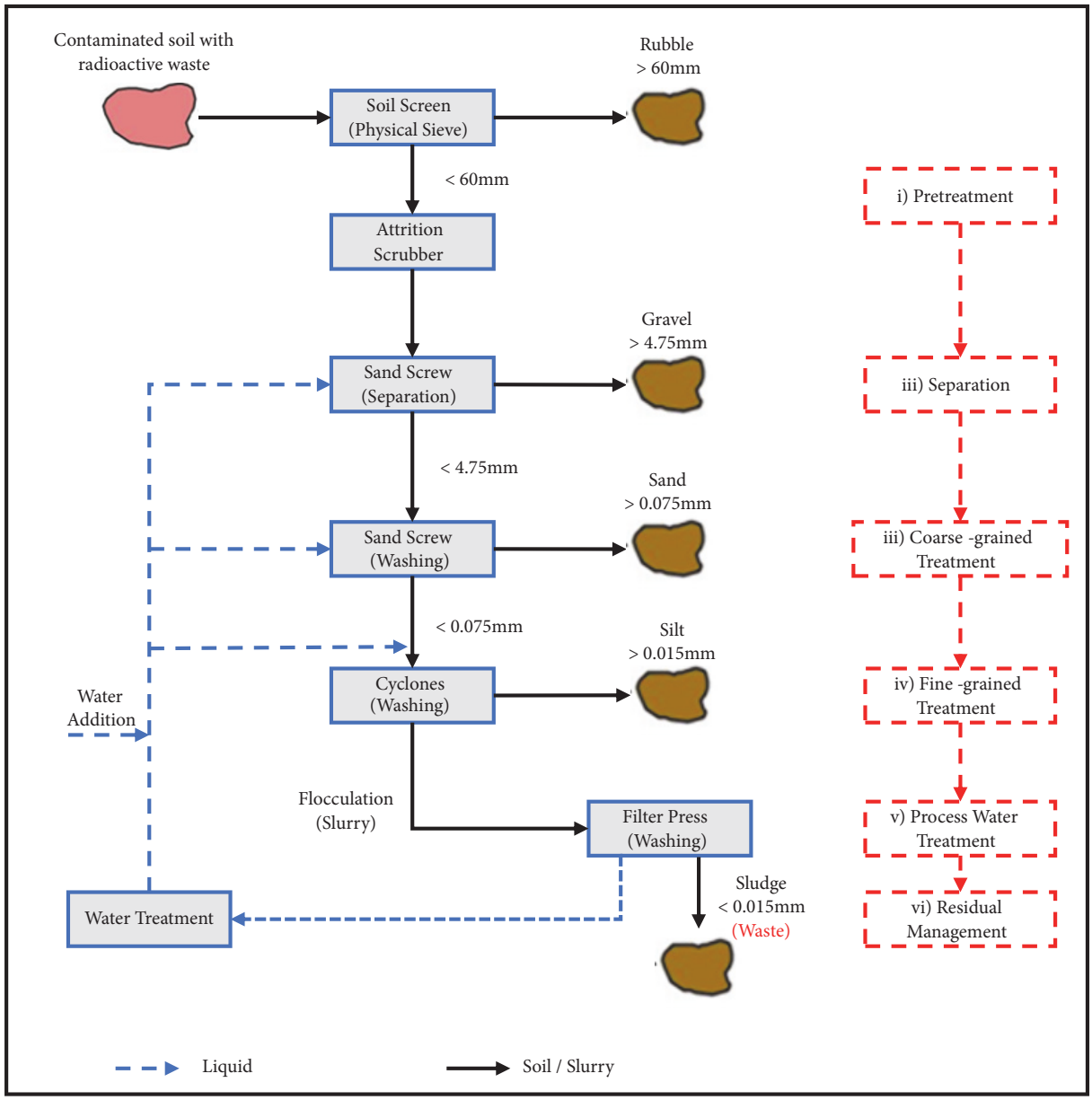

Figure 9: Soil washing process model [9].

assumptions are applied to the process rate and capacity for system components and the overall process.

(iv) The system has enough capacity to operate without bottlenecks.

(v) There are no unplanned shutdowns due equipment failure or maintenance activities.

In the development of the simulation model, among various resources and functions of FlexSim, four basic objects were used to visualize the soil remediation process. Those objects are sources, queues, processors, and sinks and are defined as follows [16].

Source. The source creates flow items and releases them to a downstream object. The simulation user can control the rate at various nodes at which the source creates flow items so that they arrive on a fixed schedule, a regular continuous rate, or a random statistical distribution. In the reference model, a fixed (scheduled) arrival scenario simulates the batch process.

Queue. The queue stores flow items until a downstream object is ready to take them. By default, the queue releases flow items on a first-in-first-out basis, but other options are available.

Processor. Processors simulate flow items being processed at a station. Processors simulate a time delay, beginning with a setup time followed by the process time. The user can also require the processor to use an operator during the setup and/or process time. The user can also set processors to handle more than one flow item at a time. In the reference model, constant process times are used.

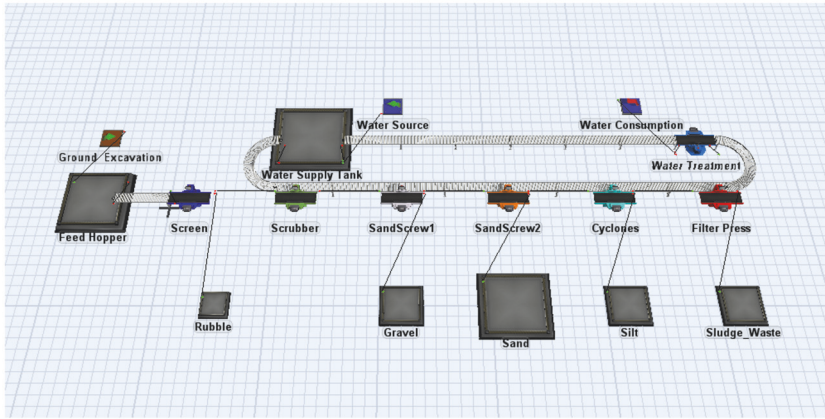

Figure 10: Logistical simulation of soil washing process.

Sink. The sink removes flow items from a simulation model when the items passed the final process.

In the simulation model the key elements control the movement of contaminated media (soil and wash water) as operational characteristics of the system. The target media are generated from the sources then transferred and separated according to the intended logic in the simulation.

5.4. System Layout. The soil washing process is visualized in the simulation model using FlexSim software based on the process flow block diagram as shown in Figure 10. The simulation was constructed by creating objects and connecting them according to the flow of soil within the soil washing system.

Figure 10 shows a screenshot of the soil washing simulation model from the 3D output of the FlexSim model. The excavated soil from the contaminated site is fed to the feed hopper on the left side of the figure, and the soil that has been cleaned through dry separation is sent to each queue according to the grain size, i.e., rubble, gravel, sand, silt, and sludge/clay. While the separation and treatment of soil are proceeding, wash water is circulating within the water circulation system located in the upper part of the figure. Some of the wash water is consumed, because water is contained in cleaned (discharged) soil. To compensate for water loss, make-up water is injected to the water supply tank.

5.5. Simulation Logic. Once the physical structure of the simulation model is set, the next step is to create the logic that determines how the soil and water flows into and through the simulation model. In the soil washing process, each equipment element is designed to separate soils according to their particle size.

5.6. Flow of Soils. In the simulation model, the processor objects are used to represent the components in the soil washing process. First, variables are designated as the soil "item" according to the attributes of each unit soil that will enter the system. Then each processor located downstream classifies and cleans the soil based on the input variables. For example, "Sandscrew2" (Figure 10) classifies sand particles with a value "3" for the "item.type" variable and sends them to the "queue" and sends soil particles other than sands to the next element, "processor: cyclones".

The particle size distribution of the soil excavated at the site must be determined. Preliminary soil particle size distribution data obtained from soil samples around the perimeter of the Kori site by KAERI was used to obtain a more realistic as it is the best available preliminary data [2]. Table 2 lists the raw soil data, the soil excavation/cleanup rates, and the derived input data.

The input data in Table 2 were derived from the raw data through simple processing. The input data were developed by averaging the numerical values for particle size distribution obtained from 10 samples around the Kori NPP site. A value of 1% for the rubble (>60mm) was assumed. Because the main concern in the washing process is silt and clay, this assumption does not impact the results. The composition of the silt and clay in the input data column was obtained from 10 samples by estimating the values from the standard soil texture diagram [17]. Once the soil particle size distribution is input, the "source" object generates the soil "items" probabilistically according to the distribution of the input and provides the soil particles to the system.

The excavation rate to feed soil to the system and the cleanup rate to remediate the soil were also assumed. On a commercial scale, there were large nonnuclear projects with a throughput of 20-100 tons/hour [5]. In this study, the system capacity was assumed to be 240 tons/day (30 tons/hour for 8 hours a day). The faster processing speed as compared to excavation speed is an intentional assumption to avoid bottlenecks in the system.

5.7. Flow of Wash Water. In the model, the wash water system was schematized but not integrated with the soil treatment system. This was simplifying assumption and for their integration additional "processors" for combining and separating soil and water will be needed at junction points such as scrubbers, screws, cyclones, and filter presses.

As soils are cleaned by soil washing, the soil moisture content increases. The moisture content of the soil is the ratio of the weight of the water in the soil. In this simulation,

Table 2: Soil input data for the model [2].

Parameters	Raw Data		Input Data	
	Type	Value	Type	Value
Excavation Rate	-	-	-	30.0 tons/hr
Particle Size of Soil	Gravel (>4.75mm)	6.3%	Rubble (>60mm)	1.0%
			Gravel (60~4.75mm)	5.3%
	Sand(4.75~0.075mm)	83.4%	Sand (4.75~0.075mm)	83.4%
	Silt & Clay(<0.075mm)	10.3%	Silt (0.075~0.015mm)	3.9%
			Clay (<0.015mm)	6.4%
Cleanup Process Rate	-	-	-	36.0 tons/hr

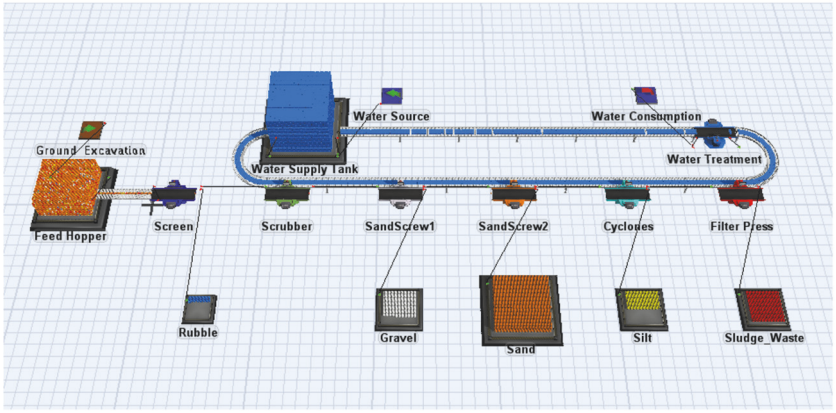

Figure 11: Logistical simulation model operation.

increase of soil moisture content is assumed as 10%. That means that 3 tons of water is consumed per batch and 3 tons of make-up water is supplied to the water supply tank. Recycling of wash from dewatering during the process could be included in future revisions of the model.

5.8. Verification. Verification was performed to assure that the simulation was working as intended.

In this study, the simulation model was verified by checking the output of the simulation. In the simulation, we can observe the visualized soil washing process and the waste throughput. Once the simulation starts, 30 tons of soil per hour is supplied to the feed hopper and the soil washing system operates at 36 tons per hour. Due to difference between the soil excavation rate and process rate, this system can be maintained as a 1-hour batch process.

The object for comparison is the particle size distribution that was input into the "source" object. Figure 11 shows a screenshot during operation of simulation. In the feed hopper on the left of the figure, soil particles in different colors are mixed randomly according to the probabilistic input data for soil particle size distribution. They are separated and treated by "processors" according to their values in "item.type" variable. As a result of simulation, separated and cleaned soils are stacked in the "queues".

Table 3 shows the process results after 2 hours of operation. The results show that the process output is approximately equal to the input meaning the simulation is operating correctly according to the intended logic. The model generates detailed processing data as a numerical table or graphical chart as shown in Figure 12.

The system is shown to be operating in a batch process as seen in Figure 12 which shows that the soil in the feed hopper accumulates and is emptied repeatedly. The State Pie diagram in Figure 12 shows utilization of the system equipment elements.

6. Discussion

The purpose of this report is to suggest that the decommissioning and site remediation projects can be optimized and improved by applying simulations to the soil remediation planning. In this section we discuss the application of simulation to the soil remediation planning.

In a soil washing system batch or continuous operation has advantages and disadvantages. In this study, the simulation model used the batch process condition by controlling the excavation rate and cleanup rate. The difference between the batch and the continuous is not significant in system operation. However, due to radioactive waste management regulatory requirements may be necessary to process the soils in batches based on site characterization and waste classification. Batch operation can avoid the regulatory issues related to blending radioactive wastes with different classifications.

Bottlenecks are a major concern in terms of efficient operation of the system. Looking at the "State Pie" in Figure 12, cyclones and filter presses at the downstream are relatively free because the idle state is dominant, while

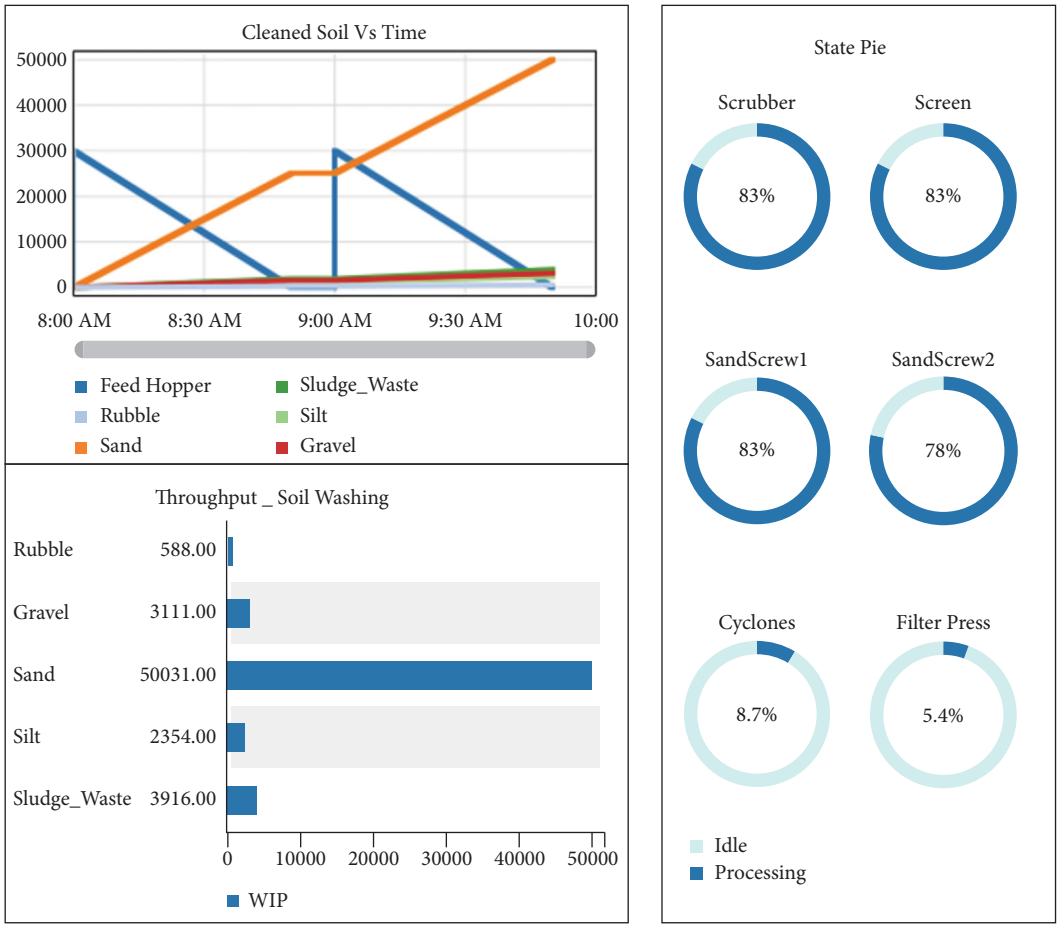

Figure 12: Graphical report for soil washing (at 2 hours).

Table 3: Simulation results at 2 hours of operation.

Queue	Rubble	Gravel	Sand	Silt	Sludge	Total
Processed Soil (ton)	0.588	3.111	50.031	2.354	3.916	60.000
Ratio (%)	0.98%	5.19%	83.39%	3.92%	6.53%	100.00%
Input Data (%)	1.0%	5.3%	83.4%	3.9%	6.4%	100.00%
Error (%)	-2.00%	-2.08%	-0.01%	0.51%	2.03%	-

four upstream devices have very high utilization. This means that the upstream devices are relatively overloaded and the downstream devices are relatively overdesigned.

One way to prevent bottlenecks is to increase the device's capacity, but in terms of system maintenance and reliability, it may be better to distribute the flow into parallel devices rather than a single larger device. This preliminary simulation model does not include the failure of the equipment or the downtime due to maintenance; however a more detailed simulation model will be able to evaluate system component failure and scheduled downtime.

Figure 13 depicts a soil remediation and waste management system. In this study we have modeled the soil washing process (Module 2). Module 1 represents soil excavation module in which excavated soil from the contaminated site is transferred to a soil treatment system to clean the soil. In Module 3, the waste management system is shown downstream from the soil remediation process. For future development of this model, we should develop Module 1 and Module 3.

Process optimization requires making decisions in a comprehensive way, including cost, schedule, and resources such as personnel and equipment. Figure 7 shows the potential for using simulation in the planning phase [13]. We can view the soil remediation system as a production system with nuclear waste as the product. As we further develop our soil remediation simulation model, we should include more detail that will allow a holistic evaluation of the waste production system.

7. Conclusions

In this study, we investigated the applicability of discrete event simulation for a soil washing process for planning

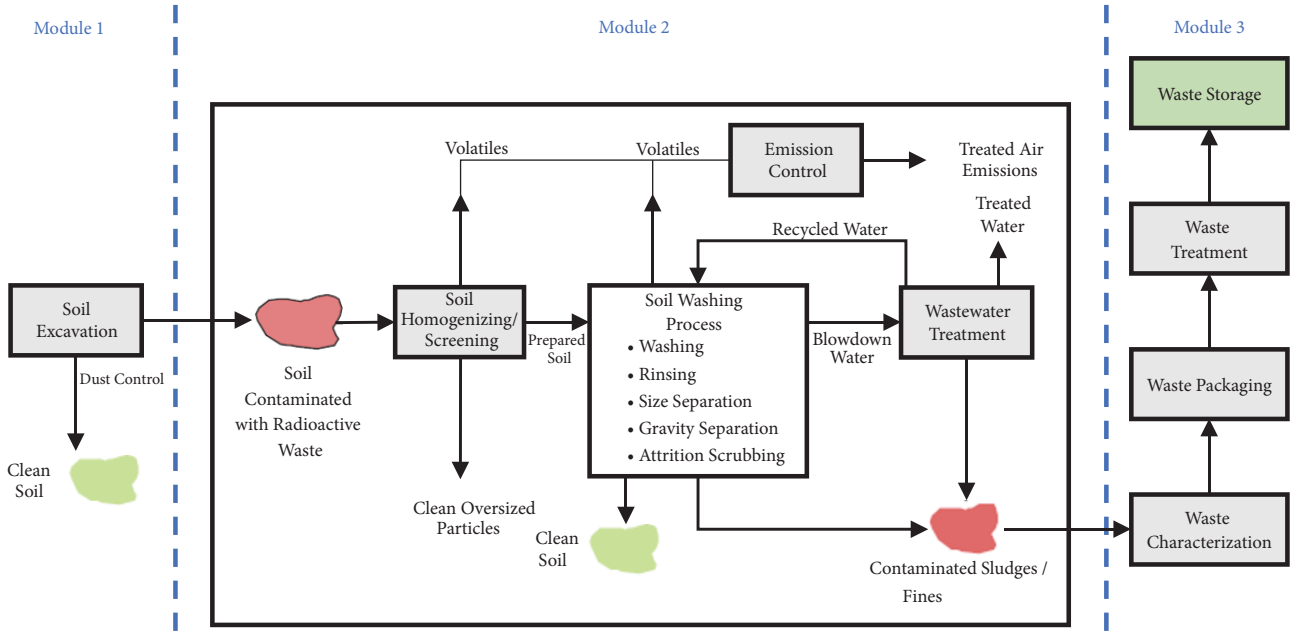

Figure 13: Expanded soil remediation process model.

site remediation. It was shown that a batch process such as soil washing can be effectively modeled as a discrete event process. Based on the literature review, efficient allocation of resources and efficient waste management including volume reduction can be achieved by use of the model for planning the soil remediation process.

Furthermore, we suggest extending the scope of the simulation model. The scope could extend beyond soil remediation to include the entire site remediation process from site excavation to waste management. This suggests that the simulation model can be used as a tool for decision analysis and planning of nuclear power plant decommissioning and remediation projects.

In future work, a conceptual site model (CSM) as suggested by NEA (Figure 2) should be developed to define the site-specific problems to be solved by remediation. Site characterization data should be incorporated in the CSM when such data becomes available for Kori 1. At that time, a more detailed simulation model can be developed to include site soil properties, radionuclides of interest, and a specific soil washing process. More broadly, site remediation starts with a site investigation and development of the site conceptual model and shows possibilities for the integration of excavation, soil treatment, waste characterization, packaging, storage, and worker dose exposure assessment.

Data Availability

The data used to support the findings of this study are included within the article.

Conflicts of Interest

The authors declare that they have no conflicts of interest.

Acknowledgments

This research was supported by the Nuclear Safety Research Program through the Korea Foundation of Nuclear Safety (KOFONS) and granted financial resource from the Nuclear Safety and Security Commission (NSSC), Republic of Korea (no. 1605008).

References

[1] International Atomic Energy Agency, *Integrated Approach to Planning the Remediation of Sites Undergoing Decommissioning*, IAEA, Vienna, Austria, 2009.

[2] B. Seo, I. Kim, J. Nam et al., *Development of Decommissioning, Decontamination and Remediation Technology for Nuclear Facilities Development of Site Remediation Technology for Decommissioning and Contaminated Site*, Korea Atomic Energy Research Institute, KAERI/RR-4233/2016, 2017.

[3] Nuclear Energy Agency, *Nuclear Site Remediation and Restoration during Decommissioning of Nuclear Installations*, OECD Publishing, NEA No. 7192, 2014.

[4] Electric Power Research Institute, *Power Reactor Decommissioning Experience*, Palo Alto, Calif, USA, 2008.

[5] U.S. Environmental Protection Agency, *Technology Reference Guide for Radioactively Contaminated Media*, 2007.

[6] C. Cameselle, S. Gouveia, D. E. Akretche, and B. Belhadj, "Advances in electrokinetic remediation for the removal of organic contaminants in soils," *Organic Pollutants - Monitoring, Risk and Treatment*, 2013.

[7] J. Heilala, J. Montonen, P. Jarvinen et al., "Developing simulation-based Decision Support Systems for customer-driven manufacturing operation planning," in *Proceedings of the 2010 Winter Simulation Conference - (WSC 2010)*, pp. 3363–3375, Baltimore, MD, USA, 2010.

[8] G.-N. Kim, S.-S. Lee, D.-B. Shon, K.-W. Lee, and U.-S. Chung, "Development of pilot-scale electrokinetic remediation technology to remove 60Co and 137Cs from soil," *Journal of Industrial and Engineering Chemistry*, vol. 16, no. 6, pp. 986–991, 2010.

[9] U.S. Environmental Protection Agency, *Soil Washing/Soil Flushing Volume 3*, U.S. Environmental Protection Agency, EPA 542-B-93-012, 1993.

[10] G.-N. Kim, S.-S. Kim, and J.-W. Choi, "Removal of 137cs from contaminated soil using pilot electrokinetic decontamination equipment," *International Journal of Environmental and Agriculture Research*, vol. 3, no. 1, p. 7, 2017.

[11] *Electrokinetic Separation*, The Federal Remediation Technology Roundtable (FRTR), 2018, https://frtr.gov/matrix2/section4/4-4.html.

[12] C. W. Alexander, "Discrete event simulation for batch processing," in *Proceedings of the 2006 Winter Simulation Conference*, pp. 1929–1934, Monterey, Calif, USA, 2006.

[13] G. Dottavio, M. F. Andrade, F. Renard, and V. Cheutet, "Logistical optimization of nuclear waste flows during decommissioning," *International Journal of Environmental Ecological and Engineering*, vol. 10, no. 10, p. 6, 2016.

[14] R. Thompson and S. McCann, "The application of simulation modeling in nuclear decommissioning," in *Proceedings of the WM2010 Conference*, p. 7, AZ, Tucson, USA, 2010.

[15] G. H. Tompkins, D. E. Kornreich, R. Y. Parker, A. C. Koehler, J. M. Gonzales-Lujan, and R. J. Burnside, "Dynamic radiation dose visualization in discrete-event nuclear facility simulation models," in *Proceedings of the 2004 Winter Simulation Conference*, pp. 472–478, Washington, DC, USA, December 2004.

[16] *FlexSim User Manual*, Flexsim Software Products, Inc., 2017.

[17] "Soil Texture Calculator — NRCS Soils," https://www.nrcs.usda.gov/wps/portal/nrcs/detail/soils/survey/?cid=nrcs142p2_054167.

Hindawi
Science and Technology of Nuclear Installations
Volume 2019, Article ID 8736173, 8 pages
https://doi.org/10.1155/2019/8736173

Research Article

Assessment of the Radioactive Contamination of the RBMK-1500 Reactor's Steam Pipelines and High Pressure Rings

G. Poškas, P. Poškas, and A. Šimonis

Lithuanian Energy Institute, Nuclear Engineering Laboratory, Breslaujos G. 3, Kaunas LT-44403, Lithuania

Correspondence should be addressed to G. Poškas; g.poskas@gmail.com

Received 23 October 2018; Accepted 7 February 2019; Published 3 March 2019

Guest Editor: Dimitrios Tsaoulidis

Data analyses of radioactive contamination of the RBMK-1500 reactor's steam pipelines (SP) and components of high pressure rings (HPR) are presented in this paper. Also, modelled results of the SP-HPR system are compared to the results of other RBMK-1500 systems at Ignalina NPP Unit 1. Characteristics of SP-HPR components, thermal-hydraulic conditions of the coolant, and system operational regimes were evaluated employing the computer code LLWAA-DECOM (Tractebel Energy Engineering, Belgium). The presented results complement radiological characterization activities and facilitate the decommissioning process of nuclear facilities with RBMK type reactors. Analysis of the modelled results showed that the spread of radioactive contamination is very uneven between different components of the SP-HPR. The overall activity level of deposits of the SP-HPR is mostly determined by activated corrosion products and is lower than the activity level in the main circulation circuit (MCC) and nonpurified water subsystem activity of the purification and cooling system (PCS).

1. Introduction

The Ignalina NPP is the only nuclear power plant in Lithuania which was operating two Russian design RBMK-1500 type reactors. Unit 1 was commissioned in 1983 and Unit 2 in 1987. The original design lifetime was projected for up to 30 years; however, Unit 1 was shut down at the end of 2004 and Unit 2 at the end of 2009. At the moment, both units are under decommissioning. Such kind of reactors and their technological systems are under decommissioning for the first time in the world. Therefore, there is a lack of knowledge about the radioactive contamination of such kind of systems, especially about radionuclides important to decommissioning and disposal. Moreover, it is worldwide recognized that the radiological characterization is one of the key issues then planning for decommissioning of NPPs. Thorough radiological characterization ensures that proper safety measures are used to reduce personnel exposure, minimization of radioactive waste and optimal utilization of disposal facilities and also minimization of costs [1, 2].

Surface contamination of the systems' components with radioactive substances is a result of the contaminated coolant circulating within these systems. There are two mechanisms for the coolant in technological systems to be contaminated with radioactive substances: contamination by activated corrosion products and contamination by fission products and actinides [3].

Despite design and operational measures developed to reduce corrosion of the technological systems, corrosion products are released in kilogramme quantities per year into most water-cooled reactor circuits [4]. Corrosion rate is dependent on many factors, such as materials of components, coolant chemistry, flow regime, and temperature [5]. Corrosion products can be divided into soluble and particulate types and are involved in different transfer mechanisms between the coolant and the surface of systems' components [6]. Corrosion products are moved to the reactor core with the coolant and activated by neutron flux. This neutron activation is possible for both ions and particles. Activated corrosion products flow with the coolant to the reactor systems which are located outside of the core, where they deposit on the surfaces of the components and cause their surface contamination. The components located in the core corrode as well, and due to erosion, these radioactive particles are also transferred with the passing coolant to the systems located outside of the reactor core [7].

Table 1: Main SP-HPR components.

No.	Name of the component	Marking
1	Steam pipes from drum-separator to steam headers	SP-HPR-1
2	Steam headers	SP-HPR-2
3	Steam pipe between drum-separators	SP-HPR-3
4	Steam pipes to turbine	SP-HPR-4
5	Pipe to high pressure ring	SP-HPR-5
6	High pressure ring	SP-HPR-6
7	Inlet pipes of main steam relief valves and fast acting pressure reducing valve	SP-HPR-7
8	Pipe to steam reception chamber	SP-HPR-8

The fission process produces more than 200 radionuclides, either directly or indirectly by decay chains and in case of claddings defect, these fission products can be released from the fuel rods into the coolant and contaminate the systems outside of the core. Additionally, during manufacturing, the outer surfaces of the fuel rods might be contaminated with uranium oxide which in active zone will also form and release to the coolant fission products as well [8].

2. Steam Pipelines and High Pressure Rings (SP-HPR)

Steam pipelines (SP) and high pressure rings (HPR) ensure the removal of steam from the drum-separators to turbines and to accident localisation system, therefore protecting the main circulation circuit (MCC) against overpressure. The main SP-HPR components are listed in Table 1 and a simplified scheme is shown in Figure 1.

Steam by steam pipes (1) is supplied from two drum-separators to four steam headers (2) for one MCC loop. Steam from the middle of steam headers (2) via four main steam pipes (4) is supplied to the turbine. Steam from headers (2) via four steam pipes (5) is supplied to high pressure rings (6) and then via pipes (8) to the accident localisation system's (ALS) steam intake chambers if overpressure conditions are reached. In each HPR, there are one fast acting reducing device (BRU-B valve) and six main steam relief valves (MSRV) installed.

3. Methodology

There is a number of complicated processes related to radioactive contamination of the systems described above. Therefore, when modelling the whole contamination process, it is necessary to consider such complicated processes as formation of radioactive particles, their deposition on surfaces, erosion of deposits and metal oxides, and transfer of particles by the flowing coolant. To analyse these processes in great detail, it is necessary to use complicated numerical solution models, which require time-consuming calculations even when the computational resources are relatively high. For this reason, in practice simplifications are made by implementing empirical and semi-empirical models in computer codes (PACTOLE [9], CRUDTRAN [10], ACE-II [11], CATE [12], etc.).

Assessment of the radioactive contamination of SP-HPR components listed in Table 1 was done employing LLWAA-DECOM computer code (Tractebel Energy Engineering, Belgium). The code is used to model the activity deposited on the surfaces of the components which is in contact with radioactive liquid or gaseous fluids. The code uses a set of modelling equations to estimate the Brownian diffusion velocity, the particle velocity in the coolant, probabilistic settling of particles, and the nuclides deposition and release rates. Its application is validated for the range of input parameters that is typical for nuclear reactors (turbulent flow of coolant, high Re numbers, appropriate nuclide list, etc.). Moreover, many codes are oriented towards evaluating activity of relatively short-lived nuclides which are important while reactor is still in operation; meanwhile, LLWAA-DECOM is intended for evaluating activity of waste considering decommissioning and disposal. The validation results of this code are presented in [13], where it is demonstrated that there is rather good agreement between the modelled and the measured results of dose rates and the deposits activity.

Specific activity of the deposits on the walls of the system components is described using the following equation [13]:

$$\frac{dW_i}{dt} = K_d * Cv_i * \left(1 - frspr_i\right) - W_i * \left(K_r + \lambda_i\right) \qquad (0)$$

where W_i is specific activity of ith nuclide of deposits, [Bq/m^2]; K_d stands for particle deposition coefficient, [m/s]; Cv_i is specific activity of ith nuclide of the coolant, [Bq/m^3]; $frspr_i$ is soluble part of ith nuclide in the coolant; K_r stands for particle relaxation coefficient, [s^{-1}]; λ_i is decay constant of ith nuclide, [s^{-1}]; t is time.

Particle deposition and erosion ratio is described by complex deposition (K_d) and relaxation coefficients (K_r) for operation cycles of systems. These coefficients on their own are calculated taking into account the following aspects:

(i) particle speed because of Brownian forces and because of coolant flow velocity;

(ii) particle physical properties (diameter, density, and solubility);

(iii) coolant characteristics (temperature, viscosity, Reynolds number, average flow rate, and water pH);

(iv) parameters related to physical characteristics of system's components and operation characteristics of the system itself.

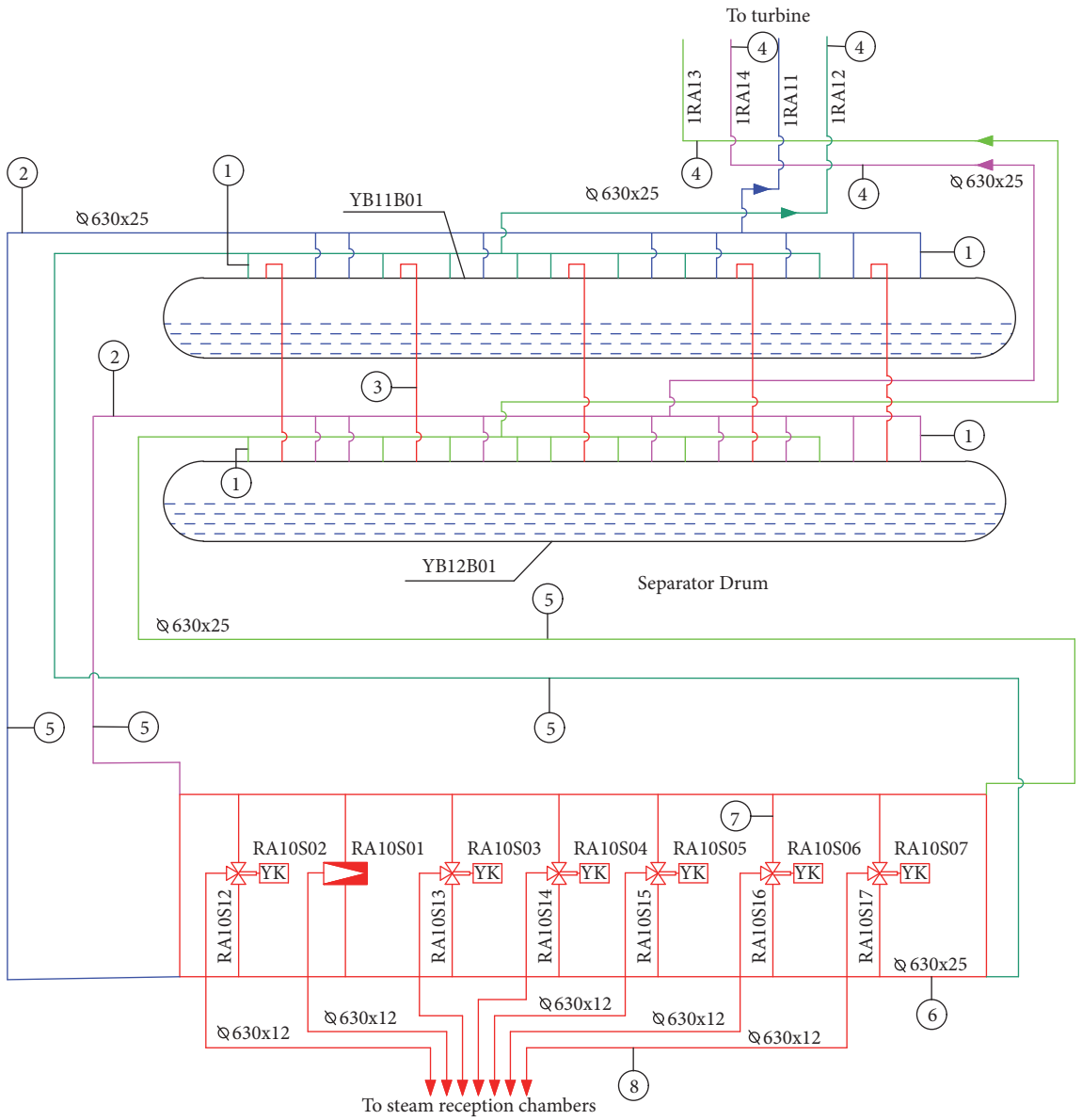

Figure 1: Simplified SP-HPR scheme.

In addition, local sensitivity analysis was performed for components with the highest contamination level to determine parameters that have the highest impact on uncertainty of the modelling results. Additional runs of the model with minimum (-20% of nominal value) and maximum (+20% of nominal value) values of the parameters were necessary to perform such analysis. In total impact of 10 input parameters and volumetric activity of Co-60 and Fe-55 was analysed.

4. Results

Analysis of the modelling results on SP-HPR components' contamination shows (Figure 2) that steam pipes to the turbine (SP-HPR-4) and steam pipes from the drum-separator to headers (SP-HPR-1) with steam headers (SP-HPR-2) are the most contaminated components. The contamination of other components is much lower and comprises less than 1% of the contamination of the most contaminated component (SP-HPR-4).

Such variation in the activity of the deposits on the components is defined by different values of the relevant system operation, geometric, and coolant characteristics in the components of the system. There is no coolant filtration in this system, and therefore the average coolant activity is constant (an assumption that coolant is fully saturated during the operation cycle). The difference in the deposits of the components for the SP-HPR is mostly caused by the differences in coolant velocity. As stated in [18, 19], the particle deposition rate increases as the velocity of the coolant increases. This is related to the intensity of coherent structures near the wall. Turbulent fluctuations of the coolant flow increase, especially the normal component v' of the turbulent

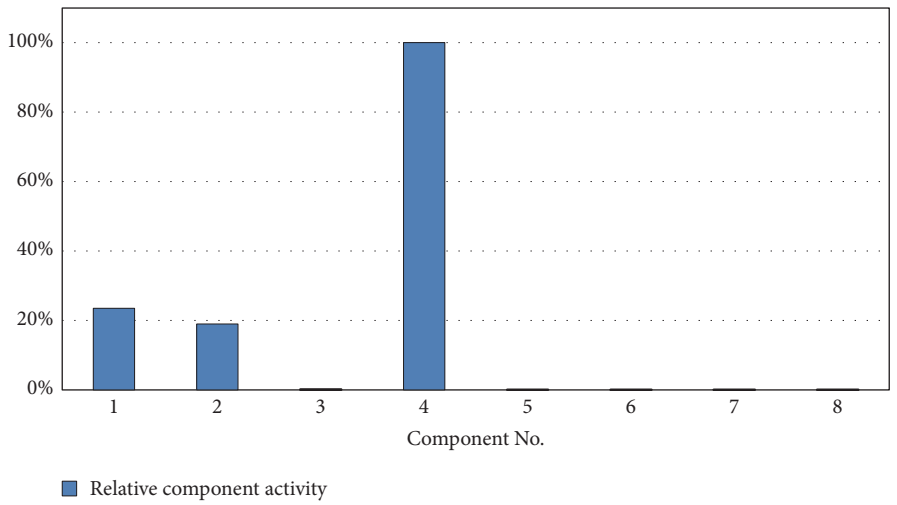

Figure 2: Relative activity of deposits on SP-HPR components (SP-HPR-1:8/SP-HPR-4).

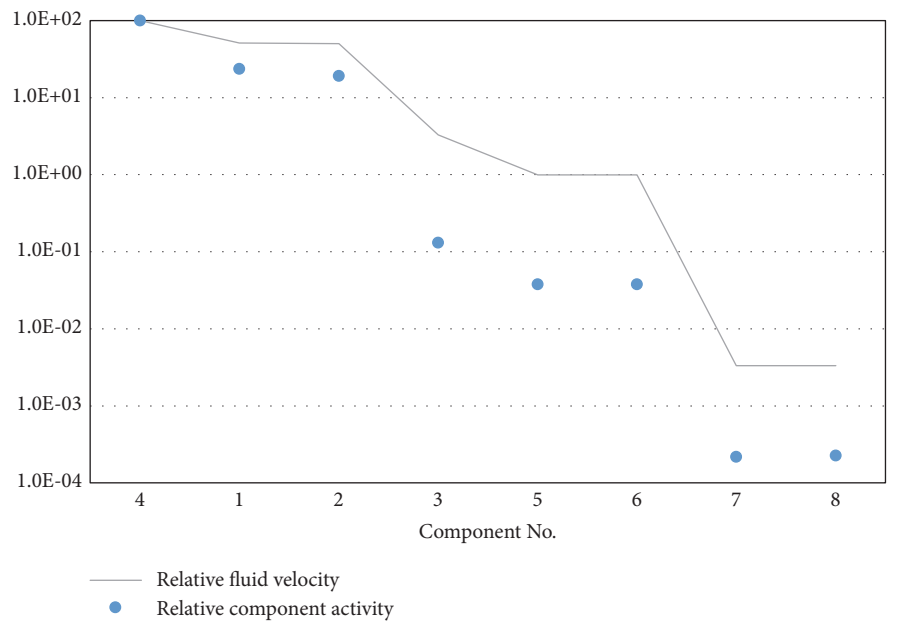

Figure 3: The interrelation between the contamination level and the coolant velocity.

flow, therefore increasing the particle transfer towards the walls. This dependency is also demonstrated in Figure 3. The contamination level is higher of those components in which the coolant flow velocity is higher. For instance, the average coolant velocity through SP-HPR-4, SP-HPR-1, and SP-HPR-2 components is high and therefore increases the particle deposition rate.

The relative activity of radionuclides in the deposits is changing because of the radioactive decay process. Changes of the relative activity of radionuclides for the most contaminated component of SP-HPR are shown in Figure 4(a). At the final shutdown of the reactor, Fe-55, Fe-59, Mn-54, and Co-60 nuclides are dominant in the contamination of the SP-HPR. The long-lived nuclide Ni-63 is dominant in the deposits after 35 years since the short-lived radionuclides (Fe-55, Co-60, Mn-54, and Fe-59) decay in a short period of time. The activity of other long-lived nuclides remains practically unchanged, so their contribution to the total activity increases.

Nuclides that emit γ radiation define the doses of direct irradiation to workers during dismantling of the system components. Changes of the radionuclides' relative impact to dose rate at the outer surface of the most contaminated component of SP-HPR are shown in Figure 4(b). At the final shutdown of the reactor, γ radiation from the deposits on SP-HPR components is mostly determined by Mn-54, Co-58, Fe-59, and Co-60. But due to longer half-life, Co-60 is the most significant contributor to the total dose rate five years after

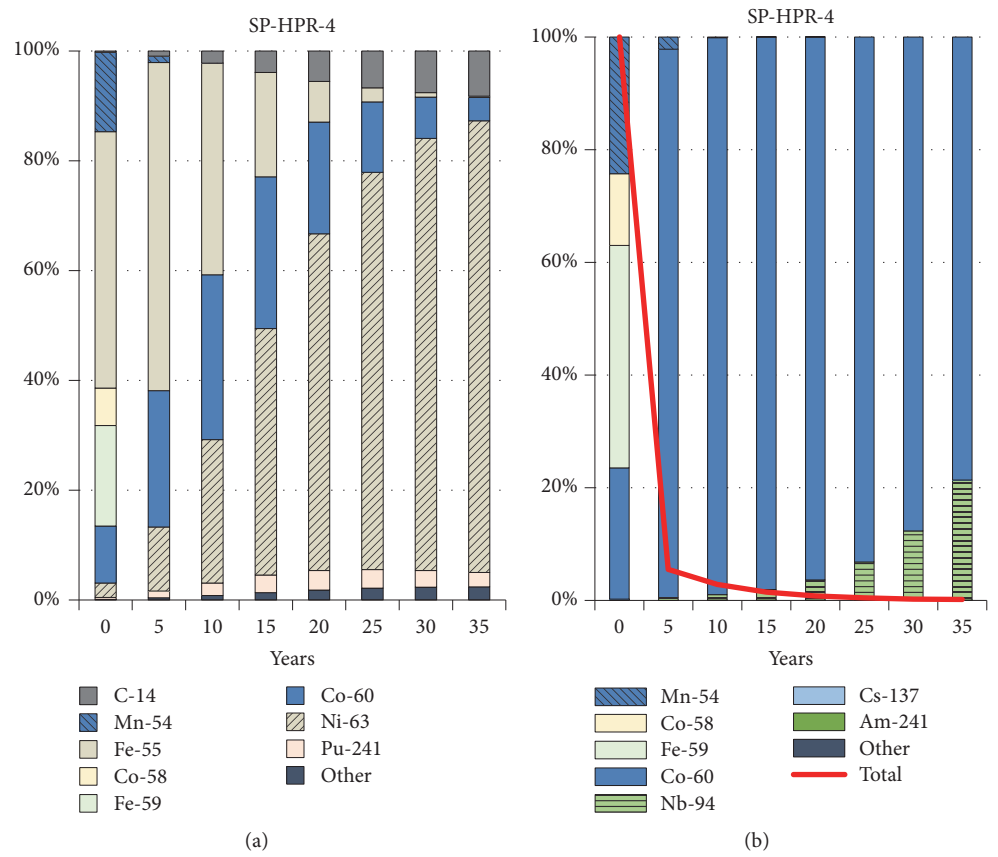

Figure 4: Changes of the relative composition of nuclides for SP-HPR-4 component with time: (a) activity of the deposits; (b) γ dose rate of the deposits (other < 1%).

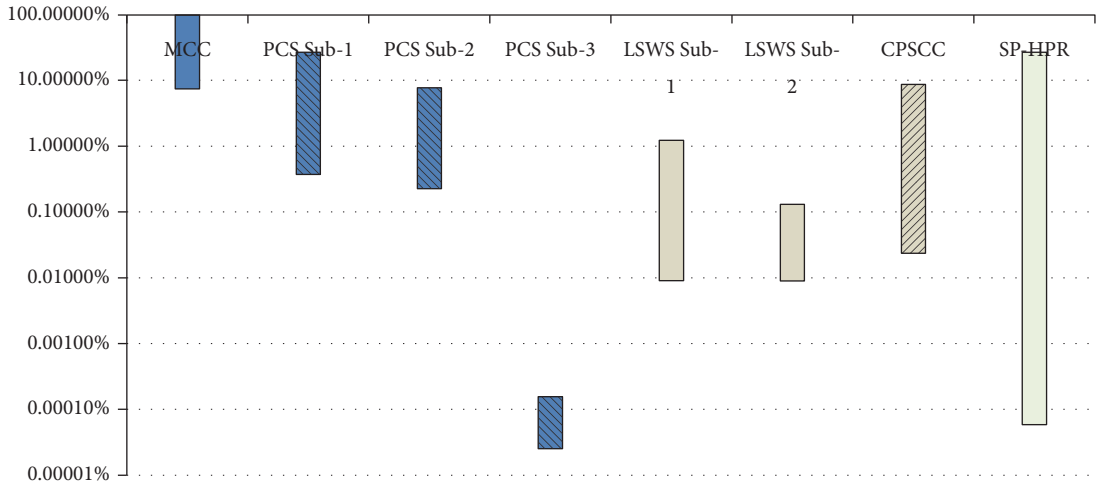

Figure 5: Comparison of relative deposit activity of SP-HPR, MCC [14], PCS [15], LSWS [16], and CPSCC [17] subsystems components compared to the MCC MCP activity (PCS-i:LSWS-i:CPSCC-i:SP-HPR-i / MCC pump).

the final shutdown. Moreover, the total dose rate decreases rapidly during the first 5 years (more than 90%) due to the decay of short-lived radionuclides.

The scattering in the deposit activity ratio (at the final shutdown of the rector) between the most (the top of the bar) and the least (the bottom of the bar) contaminated components of the SP-HPR, MCC [14], PCS [15], LSWS [16], and CPSCC [17] systems compared to the activity of the MCC characteristic component (main circulation pump, MCP) is presented in Figure 5. As is shown in the chart, the activity of SP-HPR is lower than that of MCC and PCS nonpurified water subsystem. It is noteworthy that the deposit activity

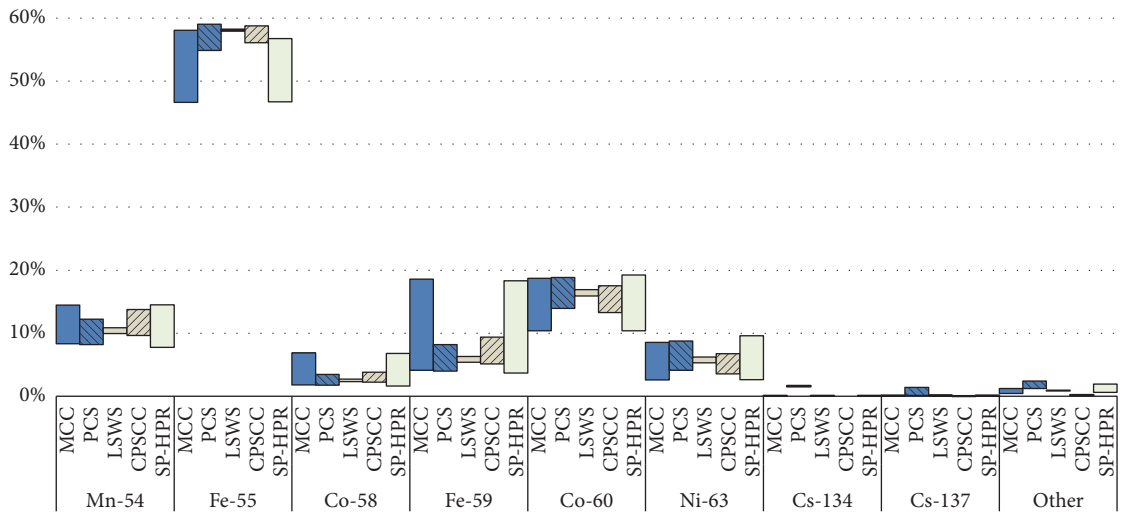

Figure 6: Relative activity of the radionuclides in the deposits of the systems of SP-HPR, MCC [14], PCS [15], LSWS [16], and CPSCC [17] subsystems (other < 1%).

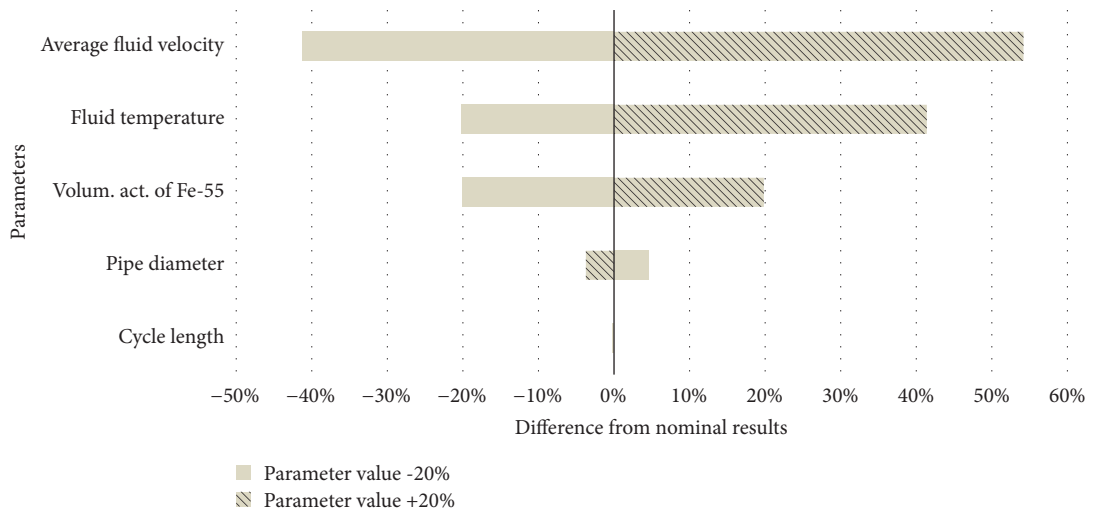

Figure 7: A tornado diagram presenting sensitivity analysis results of SP-HPR-4 component's contamination with Fe-55.

of SP-HPR system components is more scattered compared to other subsystems. This is because HPRs are considerably less contaminated than SPs. The most contaminated and the least contaminated components of SP-HPR constitute about 27% and less than one-tenth thousands of percent of activity, respectively, compared to the activity of the MCC MCP.

Scattering of relative deposit activity after final shutdown of the reactor for a specific radionuclide of the SP-HPR and other RBMK-1500 systems' components is shown in Figure 6. The top and the bottom of the bar represent maximum and minimum relative activity of a component's deposits per radionuclide and per system compared to the total deposit activity for those subsystem's particular components. The highest activity in deposits of the SP-HPR is caused by radionuclides generated from activation of corrosion products as in other systems chosen for comparison. Scattering of activity for SP-HPR components per radionuclide is similar as in the MCC. For both systems, the highest activity in deposits is from Fe-55: MCC 47%–58% and SP-HPR 47%–57% of total activity. Fission products (as Cs-134 and Cs-137) in smaller quantities are deposited on all systems' components (except CPSCC, which should not have nuclides that are generated during nuclear fuel fission or transmutation because contaminated water from this system does not mix directly with MCC water). The contribution of these radionuclides to the total activity is rather small (usually less than 1%), so they are marked as "other".

Sensitivity analysis data on contamination of SP-HPR-4 component with Fe-55, which is the main contributor to the total activity at the reactor's final shutdown, are graphically presented in a tornado diagram (Figure 7). The parameters are presented in line with uncertainty importance on the deposits contamination. Uncertainty of average coolant velocity is the most important. Reduction of its value by 20%

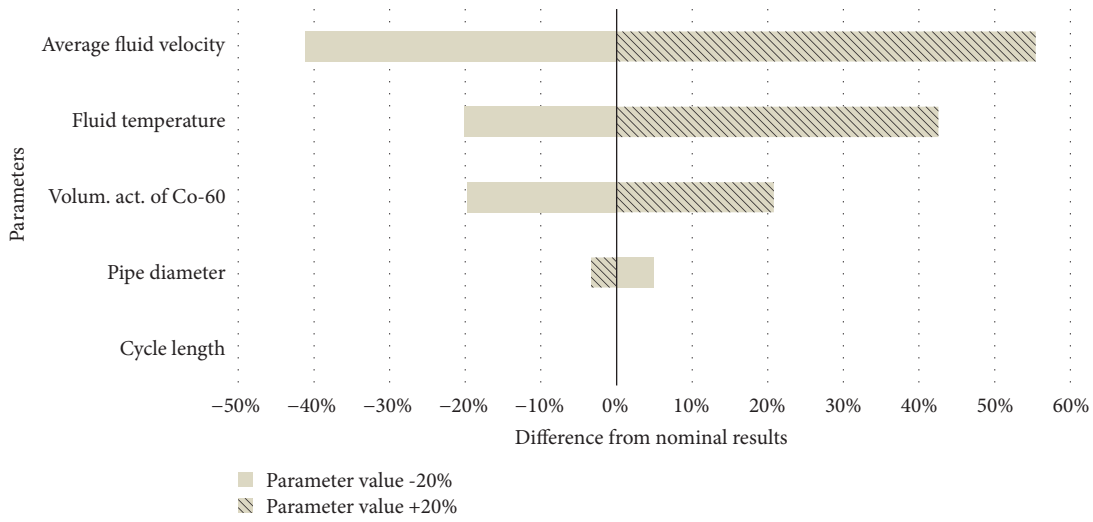

Figure 8: A tornado diagram presenting results of the sensitivity analysis of SP-HPR-4 component's contamination with Co-60.

will give 40% decrease in the deposit contamination with Fe-55. Increase of the coolant temperature (°C) parameter by 20% will result in increased deposit activity caused by Fe-55 by about 54%. Uncertainty of the activity of this radionuclide in coolant is also important. Uncertainty of pipe diameter and cycle length is not that important estimating the contribution of Fe-55 to the contamination of SP-HPR-4 component.

Figure 8 shows sensitivity analysis data of the deposits contamination with Co-60 of SP-HPR-4 component. Five years after the final shutdown of the reactor, Co-60 is the main contributor to the total dose. Similarly as with Fe-55, the uncertainty of average coolant velocity has the highest impact evaluating the SP-HPR-4 component's contamination uncertainty with Co-60. The velocity variation from -20% to +20% from the nominal value will result in ~41% and ~56% activity variation, respectively. Uncertainty of fluid temperature and Co-60 activity in the fluid are also of high importance, whereas uncertainties of the diameter of the pipe and the length of the cycle are not that important.

5. Conclusions

Component contamination of steam pipelines (SP) and high pressure rings (HPR) was modelled and analysed in this investigation. Modelling data were compared with the contamination results of other systems of the RBMK-1500 reactor. Based on this, the following conclusions have been drawn:

(1) Steam pipes to the turbine (SP-HPR-4) and steam pipes from the drum-separator to headers (SP-HPR-1) with steam headers (SP-HPR-2) are the most contaminated components. Contamination of other components is much lower and comprises less than 1% of the contamination of the component with the highest level of contamination (SP-HPR-4) contamination.

(2) Just after the final shutdown of the reactor, γ radiation from the deposits on SP-HPR components is mostly determined by Mn-54, Co-58, Fe-59, and Co-60. But due to longer half-life, Co-60 is the most significant contributor to the total dose rate five years after the final shutdown. Moreover, the total dose rate decreases rapidly during the first 5 years (more than 90%) due to the decay of the short-lived radionuclides.

(3) Contamination of the SP-HPR system is lower in comparison with the main circulation circuit (MCC) and purification and cooling system's (PCS) nonpurified water subsystem, and activity scattering amongst the components of the SP-HPR is larger in comparison to other subsystems.

(4) Highest activity in deposits of the SP-HPR is caused by radionuclides generated from activation of corrosion products as in other RBMK-1500 systems. The highest activity in deposits is from Fe-55, i.e., 47%–57% of total SP-HPR contamination.

(5) Sensitivity analysis results showed that the most important input parameters are average coolant velocity, coolant temperature, and volumetric activity in the coolant.

Abbreviations

ALS: Accident localisation system
HPR: High pressure rings
MCC: Main circulation circuit
MCP: Main circulation pump
PCS: Purification and cooling system
SP: Steam pipelines.

Data Availability

The main data used to support the findings of this study are included within the article. Detailed data used for modelling

have not been made available because it is a commercial secret.

Conflicts of Interest

The authors declare that there are no conflicts of interest regarding the publication of this paper.

References

[1] "Radiological characterization of shut down nuclear reactors for decommissioning purposes," IAEA Technical Reports Series No. 389, 1998.

[2] *Radiological Characterisation for Decommissioning of Nuclear Installations*, OECD/NEA, Paris, France, 2013.

[3] "Modelling of transport of radioactive substances in the primary circuit of water-cooled reactors," IAEA Technical Reports Series No. 1672, 2012.

[4] G. Comley, "The significance of corrosion products in water reactor coolant circuits," *Progress in Nuclear Energy*, vol. 16, no. 1, pp. 41–72, 1985.

[5] V. G. Kritskii, *Water Chemistry and Corrosion of Nuclear Power Plant Structural Materials*, Russian Materials Monograph Series, American Nuclear Society, La Grange Park, Ill, USA, 1999.

[6] "Coolant technology of water cooled reactors: an overview," IAEA Technical Reports Series No. 347, 1993.

[7] M. Laraia, *Nuclear Decommissioning: Planning, Execution and International Experience*, M. Laraia, Ed., Woodhead Publishing Series in Energy, Woodhead Publishing, Philadelphia, PA, USA, 2012.

[8] B. J. Lewis and A. Husain, "Modelling the activity of 129I in the primary coolant of a CANDU reactor," *Journal of Nuclear Materials*, vol. 312, no. 1, pp. 81–96, 2003.

[9] P. Beslu, G. Frejaville, and A. Lalex, "21. A computer code PACTOLE to predict activation and transport of corrosion products in a PWR," in *Water Chemistry of Nuclear Reactor Systems*, pp. 195–201, Thomas Telford Publishing, 1978.

[10] J. S. Song, H. J. Cho, M. Y. Jung, and S. H. Lee, "A study on the application of crudtran code in primary systems of domestic pressurized heavy-water reactors for prediction of radiation source term," *Nuclear Engineering and Technology*, vol. 49, no. 3, pp. 638–644, 2017.

[11] K. A. Burrill and P. Menut, "A description of the activity transport computer codes in the iaea benchmarking exercise," in *Water Chemistry of Nuclear Reactor Systems*, vol. 8, pp. 519–526, Thomas Telford Publishing, 2001.

[12] J. Zhang, L. Li, S. He, and Y. Chen, "Calculation of radioactivity and dose rate of activated corrosion products in water-cooled fusion reactor," *Science and Technology of Nuclear Installations*, vol. 2016, Article ID 6051834, 6 pages, 2016.

[13] B. Lemens, B. Centner, P. Beguin, and K. Mannaerts, "Determination and declaration of critical nuclide inventories in Belgian NPP radwaste streams," in *Proceedings of WM99 Conference*, 1999.

[14] P. Poskas, R. Zujus, and A. Brazauskaite, "Preliminary radiological characterisation of the main circulation circuit at Ignalina NPP for decommissioning purposes," in *Proceedings of WM'04 Conference*, pp. 1–9, 2004.

[15] G. Poskas, R. Zujus, P. Poskas, and G. Miliauskas, "Modelling of the radiological contamination of the RBMK-1500 reactor water purification and cooling system," *Science and Technology of Nuclear Installations*, vol. 2014, Article ID 293158, 8 pages, 2014.

[16] G. Poskas, R. Zujus, and P. Poskas, "Analysis of the radiological contamination of the RBMK-1500 reactor low salted water system," *Progress in Nuclear Energy*, vol. 85, pp. 707–712, 2015.

[17] G. Poskas and R. Zujus, "Modelling of the radiological contamination of the RBMK-1500 reactor control and protection system channels' cooling circuit," *World Journal of Engineering and Technology*, vol. 03, no. 03, pp. 1–5, 2015.

[18] M. Reck, P. S. Larsen, and U. Ullum, "Particle deposition in low-speed, high-turbulence flows," *Atmospheric Environment*, vol. 36, no. 30, pp. 4801–4809, 2002.

[19] A. Dehbi, "Assessment of a new fluent model for particle dispersion in turbulent flows," in *Proceedings of the Workshop on Benchmarking of CFD Codes for Application to Nuclear Reactor Safety (CFD4NRS)*, 2006.

Hindawi
Science and Technology of Nuclear Installations
Volume 2019, Article ID 4309545, 13 pages
https://doi.org/10.1155/2019/4309545

Research Article

A Methodology for Optimizing the Management of Spent Fuel of Nuclear Power Plants Using Dry Storage Casks

Ian B. Gomes,[1] **Pedro L. Cruz Saldanha**,[2] **and Antonio Carlos M. Alvim**[1]

[1]*COPPE, Programa de Engenharia Nuclear, Universidade Federal do Rio de Janeiro, UFRJ, 21941-914, Brazil*
[2]*CGRC/DRS, Comissão Nacional de Energia Nuclear, 22290-901, Brazil*

Correspondence should be addressed to Antonio Carlos M. Alvim; aalvim@gmail.com

Received 29 August 2018; Accepted 22 January 2019; Published 7 February 2019

Guest Editor: Dimitrios Tsaoulidis

The management of spent nuclear fuel assemblies of nuclear reactors is a priority subject among member states of the International Atomic Energy Agency. For the majority of these countries, the destination of such fuel assemblies is a decision that is yet to be made and the "wait-and-see" policy is thus adopted by them. In this case, the irradiated fuel is stored in on-site spent fuel pools until the power plant is decommissioned or, when there is no more racking space in the pool, they are stored in intermediate storage facilities, which can be another pool or dry storage systems, until the final decision is made. The objective of this study is to propose a methodology that, using optimization algorithms, determines the ideal time for removal of the fuel assemblies from the spent fuel pool and to place them into dry casks for intermediate storage. In this scenario, the methodology allows for the optimal dimensioning of the designed spent fuel pools and the casks' characteristics, thus reducing the final costs for purchasing new Nuclear Power Plants (NPP), as the size and safety features of the pool could be reduced and dry casks, that would be needed anyway after the decommissioning of the plant, could be purchased with optimal costs. To demonstrate the steps involved in the proposed methodology, an example is given, one which uses the Monte Carlo N-Particle code (MCNP) to calculate the shielding requirements for a simplified model of a concrete dry cask. From the given example, it is possible to see that, using real-life data, the proposed methodology can become a valuable tool to help making nuclear energy a more attractive choice costwise.

1. Introduction

In 2018 there were a total of 451 nuclear reactors in operational conditions (i.e., connected to the electrical grid of their countries) in the world. These reactors made up a total of 0,391 TW of installed electrical power. That year, these reactors utilized 65014 tons of uranium. In 2015, 2.44 trillions of kWh was generated by thermonuclear sources, which equals about 11.5% of all electrical energy produced that year [1].

Depending on the operator's decision, the spent fuel discharged from a nuclear reactor goes through one of the possible management strategies listed below [2].

(i) Once-trough cycle, when the fuel is sent to be disposed in a repository.

(ii) Closed cycle, when the fuel is reprocessed and reused in a nuclear reactor.

(iii) The "wait-and-see" policy, when the fuel is stored indefinitely and the decision on either reprocessing or disposal is made at a later moment.

Any one of these strategies demands that the spent fuel is stored for an initial period of time.

Högselius [3] argued that it is possible to consider the exportation of spent fuel to countries that detain reprocessing technology as a fourth possible policy. In general, the reprocessed fuel returns to its origin country after the operation.

Högselius also identifies five factors that can influence the decision of a country to opt for one of these policies. They are: military ambitions and nonproliferation, technological culture, political culture and civil society, geological conditions and energy policy [3].

A new approach that is also being considered is the Advanced Fuel Cycle [4], which is considered to be a closed cycle strategy whose goal is to use chemical separation

technologies to remove the constituents of the spent fuel that contribute the most to its decay heat generated and volume, such as separating pure uranium that can be reprocessed or disposed as low-level waste and separating cesium and strontium, removing the short-term heat load.

The three main objectives of pool storage of spent fuel are cooling the fuel assemblies, shielding the workers, and the public from radiation emitted from the fission products present in the fuel and to avoid criticality accidents. A typical spent fuel pool has a depth of approximately 12 m and an area of 12 m x 12 m. The walls are usually built out of reinforced concrete with 1.2 m to 2.4 m thickness. The inside walls of the pool are lined with stainless steel [5].

Dry casks were first used in 1986 at the Surry power plant as a temporary solution until a permanent destination was defined. However, no permanent solution was ever put in practice by the majority of operators [6].

The storage of spent fuel in dry casks has the same basic safety objectives as storage in pools. However, for dry casks, these objectives must be fulfilled without the use of water and mechanical devices. Cooling must be achieved passively, through air and the structural materials that are used to construct the cask. Shielding is also achieved by the choice of materials that make up the cask which may be lead, concrete and/or steel, to attenuate gamma photons, and metals or boron impregnated resins to attenuate neutrons. The criticality control is achieved by the arrangement of the fuel assemblies inside the cask and by racking baskets that contain boron in their structure to absorb neutrons and maintain the geometry of the fuel [5].

The decision begins with the choice of purpose of the container, i.e., storage only or storage and transport. The main difference between the two options is the fuel temperature allowable for transport casks, as it needs to be considerably lower so that the materials that are used comply with weight and dimension requirements of available means of transport [7].

The crucial technical parameters for a licensed dry cask design are majorly defined by the characteristics of the fuel to be stored or transported, especially its physical dimensions, initial enrichment, burnup, and the initial cooling time after the plant operation, which determines the heat generation rate at the beginning of storage or transport [5].

A plan for the management of spent fuel that is elaborated efficiently can result in the design of a spent fuel pool that occupies a smaller area than one that is designed to store for undetermined time the fuel from the whole life span of a nuclear power plant.

The aim of the study presented in this paper is to propose a methodology to optimize the time to remove fuel elements from the initial storage spent fuel pools at reactor sites, taking into account the refueling schedule of the power plant, the isotopic concentrations in the fuel at the time of its removal from the pool (i.e., the source term) and its storage costs. In consequence, it is possible to determine the most efficient dimensions for the spent fuel pool and the optimal design features of an intermediate storage system, assuming that, during the design stage of a new plant, it has been determined that, sometime in its lifetime, the spent fuel will be moved to an intermediate facility that employs dry storage casks. The proposed methodology is therefore intended for countries that have chosen dry casks as solution for interim storage of spent fuel and does not consider interim storage in pools. It is assumed that regulatory requirements, such as the mechanical limits of the casks and the spent fuel pool, are to be addressed by the designer after the initial dimensioning optimization is fulfilled, which is the goal of the proposed methodology.

Spencer et al. [8] developed a methodology to optimize the loading configurations of fuel assemblies in dry casks that minimize the number of casks to be employed, their heat load and the time at which they meet transportation requirements. That study, however, does not intend to optimize, in terms of cost, the design features of either the spent fuel pool nor of those the dry casks.

Figure 1 presents a general description diagram of the methodology proposed in this paper.

2. Materials and Methods: Steps Required for the Application of the Methodology

The steps required for the application of the methodology are listed below. They do not necessarily have to be followed in this exact order.

(1) Definition of the operation scenario of the NPP.

(2) Definition of the type and average characteristics of the fuel assembly to be used in the NPP.

(3) Simulation of the NPP's operation using reactor physics codes.

(4) Definition of the type of dry cask to be employed for the intermediate storage of spent fuel.

(5) Modeling of the storage costs for the spent fuel pool, in relation to the number of fuel assemblies to be stored in it and modeling of the storage costs for the chosen dry cask, considering the number of fuel assemblies to be stored in it and the parameters of the spent fuel at the time it is removed from the spent fuel pool.

(6) Establishment of the dose rate limits at the points of interest for the installation licensing.

(7) Establishment of the temperature limits of the structural materials that compose the dry casks.

(8) Market research of the costs involved in the construction of the spent fuel pool and the dry casks.

(9) Application of the obtained models and input data to an optimization algorithm.

Figure 2 presents a flow diagram of all the steps involved and the following sections describe them in further detail.

2.1. Operation Scenario. At this step, the main characteristics of the NPP must be defined. They are the number of units operating at the NPP, type of reactor, i.e., Pressurized Water Reactor (PWR), Boling Water Reactor (BWR), etc., reactor power, duration of the refueling cycle, number of fuel

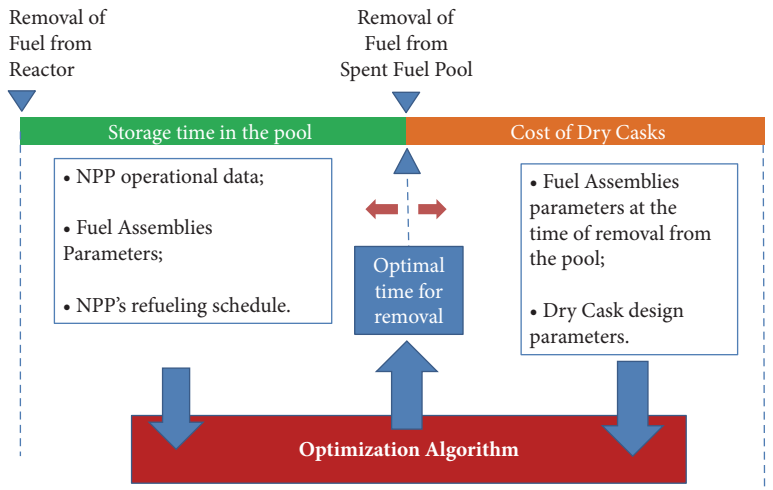

Figure 1: Overview of the spent fuel management optimization methodology.

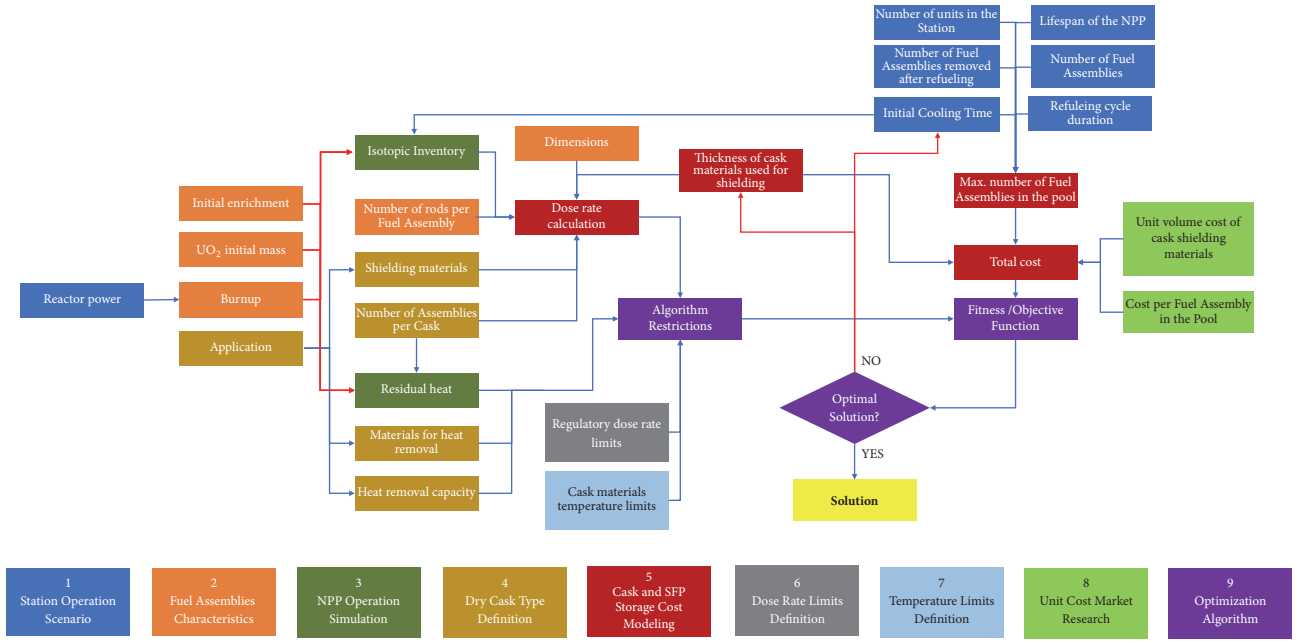

Figure 2: Flow graph of the steps involved in the proposed methodology.

assemblies used in the reactor, number of fuel assemblies that return to the reactor after a refueling outage and the life span of the NPP.

2.2. Fuel Assembly Parameters. It must be observed that inside a nuclear reactor there are fuel assemblies with different characteristics, arranged in such a manner to allow for the correct and efficient operation of the plant. At each refueling, this arrangement is altered and as such, it is difficult to predict, at the design stage of the plant, the parameters of all the fuel assemblies that will need to be stored. This methodology uses as input data the parameters of a typical fuel assembly that is usually employed with the chosen reactor type and the hypothesis of equilibrium [9] is adopted.

The fuel assembly parameters that must be known are the number of fuel rods per assembly, assembly pitch, assembly height, initial UO_2 mass, initial enrichment and burnup.

2.3. Simulation of the NPP's Operation. It is necessary that a simulation of the operation of the plant is carried out, using reactor physics codes. This simulation provides information on the isotopic concentrations and residual heat present in the irradiated fuel. It is also necessary to simulate how the isotopic concentrations change and the decay heat decreases during the time the spent fuel is stored in the pool.

2.4. Choice of Dry Cask Type. At this stage, the type and characteristics of the dry casks to be employed must be

defined. They are: purpose (i.e., storage or storage and transport); capacity (i.e., number of fuel assemblies that can be stored in it); materials used for shielding; and heat removal capacity.

2.5. Modeling of Storage Costs. It is necessary to obtain a function that describes the costs involved in the management of spent fuel, which is a function of the initial storage time of the fuel in the spent fuel pool. A fraction of the cost is independent of the time the fuel stays in the pool, such as personnel and machinery involved in the transference of the fuel to the dry casks and the costs for the construction of the dry casks that are not dependent on the parameters of the spent fuel assemblies.

As such, it is possible to define

$$C_{total}(t) = C_{sfp}(t) + N_{cask}C_{cask}(t) + C_{const} \quad (1)$$

$$C(t) = C_{sfp}(t) + N_{cask}C_{cask}(t) \quad (2)$$

where t is the initial cooling time, i.e., the time the spent fuel assemblies are stored in the at-reactor spent fuel pool, $C_{total}(t)$ is the total costs of management of spent fuel, $C_{sfp}(t)$ is the costs of storage in the spent fuel pool that are function of t, N_{cask} is the number of casks that will be needed to store all the fuel assemblies from the NPP's life span, $C_{cask}(t)$ is the cost of storage in one dry cask that is a function of t, C_{const} is the fraction of the cost of storage that is not a function of t, and $C(t)$ is the total costs of the fuel storage which is a function of t. Costs from racking space in the pool as a margin for emergencies can be considered as part of C_{const}, as this does not depend on the initial cooling time.

Figure 3 presents a sketch of the expected behavior of the contributions of the spent fuel pool and the dry casks cost to the overall cost of the spent fuel management.

For the spent fuel pool model, the defining parameter is the maximum number of fuel assemblies that are to be stored in it simultaneously. The costs associated with the heat removal and shielding of the radiation from the spent fuel are all lumped into a single value (C_{FA}) that represents the cost of storage per fuel assembly in the pool.

The number of fuel assemblies stored simultaneously in the pool depends on the rate of removal of fuel assemblies from the reactor, in accordance with the refueling schedule of the NPP, and the rate of removal of fuel elements from the pool, after the initial cooling period. Figure 4 presents the flow of fuel assemblies in and out of an at-reactor spent fuel pool that may be shared by the n units of a NPP.

$C_{sfp}(t)$ can therefore be written as

$$C_{sfp}(t) = C_{FA} \max[N(t,T)] \quad (3)$$

where $N(t,T)$ is the number of fuel assemblies in the pool at time T from the beginning of the NPP operation and in function of the initial cooling time t and $\max[N(t,T)]$ is the maximum value of $N(t,T)$ during the life span of the NPP. $N(t,T)$ is thus defined as

$$N(t,T) = \int_{T_o}^{T} N_{in}(T)\,dT - \int_{T_0}^{T} N_{out}(t,T)\,dT \quad (4)$$

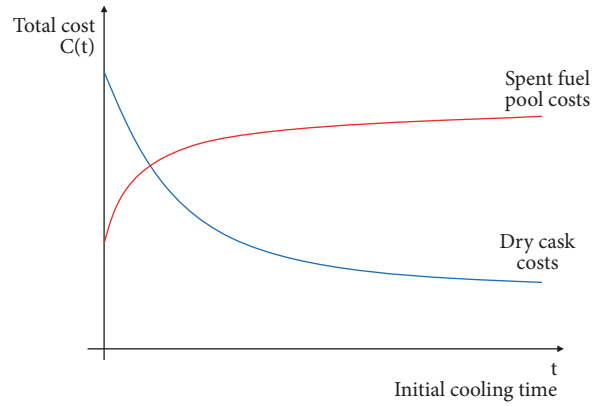

Figure 3: Illustrative sketch of the behavior of the contributions to the spent fuel storage costs.

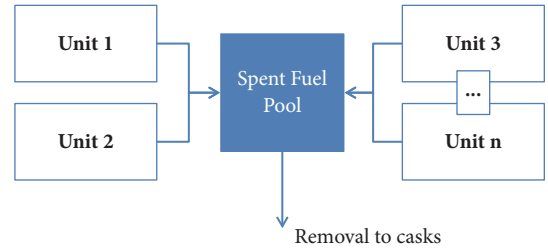

Figure 4: Flow of fuel assemblies in and out of a spent fuel pool shared by the n units of a NPP.

where $N_{in}(T)$ is the number of fuel assemblies that are placed in the pool at time T from the beginning of the NPP operation and $N_{out}(t,T)$ is the number of fuel assemblies that are removed from the pool at time T and in function of the initial cooling time t.

As stated earlier, the outflow of fuel assemblies from the pool depends on the time they stay in it for initial cooling. However, in this optimization problem, the cost of the dry casks is also dependent of the initial cooling time. The pricing of the dry casks is related to the characteristics of the fuel assemblies that are to be stored in them. The main parameters to be taken into consideration are the number of assemblies to be stored in a single cask, the decay heat and the activity of the fission products still present in the fuel at the time of transference to the casks [11]. These last two parameters are functions of t.

The main radiation sources that should be considered for the shielding design of a dry storage unit are primary gamma rays emitted from fission products and actinides, gamma rays from Cobalt-60 in the fuel assemblies' structural materials, secondary gamma rays from the radiative capture of neutrons by cask materials, neutrons from subcritical and spontaneous fission and neutrons emitted from (α, n) reaction of fissile material [6].

Chen et al. [12] made an accuracy and computational efficiency comparison of dose rate calculations for a spent fuel storage cask using the MCNP and SAS4 (Shielding Analysis Sequence 4) computer simulation codes, whose

main differences are the cross-section libraries and the imbedded variance reduction techniques MCNP has. In this comparison, MCNP's overall performance was better, although SAS4 was more efficient when the only concern was the dose rate measured at the side of the cask.

Gao et al. [6] used MAVRIC (Monaco with Automated Variation Reduction using Importance Calculations) to compare the dose rate distributions, with high level of detail, of a TN-32 cask, designed by Transnuclear [13], with two geometry models and two cross-section datasets. The study concludes that primary gamma rays contribute to ~91% of the total dose rate at the side surfaces of the cask and to ~99% at the top surface.

It is assumed for this study that measures for maintaining the subcriticality are guaranteed by the geometry of the positioning of the fuel assemblies inside the casks and by the use of boron in the spacing baskets inside the casks. The costs that result from these measures are not considered in this analysis, though they will be considered in future studies, as optimal positioning of the fuel assemblies in the casks might contribute to reducing the costs of boron used in the spacing brackets.

2.6. Dose Rate Limits. The dose rate limits to be respected by the dry cask design are those that are established by the regulatory agencies of each country. These limits will establish the minimal shielding capacity that the cask designer must demonstrate.

In the United States, these limits are established in accordance with 10 CRF part 72 [14]. However, as observed in NUREG 1536 [15], the federal regulation does not impose specific dose rate limits for individual dry casks, as acceptable dose rates depend on various factors, such as the geometry of the dry casks array, time the workers need to stay in the vicinity of the casks and the proximity to areas usually inhabited by workers. In previous evaluations, in the light of 10 CFR part 72 [14], US NRC has accepted dose rates ranging from 0.2 mSv/h to 4 mSv/h. NUREG 1536 [15] also states that the dose rates must be calculated at a distances of 1 m from points such as the surface of the cask and the air vents, as these dose rates typically contribute to the exposure of the workers.

2.7. Temperature Limits. The temperature limits of the materials that compose the selected dry casks, as well as their heat removal capacities, define the maximum decay heat allowed for the fuel assemblies to be stored in them.

Li et al. [16] presented a thermal analysis of a vertical storage dry cask containing 32 fuel assemblies with a total decay heat load of 34 kW using the ANSYS/FLUENT code. Several configurations of cannister fill gas, internal pressure and basket material were studied in order to determine peak cladding temperature and cannister surface temperatures. For this study, the dry cask was modeled after the HI-STORM 100 system by HOLTEC International [17].

2.8. Market Research. To obtain results with economic relevance, its necessary that a market research is carried out in order to estimate the costs of storage per fuel element in the spent fuel pool and the costs for the acquisition of the dry casks with the minimal parameters to guarantee the integrity of the fuel assemblies stored in them and that the minimal shielding capacity that must be fulfilled.

The change of unit costs over time was not considered in this analysis, though it might be the subject of future studies with the contribution of specialists in the economics field.

2.9. Optimization. The final step is the coding of an optimization algorithm, using all the data gathered up to this point, to obtain the optimal time to remove the fuel assemblies from the spent fuel pool and transfer them to the dry casks. The fuel assemblies' parameters, the NPP operational data, and the values obtained from the market research are used as input data to the problem. The function that models the sum of spent fuel pool and dry casks costs is used as a fitness or objective function to be minimized. The temperature and dose rate limits are used as restrictions for the algorithm.

3. Example of Application

3.1. Hypothetical NPP. To demonstrate the methodology, it is necessary to establish a hypothetical model of a NPP that will operate in accordance with the premises adopted for this study. This NPP will be referred to as the Hypothetical NPP or the HNPP.

The HNPP is comprised of one reactor unit of the PWR type, whose electrical power is 640 MW. Its main parameters are as follows:

(i) Number of fuel assemblies: 121.

(ii) Number of fuel rods per assembly: 235.

(iii) Fuel assembly pitch: 19.82 cm.

(iv) Fuel assembly height: 4 m.

(v) Initial UO_2 mass per Fuel Assembly: 0.47 MTU.

(vi) Average refueling enrichment: 4.0%.

(vii) Average Maximum Burnup: 55000 MWd/t.

(viii) Refueling frequency: 12 months.

(ix) Fraction of the core that is removed after refueling: ~33%.

It is established that the HNPP will operate for 60 years, will only be shut down for refueling and that it will operate at its nominal power during its whole life span.

The following simplifications will be adopted for the HNPP operation:

(i) From the first operational cycle, it is considered that the core is at equilibrium.

(ii) At each refueling, the new core will have the same configuration as the one before it.

(iii) All the fuel assemblies that are going to be stored have the same isotopic concentrations and decay heat. In this case the average parameters were adopted, in view of the available data.

(iv) Only normal operation will be considered. Accidental scenarios are not studied.

Considering that the reactor core has 121 fuel assemblies and that approximately one-third of them is removed during a refueling outage and assuming that ~1% of these assemblies fail and must remain in the spent fuel pool, we can assess that 40 fuel assemblies will be removed at each refueling operation. For this reason, a dry cask design that can store 24 fuel assemblies was chosen, similar to the one made available by HOLTEC with their HI-STORM 100 system [17], and two of them (with 20 fuel assemblies each) will be needed for each refueling operation.

As the life span of the HNPP is 60 years, refueling is carried out every 12 months, and in the last year of operation the whole fuel will be removed from the reactor core, the total number of dry casks that will need to be purchased is

$$N_{cask} = 124 \quad (5)$$

The failed fuel assemblies will not be considered in the example, as they require special analysis before disposal.

3.2. Dry Cask Selection. A single purpose cask design, i.e., storage only, was selected for this example. The simplified model of the cask comprises an internal cylindrical canister which holds up to 24 fuel assemblies arranged in baskets where 20 assemblies will be stored.

An outer concrete cylinder provides shielding from the radiation within. Two concrete lids, at the top and at the bottom provide shielding from the radiation that may come from those directions.

Air ducts in between the two cylinders allow for the passive removal of decay heat from the fuel. Boron injected traps placed in the air ducts ensure that no radiation flows through the air inlets at the bottom of the cask and the outlets at the top of the cask.

3.3. Spent Fuel Data. For this example, the fuel data was obtained from NUREG 7227-"US Commercial Spent Nuclear Fuel Assembly Characteristics: 1968-2013" [10]. This document provides a compilation of fuel assemblies from BWR and PWR reactors arranged by various burnup, initial enrichment and initial cooling time values. In this document, with data obtained from the GC-859 database, simulations were carried out using the ORIGEN code and information such as decay heat, isotopic concentrations and activity were presented.

The document presents these values for initial cooling times of 5 hours, 1 day, 90 days, 1 year, 5 years, 10 years, 100 years and 200 years, for three PWR and three BWR groups arranged in accordance with the year the fuel assemblies were removed from their respective reactors. This arrangement coincidentally places the assemblies in groups with roughly similar median initial enrichment and burnup values [10].

From the PWR-3 group, where the HNPP reactor parameters fall, the isotopic concentrations and activity data were obtained. The values that occur in between the available initial cooling times were interpolated.

3.4. Cost Modeling. The model that represents the costs of the spent fuel pool is used as described in Section 2.6. The model that represents the costs of the dry casks is described as follows.

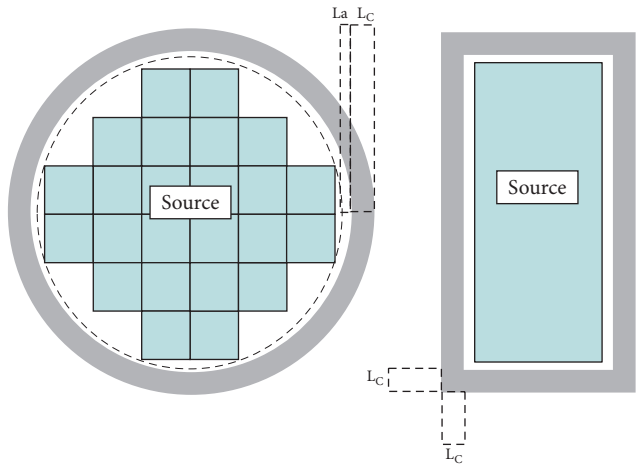

Figure 5: Model for the thickness of the materials used for the shielding of radiation.

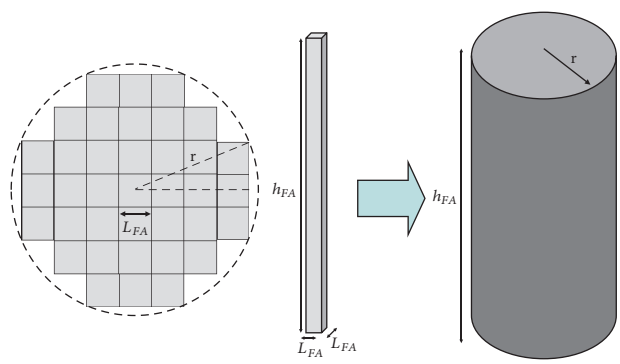

Figure 6: Approximate model of the radioactive source inside the cask.

Figure 5 shows the model for the thickness of the materials used for the shielding of radiation from the source comprised of the fuel elements inside the cask, where L_a is the air ducts thickness and L_c is the concrete layer thickness. The stainless steel lining of the inner cask, represented by the dotted line, is not considered in this example, as well as the contribution of the air in the cooling ducts, so $L_a = 0$ cm. The influences of the structural materials of the fuel assemblies and the boron injected baskets are also not considered. These assumptions make the example analysis more conservative.

The bundle of 20 fuel assemblies that make up the source inside the cask are then approximated to a cylinder, as described by Figure 6 and Equations (6) and (7). The approximation considers the 24 available slots for fuel assemblies inside the cask, even though 4 of them are left unused. For this example, as the approximation considers a homogeneous cylindrical source, it does not matter which slots remain empty. The empty slots may contribute to optimizing the shielding capacity of the cask and must be considered in a more accurate model of the source.

$$r^2 = \left(3L_{FA}\right)^2 + {L_{FA}}^2 \quad (6)$$

$$V_S = \pi r^2 h_{FA} \quad (7)$$

where

r is radius of the cylinder that approximates the geometry of the source.

L_{FA} is length of the side of the fuel assembly.

h_{FA} is height of the fuel assembly.

V_S is source volume.

From the values defined in Section 3.1,

$$r = 60.71cm \quad (8)$$

$$V_S = 46.324m^3 \quad (9)$$

Considering that the mass of UO_2 in one fuel assembly is 0.47 MTU, for the whole source term, the mass of UO_2 in a single cask is 9.4 MTU.

The cost of the whole array of dry casks, as considered in this example, is then defined as

$$C_{cask} = C_c N_{cask} \left[\pi \left(r + L_c\right)^2 \left(h_{FA} + 2L_C\right) - V_S\right] \quad (10)$$

where C_c is the cost per unit volume of concrete and L_C is the concrete shielding thickness.

In a more realistic case, (10) must include the other contributions to the cost of the cask array, as defined by the analyst.

3.4.1. Concrete Thickness Calculation. As stated in Section 2.7, in the past US NRC has accepted dry casks designs that could demonstrate dose rates ranging from 0.2 mSv/h to 4 mSv/h [15]. Both the lower and upper boundaries were chosen for this example, with the objective of demonstrating the influence the dose rate limits has on the optimization process, as part of a simple sensitivity analysis. It was decided that these dose rates would be calculated at a point located 1 meter away from the lateral surface of the cask, measured at its centerline as it is expected that it is where the dose rate is highest for the cylindrical source considered.

The calculation of the thickness of concrete needed to limit the dose rates was done with the MCNP code [18]. To accomplish this, the geometry of the cask was modeled on the MCNP input file and the concrete thickness was varied from 10 cm to 50 cm in increments of 10 cm. The dose rates were measured with a ring detector tally, centered at the Z axis and with radius equal to 1 meter plus the thickness of concrete shell and the radius of the source cylinder.

To simplify this model, the only isotope that was considered in the source was Cesium-137, because at each decay it emits a photon with a fixed energy of 0.6617 MeV, which is high enough so that it penetrates the shielding and can be measured at the detector. The detector tally was modified such as the results would be presented in pSv per 1 Bq activity in the source. To obtain the actual dose rate on the measured location, this value is then multiplied by the activity of the source. This approximation underestimates the activity of the source, but serves the purpose of demonstrating the methodology. Table 1 presents the activity and mass of Cesium-137 in the spent fuel per MTU and Table 2 presents these values for the mass of initial UO_2 in one dry cask [10]. Table 3 presents the results obtained from the MCNP simulations.

Table 1: Activity and mass of Cesium-137 in the spent fuel per MTU (adapted from [10]).

Cesium-137 - PWR-3 (47 GWd/MTU)		
Initial Cooling Time	Activity (Ci/MTU)	Mass (g/MTU)
5 hours	1.48E+05	1.71E+03
1 day	1.48E+05	1.71E+03
90 days	1.47E+05	1.70E+03
1 year	1.45E+05	1.67E+03
5 years	1.32E+05	1.52E+03
10 years	1.18E+05	1.36E+03
50 years	4.68E+04	5.39E+02
100 years	1.48E+04	1.71E+02
200 years	1.48E+03	1.71E+01

Table 2: Activity and mass of Cesium-137 in the spent fuel per cask.

Inital Cooling Time	Activity (Ci)	Mass (g)
5 hours	1.39E+06	1.61E+04
1 day	1.39E+06	1.61E+04
90 days	1.38E+06	1.60E+04
1 year	1.36E+06	1.57E+04
5 years	1.24E+06	1.43E+04
10 years	1.11E+06	1.28E+04
50 years	4.40E+05	5.07E+03
100 years	1.39E+05	1.61E+03
200 years	1.39E+04	1.61E+02

Table 3: MCNP simulation results.

Concrete thickness (cm)	Dose per decay at the source (pSv)	Relative Error
10	5.36E-08	0.0109
20	2.18E-10	0.0495
30	6.36E-13	0.0712
40	1.86E-16	0.1721
50	1.90E-19	0.1095

The MCNP user manual [18] states that for a measurement at a point or ring detector to be reliable, its associated relative error must be smaller than 0.05. Due to restraints to hardware resources available for this study, this desired value could not be reached. However, as the order of magnitude of the values with the lowest relative error achieved were in the expected range, it was decided that they were acceptable for demonstration purposes of this example. The values that fall in between the 10 cm increments were interpolated.

3.5. Decay Heat Removal. The calculation of the heat removal capacity of dry casks is usually done using Computational Fluid Dynamics (CFD) codes. The purpose of such studies is to determine the behavior of the materials chosen and verify if they fulfill the cooling requirements [19]. For the present example, heat removal analysis was not carried out, and it is assumed that the temperature limits of the materials are always respected. In a real case, these limits would be used as boundaries for the optimization algorithm.

3.6. Market Research. For this example, a market research was not done. Instead, the values for the storage per fuel assembly in the spent fuel pool and for the unit volume of concrete used in the dry casks were varied and the algorithm was run several times. This was carried out as part of the sensitivity analysis presented in Section 4.

3.7. Optimization Algorithm. For the example, the final step of the methodology, which is the optimization algorithm execution, was done using the "Global Optimization" toolbox available in MATLAB® [20]. The chosen method was the Genetic Algorithm.

Genetic algorithms are inspired by the evolutionist theory, in which the stronger individuals have a better chance to pass on their genes through reproduction. Natural selection dictates which individuals' characteristics in one generation survive to the next. The two basic operators that create new solutions from the previous generation's solutions are crossover, in which two individuals' genes are combined to form new individuals; and mutation, that introduces diversity to the population and avoids premature convergence to an optimal solution that may not be the global one. The suitability of an individual solution to an objective function, called fitness, determines the probability that it survives to the next generation [21].

Functions to calculate the costs of the dry cask and the spent fuel pool, as well as for calculating the dose rates measured at the point located at 1 meter from cask surface location were coded. The fitness function to be minimized was defined as equal to the sum of the dry cask and pool costs and the dose rate function was used as a constraint for the algorithm.

4. Results and Discussion

To evaluate the behavior of the optimization algorithm, as well as the effects of changes in the input parameters of the problem on the algorithm's output, a simple sensitivity analysis was carried out. For this, the values for dose rate limits and unit prices for the storage per fuel assembly at the pool and cubic meter of concrete were varied in relation to each other.

Table 4 presents the sensitivity analysis for the Cesium-137 fraction of the source obtained from the Genetic Algorithm for a dose rate limit of 0.2 mSv/h and for a dose rate limit of 4 mSv/h. The unit prices are measured in Monetary Units (M.U.) and are displayed within a range where changes to the results could be observable. The parameters of the scenario and the simplifications made during the development of the example defined the range where these changes could be observable.

Analyzing the results, it is noticeable that, for the algorithm to work in a range where changes in the result can be observed, the value of a cubic meter of concrete must be high in relation to the storage cost of a fuel assembly in the pool. This is a consequence to the simplification of the dry cask model used for this example, as in a real design, there are other characteristics that depend on parameters of the spent fuel that vary with the initial cooling time, such as materials for neutron shielding and passive decay heat removal features.

Secondly, it is observed that the example scenario is much more sensible to changes in the concrete shielding thickness than it is to changes in initial cooling time, for example, an increase of 1 mm to shielding thickness has a larger impact on the measured dose rate than an increase of 12 months in initial cooling time. This can be explained by the choice of only using Cesium-137 as the source for this example, as this isotope has a long half-life (approximately 30 years), and changes in its activity are more noticeable at long term. Also, the higher the dose rate limit is, the smaller is the increment or decrease in shielding thickness necessary to compensate for changes in initial cooling time.

To observe how the algorithm behaves when a more diverse source term is present, a second sensitivity analysis was carried out using a source with the decay characteristics of Cesium-137 (i.e., one photon with energy of 0.6617 MeV) and the activity at various initial cooling times for the whole spent fuel isotopic composition obtained from (USNRC, 2015) [10]. This adaptation of the source does not have by any means the objective of representing the actual source inside a dry cask, but it is useful as a tool to evaluate the sensitivity of the optimization algorithm, as it has a steeper decrease curve than the source comprised solely of Cesium-137. Table 5 presents the activity values for different cooling times of this adapted source.

Table 6 presents the sensitivity analysis of the Genetic Algorithm using the adapted source for both 0.2 mSv/h and 4 mSv/h dose rate limits, once again presented at unit costs of fuel assembly and concrete unit costs intervals where changes in the algorithm output can be observed.

As can be observed, using the adapted source with a steeper activity decrease allowed for more noticeable changes in the results, i.e., longer initial cooling times allowed for larger decreases in shielding thickness in comparison to the Cesium-137 only source.

It also possible assess that the fitness function has many local minima that correspond to the points where the dose rate at the detector is closest to, but not greater than, the normative dose rate limit. What determines if one minimum is better than another is the relation between unit costs for spent fuel cost per fuel assembly and cubic meter of concrete.

Further data, such as dose rate at 1 m from the surface of the cask and minimal capacity needed for the spent fuel pool can then be obtained for the optimal values of a given scenario of dose rate limit, choice of source and unit costs for fuel assembly storage in the pool and cubic meter of concrete. For example, using the adapted source, the 4 mSv/h dose rate limit and unit costs of 25 M.U. for storage of fuel assemblies

Table 4: Sensitivity analysis for the optimization algorithm using Cesium-137 as the source.

Dose Rate Limit 0.2 mSv/h		Concrete cost per m^3 (M.U.) 100		1000		10000	
		Optimal Time (months)	Concrete Thickness (mm)	Optimal Time (months)	Concrete Thickness (mm)	Optimal Time (months)	Concrete Thickness (mm)
Pool cost per stored Fuel Assembly (M.U.)	1	13	299.660	720	298.034	720	298.034
	10	13	299.660	13	299.660	720	298.034
	20	13	299.660	13	299.660	720	298.034
	25	13	299.660	13	299.660	720	298.034
	26	13	299.660	13	299.660	13	299.660
	27	13	299.660	13	299.660	13	299.660
	28	13	299.660	13	299.660	13	299.660
	30	13	299.660	13	299.660	13	299.660
Dose Rate Limit 4 mSv/h		Concrete cost per m^3 (M.U.) 100		1000		10000	
		Optimal Time (months)	Concrete Thickness (mm)	Optimal Time (months)	Concrete Thickness (mm)	Optimal Time (months)	Concrete Thickness (mm)
Pool cost per stored Fuel Assembly (M.U.)	1	720	255.115	720	255.115	720	255.115
	10	13	287.635	720	255.115	720	255.115
	50	13	287.635	13	287.635	720	255.115
	100	13	287.635	13	287.635	720	255.115
	250	13	287.635	13	287.635	720	255.115
	500	13	287.635	13	287.635	13	287.635
	750	13	287.635	13	287.635	13	287.635
	1000	13	287.635	13	287.635	13	287.635

Table 5: Activity for all the isotopes in the spent fuel (adapted from [10]).

Initial Cooling Time	Activity per MTU (Ci/MTU)
5 hours	7.53E+07
1 day	5.61E+07
90 days	7.79E+06
1 year	2.98E+06
5 years	8.02E+05
10 years	5.56E+05
50 years	1.81E+05
100 years	5.81E+04
200 years	1.15E+04

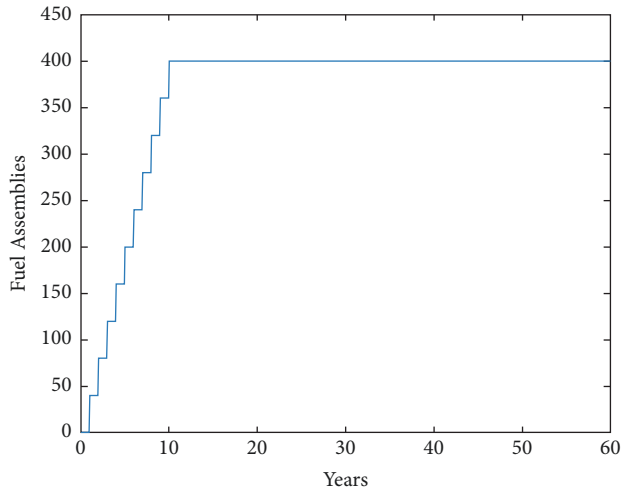

Figure 7: Spent fuel pool occupation for an optimal initial cooling time of 121 months and dose rate limit of 4 mSv/h.

and 10000 M.U. per cubic meter of concrete, we obtain the values presented in Table 7.

It is important to remember that these costs are the fraction of the cost that depends on the initial cooling time and that they do not include the costs that are constant in relation to that variable.

Figure 7 presents the occupation of the spent fuel pool for this scenario. In this case, the occupation of the pool is constant after reaching maximum capacity because the optimal cooling time of 121 months coincides with the scheduled month for refueling of the reactor, as expected. As such, the vacant racking space left by the fuel moved to the casks is immediately occupied by the fuel removed from the reactor and the technical parameters of the removed fuel assemblies are at their optimal values, within one cycle, for storage in the casks.

Finally, for purposes of comparison, Table 8 presents the optimal result data for the same unit cost values used in Table 7, but using instead the dose rate limit of 0.2 mSv/h. As expected, the overall costs increase in comparison to when the 4 mSv/h limit is applied.

The results obtained from the example show that, following the steps established by the methodology, the user can obtain the desired information, which is the optimal time, in relation to overall cost, to remove the spent fuel assemblies from the spent fuel pool and move them to dry casks as well as several data of great value for the designer of a new NPP.

5. Conclusions

This study had the purpose to establish a methodology for the optimization of the management of spent nuclear fuel assemblies. Some simplifications were necessary in order to present the example given, allowing for the development of the methodology utilizing the available resources.

It is not the intention of the authors that the results obtained from the presented example are directly applied to the design of an installation, but rather, to demonstrate the steps necessary for the application of the proposed methodology, with real data and more detailed models, to allow for the reduction of the initial investment of purchasing a new plant.

5.1. Limitation of the Study. Many uncertainties exist before the operation of a nuclear power plant. Political and financial decisions, as well as unforeseen events, such as accidents that alter the public perception of the use of nuclear energy, may result in the change of the fuel management policy adopted by any nation. Problems such as the lack of resources to acquire dry casks during the operation of the plant may cause the capacity of the spent fuel pool to be compromised, which in turn may demand that the plant is shut down until the problem is resolved. In the same manner, technological development may make dry cask design and manufacturing cheaper, making them more advantageous options than they were during the application of the methodology at the design stages of the power plant. The proposed methodology cannot foresee such issues and further studies might be needed to include an approach to address them.

The methodology also only deals with a scenario where a country opts for using dry casks as a solution for interim storage and does not apply to those countries that may choose to store their spent fuel in independent pools, limiting the scope of its application.

The adoption of the core Equilibrium Hypothesis might also limit the application of the proposed methodology as variations in the core configuration during the life span of the NPP can impair the results obtained by the optimization process. Further studies focused on this issue might also benefit and improve the methodology.

Further investigations include the refinement of the shielding and source models, including activated structural materials, decay heat analysis, and a detailed market research, with the contribution of specialists in the economic field, to obtain realistic values for the unit prices of the shielding materials and spent fuel pool construction, including their variation with time.

6. List of Symbols and Acronyms

BWR: Boiling Water Reactor.

Table 6: Sensitivity analysis for the optimization algorithm using the adapted source.

Dose Rate Limit 0.2 mSv/h		Concrete cost per m^3 (M.U.) 100		1000		5000	
		Optimal Time (months)	Concrete Thickness (mm)	Optimal Time (months)	Concrete Thickness (mm)	Optimal Time (months)	Concrete Thickness (mm)
Pool cost per stored Fuel Assembly (M.U.)	0.5	433	300.000	720	299.709	720	299.709
	1	433	300.000	601	299.788	720	299.709
	25	121	343.877	433	300.000	433	300.000
	50	61	360.956	433	300.000	433	300.000
	75	61	360.955	433	300.000	433	300.000
	100	13	389.405	433	300.000	433	300.000
	500	13	389.405	61	360.956	433	300.000
	1000	13	389.405	13	389.405	121	343.877
Dose Rate Limit 4 mSv/h		Concrete cost per m^3 (M.U.) 100		1000		5000	
		Optimal Time (months)	Concrete Thickness (mm)	Optimal Time (months)	Concrete Thickness (mm)	Optimal Time (months)	Concrete Thickness (mm)
Pool cost per stored Fuel Assembly (M.U.)	1	720	288.610	720	288.610	720	288.610
	10	13	299.670	720	288.610	720	288.610
	50	13	299.670	13	299.670	720	288.610
	75	13	299.670	13	299.670	613	290.050
	90	13	299.670	13	299.670	121	297.002
	100	13	299.670	13	299.670	61	298.003
	250	13	299.670	13	299.670	13	299.670
	200	13	299.670	13	299.670	13	299.670

Table 7: Optimal result data for a given set of example parameters with 4 mSv/h as the dose rate limit.

Source	Adapted
Dose Rate Limit	4 mSv/h
Cubic Meter of Concrete Unit Cost	5000 M.U.
Storage Cost per Fuel Assembly in the Pool	90 M.U.
Optimal Initial Cooling Time	121 months
Optimal Shielding Thickness	297.002 mm
Spent Fuel Pool Minimal Capacity	400 Fuel Assemblies
Spent Fuel Pool Cost	3600 M.U.
Dose Rate at 1 m from Cask Surface	4 mSv/h
Concrete Volume for Whole Cask Array	11.15 m^3
Cost of Whole Cask Array	6.9126 x 10^6 M.U.
Cost per Fuel Assembly Stored Dry	2787.33 M.U.

Table 8: Optimal result data for a given set of example parameters with 0.2 mSv/h as the dose rate limit.

Source	Adapted
Dose Rate Limit	0.2 mSv/h
Cubic Meter of Concrete Unit Cost	5000 M.U.
Storage Cost per Fuel Assembly in the Pool	90 M.U.
Optimal Initial Cooling Time	433 months
Optimal Shielding Thickness	300.000 mm
Spent Fuel Pool Minimal Capacity	1440 Fuel Assemblies
Spent Fuel Pool Cost	129,600 M.U.
Dose Rate at 1 m from Cask Surface	0.2 mSv/h
Concrete Volume for Whole Cask Array	11.24 m^3
Cost of Whole Cask Array	6.9703 x 10^6 M.U.
Cost per Fuel Assembly Stored Dry	2810.60 M.U.

$C(t)$: costs of management of spent fuel that depend on the initial cooling time t.

C_c: cost per unit volume of concrete.

C_{const}: costs that do not depend on the initial cooling time t.

C_{FA}: cost of storage per fuel assembly in the pool.

CFD: Computational Fluid Dynamics.

CFR: Code of Federal Regulations.

$C_{cask}(t)$: cost of one dry cask that is dependent on t.

$C_{sfp}(t)$: cost of spent fuel pool that is dependent on t.

$C_{total}(t)$: total cost of management of spent fuel.

h_{FA}: height of a fuel assembly.

HNPP: Hypothetical Nuclear Power Plant.

L_c: concrete shielding thickness.

L_{FA}: length of the side of a fuel assembly.

M.U.: Monetary Units.

MAVRIC: Monaco with Automated Variation Reduction using Importance Calculations.

$\max[N(t,T)]$: number of fuel assemblies in the pool at time T in function of t.

MCNP: Monte Carlo N-Particle.

MTU: Metric Ton of Uranium.

N_{cask}: total number of dry casks.

$N_{in}(t)$: number of fuel assemblies that are placed in the pool at time T.

$N_{out}(t)$: number of fuel assemblies that are removed from the pool at time T and in function of t.

NPP: Nuclear Power Plant.

NUREG: United States Nuclear Regulatory Commission Regulation.

PWR: Pressurized Water Reactor.

SAS4: Shielding Analysis Sequence 4.

t: initial spent fuel cooling time.

T: time from the beginning of the power plant operation.

UO_2: Uranium Dioxide.

US NRC: Unite States Nuclear Regulatory Commission.

V_s: volume of the source.

Data Availability

The MCNP simulated radiation dose data used to support the findings of this study are included within the article. The Spent Nuclear Fuel Assemblies Characteristics data supporting this study are from previously reported studies and datasets, which have been cited. The processed data are included within the article.

Conflicts of Interest

The authors declare that there are no conflicts of interest regarding the publication of this paper.

Acknowledgments

Ian B. Gomes received scholarship funding from the National Council for Scientific and Technological Development (CNPq), Process 141061/2013-8, from March 2013 to August 2014.

References

[1] "WNA. World Nuclear Association," World Nuclear Power Reactors & Uranium Requirements, 2018, http://www.world-nuclear.org/info/Facts-and-Figures/World-Nuclear-Power-Reactors-and-Uranium-Requirements/.

[2] K. Fukuda, W. Danker, J. S. Lee et al., "IAEA Overview of Global Spent Fuel Storage," in *Proceedings of the Storage of Spent Fuel from Power Reactors, 2003, Vienna. Conference & Symposium Papers*, pp. 3–11, IAEA, Vienna, Austria, 2003.

[3] P. Högselius, "Spent nuclear fuel policies in historical perspective: An international comparison," *Energy Policy*, vol. 37, no. 1, pp. 254–263, 2009.

[4] J. J. Laidler and J. C. Bresee, "The U.S. advanced fuel cycle initiative: development of separations technologies," in *Proceedings of the ATALANTE Conference*, p. 6, Nimes, France, 2004.

[5] "Committee on the safety and security of commercial spent nuclear fuel storage, board on radioactive waste management," in *National Research Council of the National Academies. Safety and Security of Commercial Spent Nuclear Fuel Storage*, p. 116, The National Academies Press, Washington, DC, USA, 2006.

[6] Y. Gao, C. R. Hughes, C. R. Greulich, J. E. Tulenko, A. Enqvist, and J. E. Baciak, "Radiation dose rate distributions of spent fuel dry casks estimated with MAVRIC based on detailed geometry and continuous-energy models," *Annals of Nuclear Energy, Gainesville*, vol. 117, pp. 84–97, 2018.

[7] IAEA. International Atomic Energy Agency, *Optimization Strategies for Cask Design and Container Loading in Long Term Spent Fuel Storage: IAEA-TECDOC-1523*, IAEA, Vienna, Austria, 2006.

[8] K. Y. Spencer, P. V. Tsvetkov, and J. J. Jarrell, "Optimization of dry cask loadings for used nuclear fuel management strategies," *Progress in Nuclear Energy*, vol. 108, pp. 11–25, 2018.

[9] A. Yamamoto and K. Kanda, "Comparison between equilibrium cycle and successive multicycle optimization methods for in-core fuel management of pressurized water reactors," *Journal of Nuclear Science and Technology*, vol. 34, no. 9, pp. 882–892, 1997.

[10] USNRC, "United States Nuclear Regulatory Commission," US Commercial Spent Nuclear Fuel Assembly Characteristics: 1968-2013: NUREG/CR-7227. Oak Ridge: Office of Nuclear Regulatory Research, p. 145, 2015.

[11] IAEA. International Atomic Energy Agency, *Operation and Maintenance of Spent Fuel Storage and Transportation Casks/ Containers: IAEA-TECDOC 1532*, IAEA, Vienna, Austria, 2007.

[12] A. Y. Chen, Y. F. Chen, J. N. Wang, R. J. Sheu, Y.-W. H. Liu, and S. H. Jiang, "A comparison of dose rate calculations for a spent fuel storage cask by using MCNP and SAS4," *Annals of Nuclear Energy*, vol. 35, no. 12, pp. 2296–2305, 2008.

[13] "TRANSUCLEAR INC., TN-32," Dry Storage Cask. Safety Analysis Report Final Safety Analysis Report, Rev. 2, 2002.

[14] USNRC, "United States Nuclear Regulatory Commission," Title 10 of the Code of Federal Regulations - PART 72 - Licensing Requirements for the Independent Storage of Spent Nuclear Fuel, High-Level Radioactive Waste, and Reactor-Relater Greater than Class C Waste, United States, 2017.

[15] USNRC. United States Nuclear Regulatory Commission, "Standard review plan for spent fuel dry storage systems at a general license facility," Tech. Rep. NUREG-1536, Office of Nuclear Material Safety and Safeguards, Oak Ridge,Tenn, USA, 2010.

[16] J. Li and Y. Y. Liu, "Thermal modeling of a vertical dry storage cask for used nuclear fuel," *Nuclear Engineering and Design*, vol. 301, pp. 74–88, 2016.

[17] HOLTEC, "Holtec International," Final Safety Analysis Report on the HI-STORM 100 Cask System. Marlton, 2010.

[18] X-5 MONTE CARLO TEAM. X-5 Monte Carlo Team, i. MCNP – Version 5, Vol. I: Overview and Theory. LA-UR-03-1987. United States, 2003.

[19] J. LEE, D.-H. Kim, and K.-S. Bang, "Thermal Analysis of a Storage Cask for 24 Spent PWR Fuel Assemblies," in *Proceedings of the International Symposium on the Packaging and Transportation of Radioactive Materials, 14*, Berlin, Germany, 2004, http://www.iaea.org/inis/collection/NCLCollectionStore/_Public/37/088/37088784.pdf.

[20] MATHWORKS, "The MathWorks, Inc," MATLAB, Version R2017b. Natick, 2017.

[21] A. Konak, D. W. Coit, and A. E. Smith, "Multi-objective optimizationusinggeneticalgorithms: A tutorial," *Reliability Engineering & System Safety*, vol. 91, no. 9, pp. 992–1007, 2006.

Hindawi
Science and Technology of Nuclear Installations
Volume 2019, Article ID 4936379, 10 pages
https://doi.org/10.1155/2019/4936379

Research Article

Effect of Fe_2O_3 on the Immobilization of High-Level Waste with Magnesium Potassium Phosphate Ceramic

Hailin Yang,[1,2] **Mingjiao Fu**,[3] **Bobo Wu**,[4] **Ying Zhang**,[2] **Ruhua Ma**,[2] **and Jueshi Qian**[1]

[1]*College of Materials Science and Engineering, Chongqing University, Chongqing 400045, China*
[2]*College of Environment and Resources, Chongqing Technology and Business University, Chongqing 400067, China*
[3]*Guizhou Aerospace XinLi Casting and Forging Co., LTD, Zunyi, Guizhou Province 563000, China*
[4]*Zunyi Transportation and Tourism Investment, Zunyi, Guizhou Province 563000, China*

Correspondence should be addressed to Hailin Yang; hailinyang@gmail.com

Received 28 September 2018; Accepted 30 December 2018; Published 3 February 2019

Guest Editor: Rema Abdulaziz

For the proposed novel procedure of immobilizing HLW with magnesium potassium phosphate cement (MKPC), Fe_2O_3 was added as a modifying agent to verify its effect on the solidification form and the immobilization of the radioactive nuclide. The results show that Fe_2O_3 is inert during the hydration reaction. It slows down the hydration reaction and lowers the heat release rate of the MKPC system, leading to a 3°C-5°C drop in the mixture temperature during hydration. Early comprehensive strength of Fe_2O_3 containing samples decreased slightly while the long-term strength remained unchanged. For the sintering process, Fe_2O_3 played a positive role, lowering the melting point and aiding the formation of ceramic structure. $CsFe(PO_4)_2$, or $CsFePO_4$, was generated by sintering at 900°C. These products together with the ceramic structure and absorption benefit the immobilization of Cs^+. The optimal sintering temperature for heat treatment is 900°C; it makes the solidification form a fired ceramic-like structure.

1. Introduction

The utilization of nuclear energy resulted in the accumulation of large amounts of liquid high-level radioactive waste (HLW) which contains environmentally hazardous elements like plutonium and other actinides in addition to fission and corrosion products [1]. Safe disposal of HLW is of key concern in the application of nuclear energy. The dominant technology for the solidification of HLW is vitrification. Generally, the technology of immobilizing HLW through vitrification does not ensure the complete immobilization of radionuclides due to the low hydrothermal stability of the glass produced [2]. In recent research, the incorporation of radionuclides into crystalline phases (pyrochlore, zircon, zirconolite, etc.) that are analogs to natural minerals and that have high radiation and chemical stability is considered as an alternative way for vitrification. Various methods were proposed for the preparation of mineral-like matrices, e.g., cold pressing and sintering or hot pressing or induction melting in a cold crucible [3]. As alternative materials for vitrification, various matrices were proposed for immobilization of HLW including hydrothermal synthetic rock [4–6], ceramics [2], and Portland cement [7].

Magnesium phosphate cements (MPCs) are cementitious materials that are formed through a solution acid-based reaction between dead burnt magnesia and phosphate. Retarder and mineral admixtures may be added during hydration reaction to achieve proper workability or specific properties [8–10]. Formed at ambient temperatures and exhibiting properties like ceramics, MPCs are also termed chemically bonded phosphate ceramics [11]. MPCs have several advantages over conventional Portland cement such as rapid setting time, high early strength, good bonding with Portland cement, little drying shrinkage, and better resistance to abrasion, etc. [12]. These superior properties lead MPCs to be widely used in various engineering structures, especially in emergency-repairing as well as in the solidification of hazardous materials [13].

Earlier MPCs featured a "two-part" system, consisting of dead burnt magnesia and a soluble orthophosphate, i.e., $NH_4H_2PO_4$ (ADP) or KH_2PO_4 (KDP) [14]. However, the hydration reaction is too fast to allow enough time for

operation. Subsequently, a "three-part" MPC system based on magnesium and phosphate was prepared with the addition of retarders [15]. The use of sodium triphosphate (STP), boric acid (H_3BO_3), or borax ($Na_2B_4O_7{\cdot}10H_2O$) as retarders has been reported in recent literature [16, 17]. Particularly, borax has been widely used in academic study and commercial application due to its easy storage and effectiveness [8].

Since the reaction between MgO and ADP releases ammonia, in consideration of the secondary pollution control, we prefer to adopt the magnesium potassium phosphate system as the raw material. The hydration reaction is governed by [18]

$$MgO + KH_2PO_4 + 5H_2O \longrightarrow MgKPO_4 \cdot 6H_2O \quad (1)$$

Nuclear reactors periodically unload spent fuel containing unburnt nuclear fuel, abundant fission fragments, and their decay products [19]. To achieve intensive utilization of limited uranium resources, spent fuel should be recycled by postprocessing such as PUREX [20]. Postprocessing discharges aqueous HLW that carries most of the radioactive activity and toxicity from the spent fuel, making aqueous HLW the most important radioactive waste that needs to be handled.

As shown in the reaction equations, aqueous HLW could be directly immobilized by the introduction of binding agents. The cement-like solidification process is characterized by its low energy inputs, the simplicity of realization, as well as the minimization of secondary radioactive waste, and the low mobility of the nuclide ion. Compared to conventional cementation, MKPC has perceptible advantages: possibility of solidifying liquid wastes within a wide range of pH, high loading capacity toward HLW, etc. Interest in the use of binding phosphate materials for radioactive waste immobilization has risen during last few years. Singh et al. investigated immobilizing ^{99}Tc with MKPC Ceramicrete. The solidified form was achieved and had a comprehensive strength no less than 30 MPa. The solidification mechanism of ^{99}Tc was proven to be the combination of mechanical enclosing and chemosetting [21]. Vinokurov et al. studied to solidify simulated HLW with MPC at ambient temperatures. Results show that the density of solidified form is 1.7 g/cm^3 while its comprehensive strength exceeds 20 MPa. The leaching resistance conforms to relevant standards [1]. Wagh et al. attempted to solidify radioactive waste containing Pu with MPC. Pu^{3+} was translated into Pu^{4+} (Insoluble oxide) first to reduce the solubility and then achieve better immobilization. Testing shows that Pu^{4+} was well immobilized through both the chemical stabilization and the physical encapsulation [22, 23].

Scientists of ANL (USA) offered the use of phosphate materials (Ceramicrete) for immobilization of low-level and technetium-containing simulant waste solutions as well as for incorporation of Pu-containing ash. At the Khlopin Radium Institute (Russia) and INEEL (USA), the possibility of incorporating a simulant of low-level ash remainder of combustible radioactive waste into iron phosphate matrices was also studied [1].

In our previous study, a novel procedure of HLW immobilization was developed in which the liquid HLW was added as a substitute for the mixing water of the MKPC system. This procedure makes the processing very simple and direct. The solidified form has advantages over glass solidification or synroc solidification in terms of chemical stability and heat resistance, etc. Further study showed that the MKPC solidification form has good thermal resistance; it keeps intact even after sintering at 1400°C for hours, and the sintering makes MKPC form into real fire ceramics. In consideration of the heat releasing of the HLW, the MKPC form needs to withstand quite high temperatures after the HLW disposal. So, we believe that the presintering is beneficial for the durability and stability of the solidified forms as well as for the immobilization of the nuclide.

Iron phosphate has been proven to be appropriate for hazardous material immobilization. Sales, B. C. et al. reported that the lead-iron phosphates glass performs well as stable storage of high-level nuclear waste [24]. Greaves, G. N. et al. added iron oxide to prepare lead-iron-phosphate glasses and to achieve more stable structure [25]. Mechanically, iron ions can enter the network structure of phosphate, Fe^{3+}, and replace P^{5+} because of its stronger electro-positivity, thus forming a Fe - O - P bond which has better water resistance. Furthermore, the smaller radius of the iron ion (Fe^{3+}, Fe^{2+}) can hinder the larger water module from passing through the solidification form, therefore, significantly improving the chemical stability of immobilization matrix [26, 27].

Iron oxide is one of the most abundant metal oxides on earth. Its abundant and inexpensive characteristics make it a promising candidate to partially replace the magnesium for forming phosphate cements. It is meaningful to investigate the effect of fe_2o_3 on the immobilization of aqueous high-level waste with magnesium potassium phosphate ceramic. An experimental study was carried out in this paper to verify the function of the iron oxide in both the hydration reaction and the sintering process of the MKPC matrix.

2. Materials and Experiments

2.1. Materials. The magnesium potassium phosphate cement paste was prepared through a mixture of dead burnt magnesium oxide (MgO), acidic phosphate (KDP), and borax in specific proportions. The chemical characteristics of the raw materials are listed in Table 1.

The aqueous HLW considered in this study is the effluent of spent fuel postprocessing. During the postprocessing procedure, the spent fuel from the nuclear power reactor is mechanically cut and then dissolved in nitric acid. The solution is then filtered and clarified, and residual U and Pu are extracted for recycling by extraction agents, e.g., TBP. The aqueous HLW is discharged by spent fuel recycling and posttreatment processes. Generally, it is a mixture of concentrated nitric acid and various kinds of nitrate solution that contain the majority of the radiation and toxicity of the spent fuel. Due to the safety considerations and experimental conditions, a simulated aqueous HLW was used to represent the nuclear power reactor aqueous HLW. Cations were introduced into nitric acid by corresponding nitrate. Nuclides

Table 1: Characteristics of raw materials.

Component	Characteristics	Supplier
Dead burnt magnesium oxide powder (MgO)	Industrial grade, >95% MgO	Liaoning Xinrong Mining Group Co. Ltd., China
KDP (KH_2PO_4)	Industrial grade, >98% KDP	Qingzhou Guanghui Chemical Plant Co. Ltd, China
Borax ($Na_2B_4O_7{\cdot}10H_2O$)	Industrial grade, >95% borax	Tibet Pengdu Boron Industry Co. Ltd., China

Table 2: Composition of typical power nuclear reactor aqueous HLW (g/L) [28].

Al^{3+}	Ba^{2+}	Cr^{3+}	Fe^{3+}	K^{+}	Na^{+}	Cs^{+}	Ni^{2+}	Sr^{2+}	Mo^{6+}	Ce^{3+}	Nd^{3+}
15.9	0.074	2	17.4	0.45	51.2	2	8.2	0.61	0.82	0.78	2.05

[a] C_{HNO3}=2.6 mol/L.

Table 3: Basic formula of MKPC.

Component	MgO	KDP	Borax	Water
Ratio	100	25	12	16

were represented by their nonradioactive isotopes. We believe this is appropriate in chemical view. The simulated aqueous HLW was prepared according to the composition listed in Table 2.

$K_3PO_4{\cdot}7H_2O$ was introduced into aqueous HLW to adjust the pH value in advance. Fe_2O_3 powder was mixed with MgO homogeneously as an additive. All above-mentioned chemicals are analytically graded products.

2.2. Experiments. Solidified blocks were prepared through the following steps. (1) Add $K_3PO_4{\cdot}7H_2O$ into aqueous HLW to adjust pH to the specific value. (2) Add KDP and Borax into the liquid HLW at specific proportion and stir to make the liquid (solution and sediment) a homogeneous mixture. (3) Add mixture of MgO and Fe_2O_3 into the liquid and stir the hydration reaction. Pour the paste into cubic mold when the flowability is appropriate. (4) Vibrate by hand, use glass rod to densify paste, and avoid the opening. (5) Cure at ambient room temperature for hours. (6) Remove mold and retrieve blocks for further processing and study. (7) After ambiently curing for 7 days, the solidification forms were sintered for 2 hours at specific temperature in a muffle furnace. Heating rate of the muffle furnace was set to 5°C/min.

The basic formula of MKPC was listed in Table 3.

Hydration heat release was tested by an eight-channel micro calorimeter (Thermonetrics TAMair). The compressive strength of the hardened blocks was measured according to the standard of *method of testing cement-determination of strength* (idt ISO 679:1989). The strength of the samples at the ages of 1 h, 3 h, 1 day, 3 days, and 7 days was tested. To assure the reproducibility of experimental results, at least three replicates of specimens from each set were prepared and tested under the same conditions. The adiabatic temperature curve of the hydration reaction was recorded by an automatic temperature recorder that was dipped into the mixture while the mixture was placed into a vacuum cup. The leaching behavior of the most important nuclide, i.e., cesium, was tested according to the static immersion method of MCC-1 [29] using deionized water as the leachant and leaching at 40°C. The concentration of the Cs^{+} in the leachant was analyzed by flame atomic absorption spectrophotometer (TAS-990). The reaction product of MPC and liquid HLW were analyzed by X-ray diffraction (XRD, Panalytical xpert Powder) with a 2θ scanning rate of 0.5°/min. The microstructure and morphology of the blocks were observed by scanning electron microscopy (SEM, Hitachi 1050).

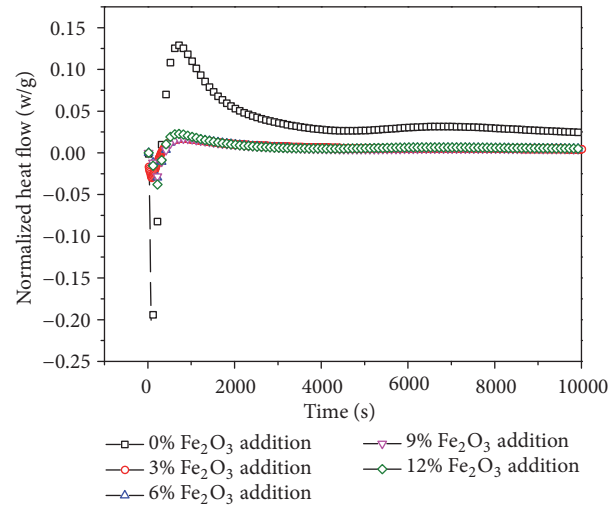

Figure 1: Exothermic curve of the mixture during hydration.

3. Results and Discussion

3.1. Effect on MKPC Systems. Fe_2O_3 was added at a dosage series of 0%, 3%, 6%, 9%, and 12% (wt% of MgO to replace MgO) to investigate the effect on MKPC hydration.

The exothermic curve of the mixture during hydration can be seen in Figure 1. The hydration heat release curve of the original MKPC has an endothermic valley and two exothermic peaks. The endothermic valley is because of the heat absorption of monopotassium phosphate's dissolution. MgO's dissolution in an acid solution as well as the hydration reaction release heat to make up the two exothermic peaks.

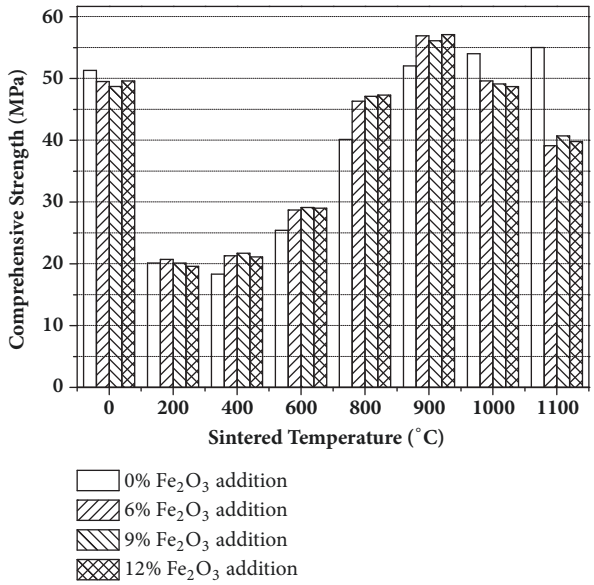

Figure 2: Comprehensive strength.

Endothermic valley keeps the same after the addition of Fe_2O_3, for the dissolution of monopotassium phosphate keeps unchanged. The addition of Fe_2O_3 reduced the heat release rate of the hydration reaction thus nearly flattening the second exothermic peak. Although Fe_2O_3 also meets the same requirements as MgO of 2n (pH) ≥pKsp to prompt the hydration reaction [30], its dissolution rate is much lower than MgO in an acid solution at room temperature. Thus, the addition of Fe_2O_3 substituted part of MgO and played the role of inert matter, resulting in a slower reaction rate and less hydration heat release rate because of the reduction of active substance, i.e., the MgO. Fe_2O_3 prolonged the setting time and lowered the exothermic curve dramatically while the overall heat releasing just changed slightly because of the reduction of MgO.

Fe_2O_3 was added at a dosage series of 0%, 6%, 9%, and 12% (wt% of MgO to replace MgO) to investigate the effect on mechanical property. Samples of the original MKPC and the sintered MKPC were tested for comprehensive strength (Figure 2). The basic result is that the addition of Fe_2O_3 does not reform the mechanical property of original MKPC remarkably. The comprehensive strength of the original samples even dropped with the addition of Fe_2O_3. Sintering at no more than 800°C weakened the comprehensive strength of samples. This is due to the sintering destroying the original structure, but not leading to a solid melting reaction due to the temperature not being high enough. Sintering at 900°C hardened the samples because of the melting reaction forming ceramic microstructure. 1000°C and 1100°C sintering hardened the original sample while weakening the Fe_2O_3 containing samples. Both the original and Fe_2O_3 containing samples were macroscopically destroyed by 1200°C sintering. The addition of Fe_2O_3 hardened the sintered samples at a temperature range of no more than 900°C while its effect was negative for the original samples. The proposed mechanism is that Fe_2O_3 is inert matter for the hydration reaction, but it lowers the melting temperature of system remarkably. When considering sintering in the whole immobilization process, Fe_2O_3 does benefit the mechanical property of the MKPC solidification form.

3.2. Effect on HLW Immobilization. Aqueous HLW was used to substitute mixing water completely in the proposed immobilization procedure. Since liquid HLW is a very concentrated acid liquor (pH<1), it may degrade the cement system and lead to failure of the immobilization. So the liquid HLW was treated in advance to adjust its pH value. $K_3PO_4{\cdot}7H_2O$ was used as buffer agent since its solution is alkalic and the introduction of $K_3PO_4{\cdot}7H_2O$ does not bring in extra elements. The neutralization reaction produces the sediment nuclide phosphate, which is more stable than hydroxide. Thus, the pretreatment benefits immobilization and eliminates the negative effect of nitric acid.

HLW was pretreated to specific pH (3, 5, 7) and then incorporated into the MKPC system mix water to form solidification blocks. Original samples and samples containing 9% Fe_2O_3 were tested to find the effect of Fe_2O_3 on the immobilization form.

As can be seen in Figure 3, comprehensive strength test indicated that the addition of Fe_2O_3 reduced early strength (age < 1 d) dramatically while the long-term strength was almost the same as original solidification forms at all pH levels. This is due to the fact that Fe_2O_3 substituted MgO as an inert matter and then reduced the generation of the K-struct struvite, i.e., $MgKPO_4{\cdot}6H_2O$. At the same time, it slowed down the hydration reaction. Both effects harmed the early strength. Long-term strength stood unchanged because the dosage of Fe_2O_3 was relatively low overall. Samples were sintered at 800°C, 900°C, and 1000°C to see the effect of Fe_2O_3 on sintering. The findings verified that the introduction of Fe_2O_3 lowered the melting temperature of system and reinforced the structure when sintered below 1000°C. This benefitted the sintering process through easier melting reaction and the forming of ceramic structure.

The adiabatic temperature curve of the hydration reaction was plotted. As seen in Figure 4, the curve of the Fe_2O_3 contained samples is lower and smoother than the Fe_2O_3 free samples. This indicates that at all pH levels (3, 5, 7), the introduction of Fe_2O_3 slowed down the heat release rate and lowered the equilibrium temperature and delayed the emergence of thermal balance. A reasonable explanation is that the partial substitution of MgO by Fe_2O_3 resulted in the reduction of reactant, therefore slowing down the hydration reaction. This explanation is also proven by chemical phase analysis.

The unsintered solidification form and the solidification form sintering at 900°C were prepared and analyzed by XRD. For the XRD spectrum, see Figure 5. HLW was pretreated to different pH levels (3,5,7) before mixing with the MKPC matrix. The XRD spectrum of the unsintered samples demonstrated that the iron phase shows as Fe_2O_3 and FeO·OH. This demonstrates that Fe_2O_3 is really an inert matter for hydration reaction. As to FeO·OH, it is the product of Fe_2O_3 in an alkaline environment, since MgO is superfluous according to the reaction formula and the basic

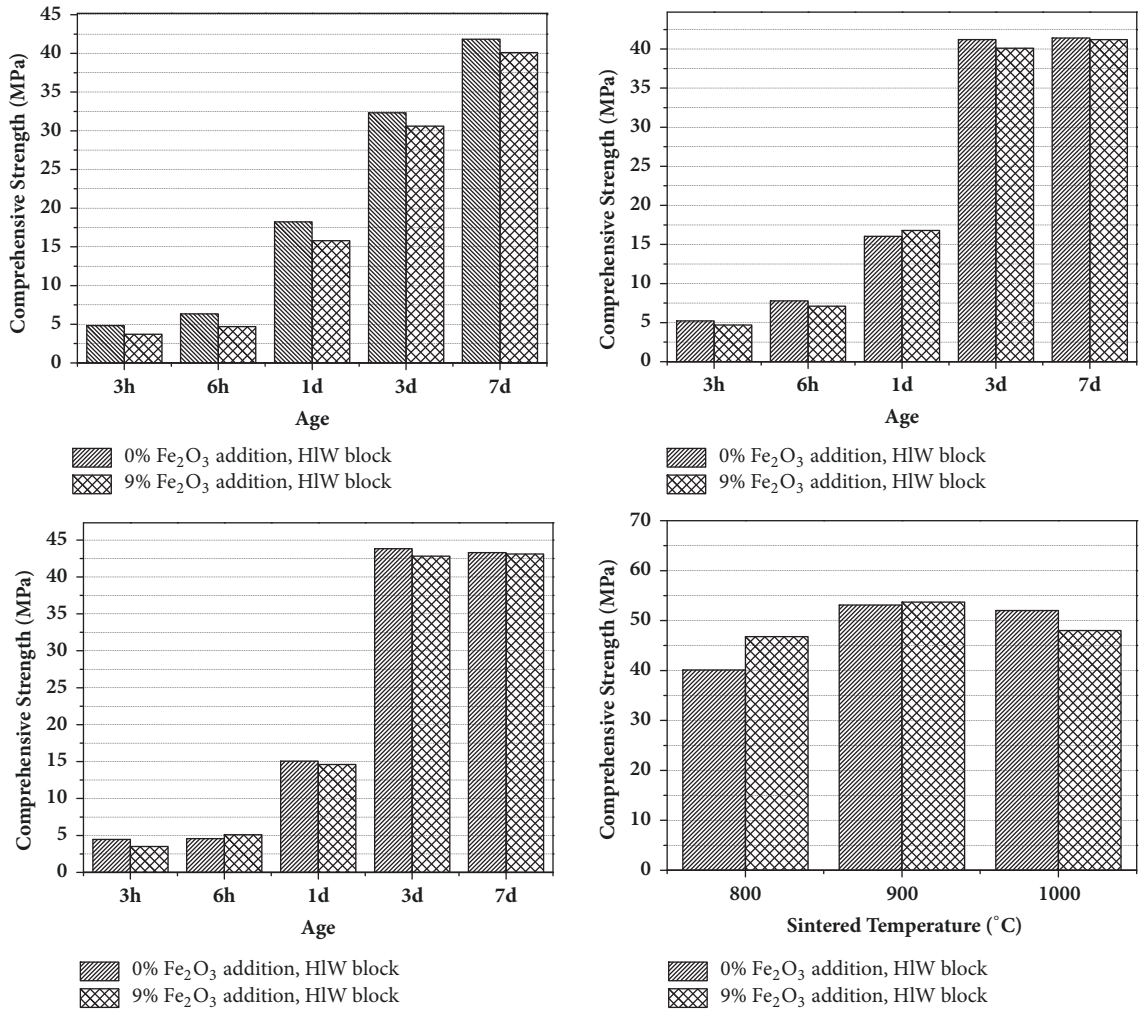

Figure 3: Comprehensive strength of solidification forms. ①HLW pH=3, ②HLW pH=5, ③HLW pH=7, ④HLW pH=5, sintered samples.

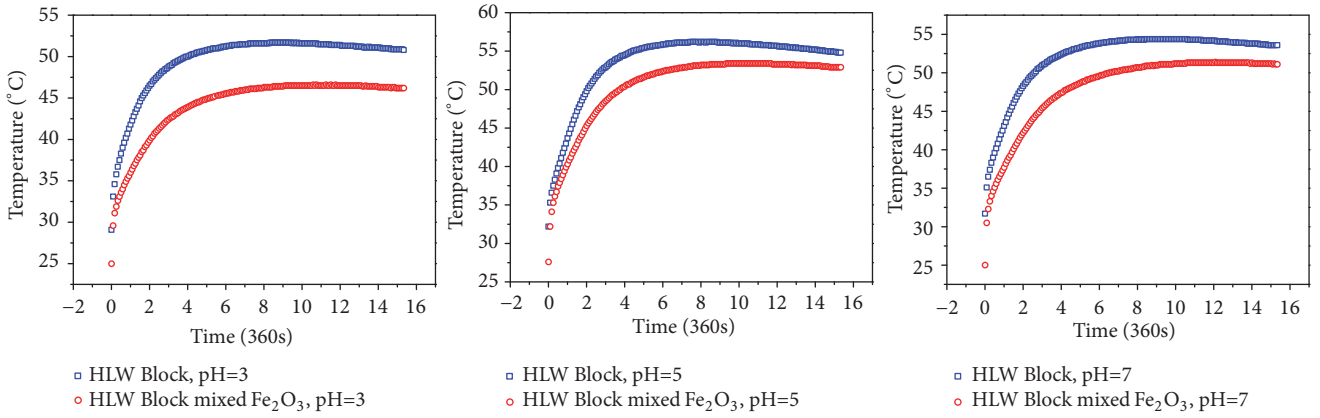

Figure 4: Adiabatic temperature curve (Fe_2O_3 dosage=9%).

matrix formula. Fe_2O_3 keeps stable at quite wide pH range. After sintering at 900°C, the characteristic diffraction peak of Fe_2O_3 and FeO·OH at the position of 2θ=21°, 2θ=34°, and 2θ=36° almost disappeared, indicating that Fe_2O_3 reacted with other constituents in the process of sintering. The HLW pH=3 diffraction peak of Fe_2O_3 is very similar to the Fe_2O_3-free samples, indicating that the addition of Fe_2O_3 barely altered the chemical phase of the solidification form. When dpH=5, the diffraction peak of $CePO_4$ moved right. A little isometric system of $CePO_4$ phase showed beside this trigonal

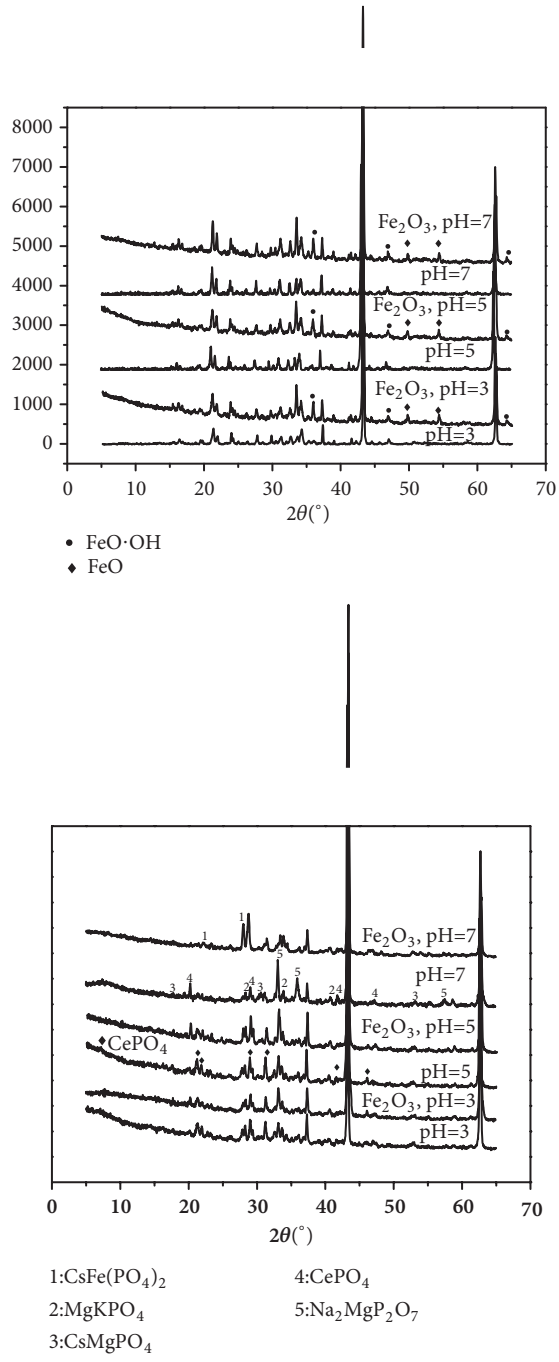

Figure 5: XRD spectrum of solidification forms (①unsintered, ②sintered at 900°C).

system. The crystallinity of the form improved. Conclusions can be drawn that the addition of Fe_2O_3 lowered the melting temperature thus producing more liquid phase at same sintering temperature benefitting the formation of ceramic structure. When pH=7, the chemical phase constitution changed dramatically. The diffraction peak at 2θ=30° rose remarkably while a new diffraction peak appeared at 2θ=20°. The new peak is verified to be $CsFe(PO_4)_2$ according to Jade software analysis.

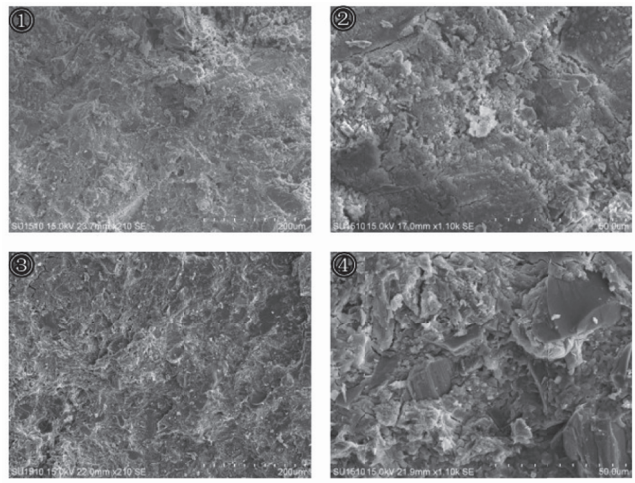

Figure 6: SEM photo of unsintered samples (HLW pH=3, ①②Fe_2O_3 free, ③④9% Fe_2O_3 addition).

In order to investigate the effect on the microstructure of the solidification form, HLW was pretreated to specific pH levels and incorporated in the MKPC matrix. The original form and Fe_2O_3 containing samples were prepared. All sample series were sintered at 900°C and compared with unsintered samples. SEM photos were taken and compared.

When HLW pH=3, the microstructure is mainly a small particle, and the crystal is underdeveloped because of the rapid hydration reaction (①② in Figure 6). Plate column and layered structure can be seen in microstructure of the Fe_2O_3 containing samples (③④ in Figure 6). As Fe_2O_3 is an inert matter, its addition reduced the content of reactant, i.e., MgO, thus slowing down the hydration reaction, making the crystal better developed and forming the plate column and layered structure.

When HLW pH=5, the crystal developed into a bigger formation. The reason is that free H^+ gets less, slowing down the reaction. The prolonged setting time makes better developed crystal (①② in Figure 7). For the Fe_2O_3 containing samples, the crystal size is smaller and mainly layered in structure, and the appearance of Fe_2O_3 reduced the production of the K-struct struvite for it is an inert matter (③④ in Figure 7).

When HLW pH=7, the crystal agglomeration region did not show on the vision field. The solidification form developed into a bigger compact plate structure. The bigger compact plate structure is a result of enough setting time for the production of K-struct struvite. The pH=7 environmentally lessens the free H^+ and benefits the crystal growth (①② in Figure 8). For Fe_2O_3 containing samples, the microstructure is compact and shown as lamellar structure (③④ in Figure 8).

As to all samples that sintered at 900°C, the microstructures present for the fire ceramic-like structure are all very compacted without visible pores (Figures 9, 10, and 11). When the HLW pH=3, Fe_2O_3 containing samples are more compacted than the Fe_2O_3 free ones, and the appearance of the iron phase lowered the melting temperature and generated more liquid phase to from ceramic structure.

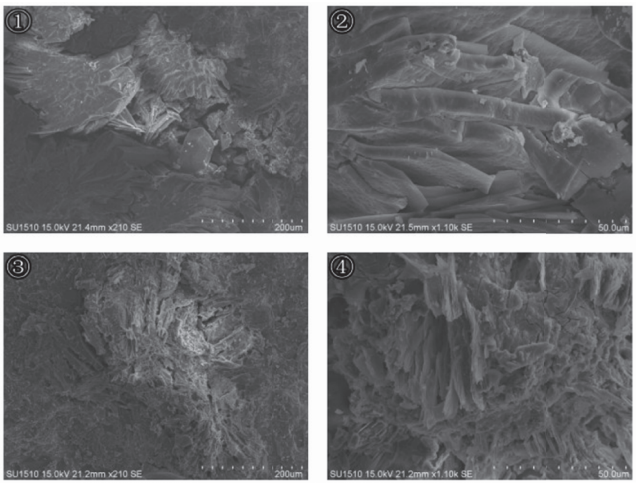

Figure 7: SEM photo of unsintered samples (HLW pH=5, ①②Fe_2O_3 free, ③④9% Fe_2O_3 addition).

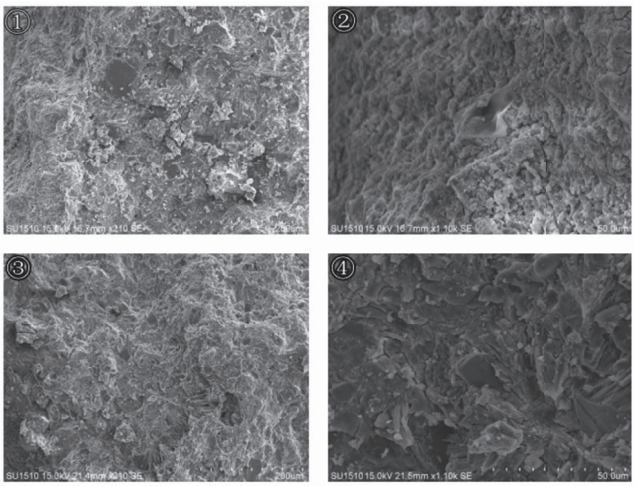

Figure 8: SEM photo of unsintered samples (HLW pH=7, ①②Fe_2O_3 free, ③④9% Fe_2O_3 addition).

When HLW pH=5, the microstructure of Fe_2O_3 containing samples interspersed with the column crystal. This deserves further investigation. When HLW pH=7, crystal grows well in Fe_2O_3-free samples, but the melting and resolidification works poorly during sintering; the microstructure is more granular. On the contrary, Fe_2O_3 containing samples show more compacted ceramic structure because of the better melting and reintegration. This is helpful for immobilization of radioactive nuclides.

According to mechanism research, immobilization of Cs^+ with MKPC system mainly depends on the following reactions. (a)Cs^+ replaces the metal ion with minor radius thus entering the crystal lattice. (b)Cs^+ is absorbed by metal phosphate. Cs^+ leaching behavior of samples containing free Fe_2O_3 and Fe_2O_3 as well as sintered and unsintered samples was tested according to the MCC-1 method. HLW was pretreated to a specific pH (3,5,7) first before being incorporated in. For the leaching rate of Cs^+, see Figure 12.

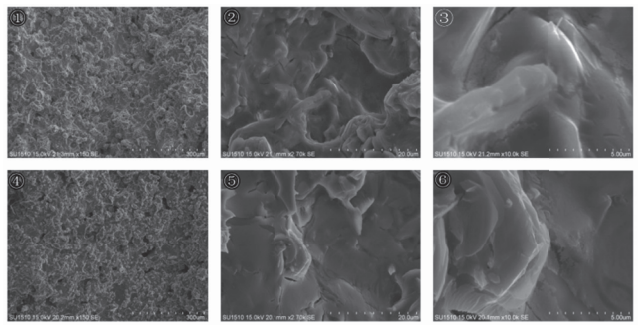

Figure 9: SEM photo of 900°C sintered samples (HLW pH=3, ①②③Fe_2O_3 free, ④⑤⑥9% Fe_2O_3 addition).

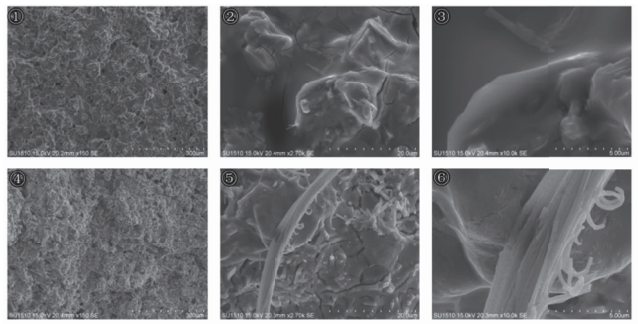

Figure 10: SEM photo of 900°C sintered samples (HLW pH=5, ①②③Fe_2O_3 free, ④⑤⑥9% Fe_2O_3 addition).

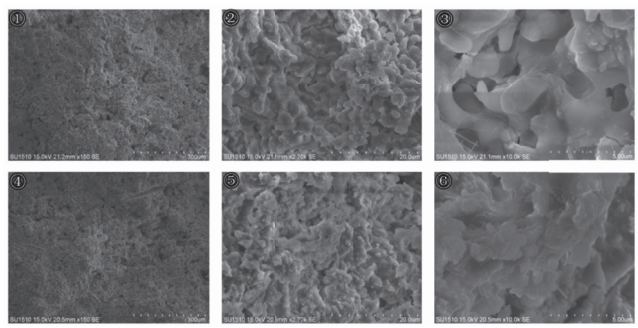

Figure 11: SEM photo of 900°C sintered samples (HLW pH=7, ①②③Fe_2O_3 free, ④⑤⑥9% Fe_2O_3 addition).

For unsintered samples, the addition of Fe_2O_3 lowered the leaching rate slightly while the variation tendency stayed the same with the Fe_2O_3 free samples, which is why the leaching rate of Cs^+ is lower in higher HLW pH value. In an acidic environment, free H^+ makes the MgO dissolve faster and thus sped up the hydration reaction. This makes Fe_2O_3 have fewer chances for entering the crystal lattice or for being absorbed. Thus, harming the immobilization of Cs^+ and making it escape easily from the solidification form. Addition of Fe_2O_3 makes the form more compacted because of the accumulation of its particles. Denser structure prevents the flushing out of the Cs^+.

For sintered samples, sintering at 900°C makes the solidification form a fire ceramic structure. Cs^+ replaces

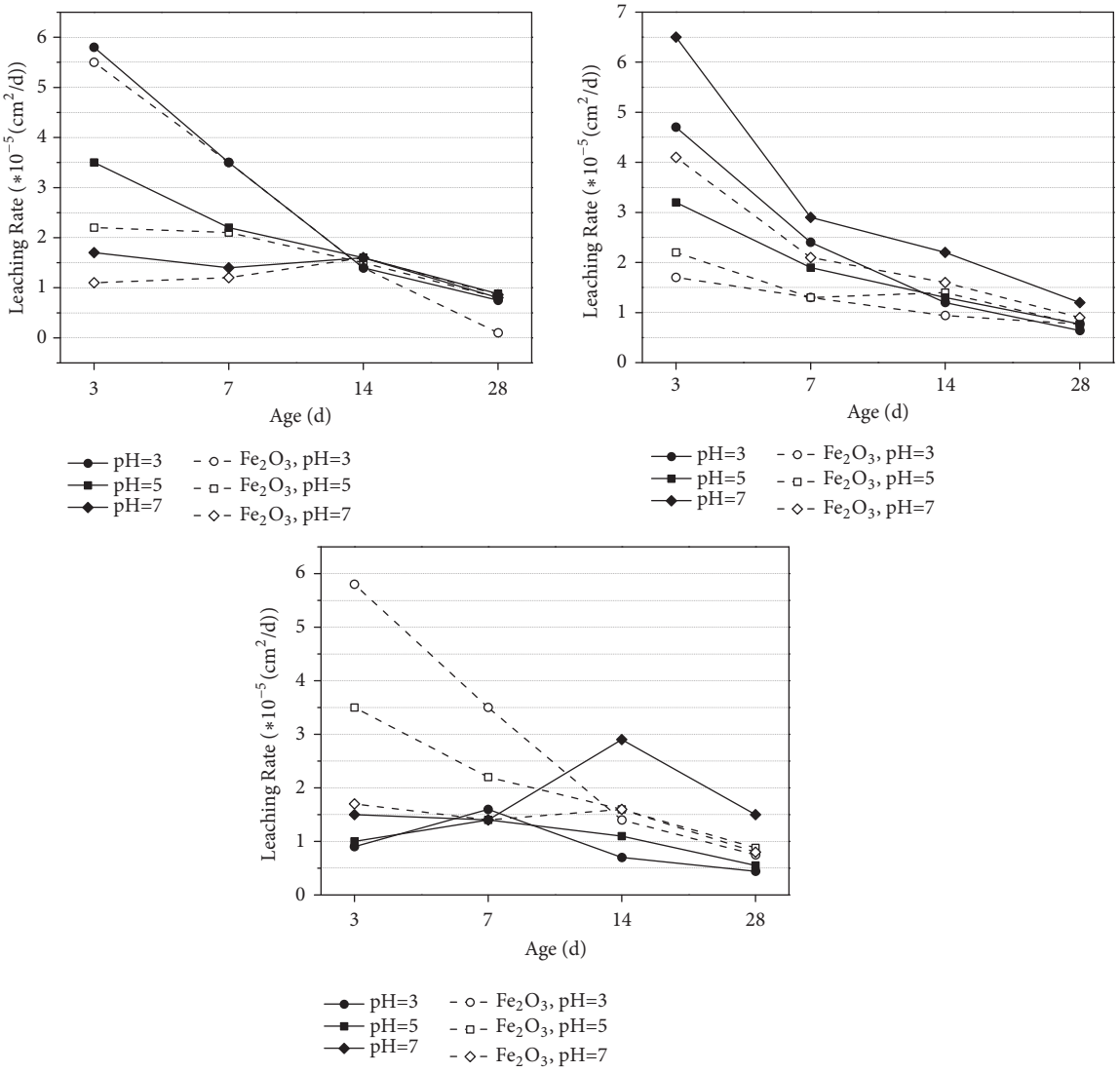

Figure 12: Leaching rate of Cs^+ (①unsintered samples, ② 900°C sintered samples, ③1000°C sintered samples).

K^+ and forms $MgCsPO_4$ and $CsFePO_4$ both of which have better water resistance. The addition of Fe_2O_3 lowered the leaching rate significantly since it lowered the melting point and helped the formation of ceramic.

Sintering at 1000°C cut the Cs^+ leaching rate of Fe_2O_3 free samples but improved the Cs^+ leaching rate of Fe_2O_3 containing samples dramatically. This again proved that the addition of Fe_2O_3 lowered the melting point, destroying Fe_2O_3 containing samples in the 1000°C sintering, and Cs^+ was leached out easily because of the failure of encapsulation and absorption.

4. Conclusions

As an additive for the novel procedure of HLW immobilization, in which the liquid HLW was added to substitute mixing water of the magnesium potassium phosphate cement system, the effect of Fe_2O_3 can be concluded as follows.

Addition of Fe_2O_3 lowers the heat release rate of the hydration reaction significantly, thus lowering the temperature of the mixture during hydration, while not harming the comprehensive strength of the test blocks.

Fe_2O_3 increases the compactness of the samples due to the accumulation of particles. For sintered samples, the existence of Fe_2O_3 lowers the melting point and generates more liquid phase in the sintering; this lowers the firing temperature effectively.

Fe_2O_3 is an inert matter for the hydration reaction, but it plays a positive role in sintering process. It lowers the melting point and helps the formation of ceramic structure. The sintering process produces $CsFe(PO_4)_2$ and immobile Cs^+ more effectively.

When taking its cheap price and remarkable availability into consideration, Fe_2O_3 may play an important role as an additive in the application of HLW immobilization with MKPC.

Data Availability

The raw/processed data required to reproduce these findings cannot be shared at this time due to technical or time limitations.

Conflicts of Interest

The authors declare that all received funding in the "Acknowledgments" section did not lead to any conflicts of interest, and there are no other possible conflicts of interest in the article.

Acknowledgments

The authors would like to acknowledge the financial support listed: International Cooperation Project of National Nature Science Fund of China, Grant No. 0211002321124; Chongqing Municipal Education Commission Science and Technology Planning Project, Grant No. KJ1600636; Student Science and Technology Innovation Fund of Chongqing Technology and Business University, Grant No. 173018; Environmental Pollution Control Team Fund of Environment and Resources College, CTBU.

References

[1] S. E. Vinokurov, Y. M. Kulyako, O. M. Slyuntchev, S. I. Rovny, and B. F. Myasoedov, "Low-temperature immobilization of actinides and other components of high-level waste in magnesium potassium phosphate matrices," *Journal of Nuclear Materials*, vol. 385, no. 1, pp. 189–192, 2009.

[2] I. W. Donald, B. L. Metcalfe, and R. N. J. Taylor, "The immobilization of high level radioactive wastes using ceramics and glasses," *Journal of Materials Science*, vol. 32, no. 22, pp. 5851–5887, 1997.

[3] W. E. Lee, M. I. Ojovan, M. C. Stennett, and N. C. Hyatt, "Immobilisation of radioactive waste in glasses, glass composite materials and ceramics," *Advances in Applied Ceramics*, vol. 105, no. 1, pp. 3–12, 2006.

[4] N. Yamasaki, K. Yanagisawa, S. Kanahara, M. Nishioka, K. Matsuok, and J. Yamazaki, "Immobilization of radioactive wastes in hydrothermal synthetic rock: Lithification of silica powder," *Journal of Nuclear Science and Technology*, vol. 21, no. 1, pp. 71–73, 1984.

[5] N. Yamasaki, K. Yanagisawa, S. Kanahara, M. Nishioka, K. Matsuoka, and J. Yamazaki, "Immobilization of Radioactive Wastes in Hydrothermal Synthetic Rock," in *Hydrothermal Reactions for Materials Science and Engineering: An Overview of Research*, S. Sōmiya, Ed., pp. 348–350, Springer, Dordrecht, Netherlands, 1989.

[6] A. Ringwood, "Immobilization of Radioactive Wastes in SYNROC: A high-performance titanate ceramic waste form composed of minerals that have survived in various natural environments for long periods, SYNROC should permit safe burial of waste in deep drill holes," *American Scientist*, vol. 70, no. 2, pp. 201–207, 1982.

[7] M. Atkins and F. P. Glasser, "Application of portland cement-based materials to radioactive waste immobilization," *Waste Management*, vol. 12, no. 2-3, pp. 105–131, 1992.

[8] N. Liu and B. Chen, "Experimental research on magnesium phosphate cements containing alumina," *Construction and Building Materials*, vol. 121, pp. 354–360, 2016.

[9] B. Kanter, A. Vikman, T. Brückner, M. Schamel, U. Gbureck, and A. Ignatius, "Bone regeneration capacity of magnesium phosphate cements in a large animal model," *Acta Biomaterialia*, vol. 69, pp. 352–361, 2018.

[10] X. Lu and B. Chen, "Experimental study of magnesium phosphate cements modified by metakaolin," *Construction and Building Materials*, vol. 123, pp. 719–726, 2016.

[11] Y. Li, W. Bai, and T. Shi, "A study of the bonding performance of magnesium phosphate cement on mortar and concrete," *Construction and Building Materials*, vol. 142, pp. 459–468, 2017.

[12] Y. Li and B. Chen, "Factors that affect the properties of magnesium phosphate cement," *Construction and Building Materials*, vol. 47, pp. 977–983, 2013.

[13] Y.-S. Wang, J.-G. Dai, L. Wang, D. C. W. Tsang, and C. S. Poon, "Influence of lead on stabilization/solidification by ordinary Portland cement and magnesium phosphate cement," *Chemosphere*, vol. 190, pp. 90–96, 2018.

[14] T. Sugama and L. E. Kukacka, "Magnesium monophosphate cements derived from diammonium phosphate solutions," *Cement and Concrete Research*, vol. 13, no. 3, pp. 407–416, 1983.

[15] D. A. Hall, R. Stevens, and B. El-Jazairi, "The effect of retarders on the microstructure and mechanical properties of magnesia-phosphate cement mortar," *Cement and Concrete Research*, vol. 31, no. 3, pp. 455–465, 2001.

[16] B. Rentsch, A. Bernhardt, A. Henß et al., "Trivalent chromium incorporated in a crystalline calcium phosphate matrix accelerates materials degradation and bone formation in vivo," *Acta Biomaterialia*, vol. 69, pp. 332–341, 2018.

[17] M. Ltifi, A. Guefrech, and P. Mounanga, "Effects of sodium tripolyphosphate addition on early-age physico-chemical properties of cement pastes," *Procedia Engineering*, vol. 10, pp. 1457–1462, 2011.

[18] E. Soudée and J. Péra, "Mechanism of setting reaction in magnesia-phosphate cements," *Cement and Concrete Research*, vol. 30, no. 2, pp. 315–321, 2000.

[19] R. C. Ewing, W. J. Weber, and F. W. Clinard Jr., "Radiation effects in nuclear waste forms for high-level radioactive waste," *Progress in Nuclear Energy*, vol. 29, no. 2, pp. 63–127, 1995.

[20] J. M. Mckibben, "Chemistty of the Purex Process," *Radiochimica Acta*, vol. 36, no. 1-2, 1984.

[21] D. Singh, V. R. Mandalika, S. J. Parulekar, and A. S. Wagh, "Magnesium potassium phosphate ceramic for 99Tc immobilization," *Journal of Nuclear Materials*, vol. 348, no. 3, pp. 272–282, 2006.

[22] A. S. Wagh, R. Strain, S. Y. Jeong, D. Reed, T. Krause, and D. Singh, "Stabilization of Rocky Flats Pu-contaminated ash within chemically bonded phosphate ceramics," *Journal of Nuclear Materials*, vol. 265, no. 3, pp. 295–307, 1999.

[23] A. S. Wagh, S. Y. Sayenko, A. N. Dovbnya et al., "Durability and shielding performance of borated Ceramicrete coatings in beta and gamma radiation fields," *Journal of Nuclear Materials*, vol. 462, pp. 165–172, 2015.

[24] B. C. Sales and L. A. Boatner, "Lead-iron phosphate glass: A stable storage medium for high-level nuclear waste," *Science*, vol. 226, no. 4670, pp. 45–48, 1984.

[25] G. N. Greaves, S. J. Gurman, L. F. Gladden et al., "A structural basis for the corrosion resistance of lead-iron-phosphate glasses: An X-ray absorption spectroscopy study," *Philosophical Magazine*, vol. 58, no. 3, pp. 271–283, 2006.

[26] J. H. Cho, Y. Eom, and T. G. Lee, "Stabilization/solidification of mercury-contaminated waste ash using calcium sodium phosphate (CNP) and magnesium potassium phosphate (MKP) processes," *Journal of Hazardous Materials*, vol. 278, pp. 474–482, 2014.

[27] W. Huang, D. E. Day, C. S. Ray, C.-W. Kim, and A. Mogus-Milankovic, "Vitrification of high chrome oxide nuclear waste in iron phosphate glasses," *Journal of Nuclear Materials*, vol. 327, no. 1, pp. 46–57, 2004.

[28] J. Wang and X. Cao, "Formic denitration of the simulated highlevel liquid waste," *Nuclear Science and Engineering*, no. 01, pp. 93–98, 1997.

[29] D. M. Strachan, R. P. Turcotte, and B. O. Barnes, "MCC-1: A Standard Leach Test for Nuclear Waste Forms," *Nuclear Technology*, vol. 56, no. 2, pp. 306–312, 1980.

[30] W. E. Lee, M. I. Ojovan, and C. M. Jantzen, *Radioactive Waste Management and Contaminated Site Clean-Up*, W. E. Lee, M. I. Ojovan, and C. M. Jantzen, Eds., Woodhead Publishing Limited, 2013.